PHYSICAL REVIEW D **111,** 074511 (2025)

Meson spectroscopy in the $Sp(4)$ gauge theory with three antisymmetric fermions

Ed Bennett,[1,*] Deog Ki Hong,[2,3,†] Ho Hsiao,[4,5,‡] Jong-Wan Lee,[6,§] C.-J. David Lin,[5,7,‖] Biagio Lucini,[1,8,¶]
Maurizio Piai,[9,**] and Davide Vadacchino[10,††]

[1]*Swansea Academy of Advanced Computing, Swansea University (Bay Campus),*
Fabian Way, SA1 8EN Swansea, Wales, United Kingdom
[2]*Department of Physics, Pusan National University, Busan 46241, Korea*
[3]*Extreme Physics Institute, Pusan National University, Busan 46241, Korea*
[4]*Center for Computational Sciences, University of Tsukuba,*
1-1-1 Tennodai, Tsukuba, Ibaraki 305-8577, Japan
[5]*Institute of Physics, National Yang Ming Chiao Tung University,*
1001 Ta-Hsueh Road, Hsinchu 30010, Taiwan
[6]*Particle Theory and Cosmology Group, Center for Theoretical Physics of the Universe,*
Institute for Basic Science (IBS), Daejeon, 34126, Korea
[7]*Centre for High Energy Physics, Chung-Yuan Christian University, Chung-Li 32023, Taiwan*
[8]*Department of Mathematics, Faculty of Science and Engineering, Swansea University (Bay Campus),*
Fabian Way, SA1 8EN Swansea, Wales, United Kingdom
[9]*Department of Physics, Faculty of Science and Engineering, Swansea University,*
Singleton Park, SA2 8PP, Swansea, Wales, United Kingdom
[10]*Centre for Mathematical Sciences, University of Plymouth, Plymouth, PL4 8AA, United Kingdom*

(Received 19 December 2024; accepted 28 February 2025; published 14 April 2025)

We report the results of an extensive numerical study of the $Sp(4)$ lattice gauge theory coupled to fermion matter content consisting of three (Dirac) flavors, transforming in the two-index antisymmetric representation of the gauge group. In the presence of (degenerate) fermion masses, the theory has an enhanced global $SU(6)$ symmetry, broken explicitly and spontaneously to its $SO(6)$ subgroup. This symmetry breaking pattern makes the theory interesting for applications in the context of composite Higgs models, as well as for the implementation of top partial compositeness. Alternatively, it can also provide a dynamical realization of the strongly interacting massive particle paradigm for the origin of dark matter. We adopt the standard plaquette gauge action, along with the Wilson-Dirac formulation for the fermions, and apply the (rational) hybrid Monte Carlo algorithm in our ensemble generation process. We monitor the autocorrelation and topology of the ensembles. We explore the bare parameter space, and identify the weak and strong coupling regimes, which are separated by a line of first-order bulk phase transitions.

We measure two-point correlation functions between meson operators that transform as nontrivial representations of $SO(6)$, and extract the ground-state masses, in all accessible spin and parity channels. We assess the size of finite volume effects, and restrict attention to measurements in which these systematic effects are negligibly small compared to the statistical uncertainties. The accuracy of our data enables us to extract the decay constants of the composite particles in the pseudoscalar, vector and axial-vector channels. In addition, we measure the mass of the first excited state for one of the channels, the vector meson, by performing a generalized eigenvalue problem analysis involving two different meson operators. Spectral quantities show a mass dependence that is compatible with the expectation that, at long distances, the

---

[*] Contact author: E.J.Bennett@swansea.ac.uk
[†] Contact author: dkhong@pusan.ac.kr
[‡] Contact author: hohsiao@ccs.tsukuba.ac.jp
[§] Contact author: j.w.lee@ibs.re.kr
[‖] Contact author: dlin@nycu.edu.tw
[¶] Contact author: B.Lucini@Swansea.ac.uk
[**] Contact author: m.piai@swansea.ac.uk
[††] Contact author: davide.vadacchino@plymouth.ac.uk

theory undergoes confinement, accompanied by the spontaneous breaking of the approximate global symmetries acting on the matter fields. Finally, we discuss the continuum and massless extrapolations within the framework of Wilson chiral perturbation theory, after setting the physical scale using the gradient flow method, and compare the results to those of existing studies in the quenched approximation, as well as to the literature on closely related theories.

DOI: 10.1103/PhysRevD.111.074511

I. INTRODUCTION

New physics systems made of composite particles, arising from novel strong coupling dynamics, yield promising scenarios within which to address the big open questions in contemporary particle physics and astrophysics. They form the basis of composite Higgs models (CHMs) [1–3] (see also the reviews in Refs. [4–6], the tables in Refs. [7–9], a selection of publications in Refs. [10–51] and the holographic models in Refs. [52–65]), models of top partial compositeness (TPC) [66] (see also Refs. [67–69], for useful discussions), models of dark sectors [70–76], composite dark matter [6,77–86] (see also Ref. [87]), and strongly interacting massive particles (SIMPs) [88–97] (see also the review [98] and references therein). Their presence might even affect the thermal history of the early Universe, giving rise to inflation [99–101]. A stochastic relic density of gravitational waves might arise if such systems underwent a first-order phase transition during the times our universe was hot [102–107]. Such effects are detectable in present and future experiments [108–125] (see the discussions in Refs. [126–133] and [134–142]).

Motivated by compositeness scenarios, an extensive program of theoretical explorations on the lattice with orthogonal and symplectic groups (TELOS), in particular in the case of $Sp(2N)$ groups, has led to significant recent advancements in their understanding [143–156]—see also Refs. [157–164] as well as Refs. [165–172] and the pioneering work in Ref. [173]. Field theories with symplectic gauge group, $Sp(N_c = 2N)$, lead to enhanced global symmetry patterns, distinctive from those emerging in $SU(N_c)$ gauge theories. Nevertheless, in the large-N_c limit, $Sp(N_c)$ and $SU(N_c)$ gauge theories are expected to share the same physics in a common sector. Interesting ideas have been put forward to describe the associated nonperturbative phenomena [146,149,174–176], hence providing more general reasons to gain understanding of nonperturbative properties of $Sp(2N)$ theories. Finally, dedicated studies of these theories have also appeared within bottom-up holographic models [177–179]—an example of top-down holographic models is found in Ref. [180].

In the CHM context, the minimal model amenable to lattice studies exploits the global symmetry patterns described by the $SU(4)/Sp(4)$ coset. It can be realized by the $Sp(2N)$ gauge theory coupled to $N_{\rm f} = 2$ matter fermions transforming in the fundamental representation, (f) [181]. For $N > 1$, the addition of $N_{\rm as} = 3$ fermions transforming in the two-index antisymmetric representation, (as), leads to the minimal realization of a model combining CHM and TPC [182].[1] The enhanced $SU(6)$ global symmetry acting on the $N_{\rm as} = 3$ fermions is broken to $SO(6)$, both by the presence of degenerate fermion masses, and by the formation of a fermion condensate [181]. The $SU(3)$ group associated with quantum chromodynamics (QCD) is identified with a subgroup of the unbroken $SO(6)$, and fermion bound states involving one (as)-type and two (f)-type fermions have the right quantum numbers to act as partners of the top quark.

In this paper, we study a closely related $Sp(4)$ lattice theory, coupled to $N_{\rm as} = 3$ (as)-type dynamical Dirac fermions, but in which $N_{\rm f} = 0$. Because of the large multiplicity of the antisymmetric representation, this single-representation lattice theory is expected to approximate well the two species theory, without the significant complications due to the mixed matter field content. We refer to the handful of existing lattice studies in theories with mixed representations: see for instance Refs. [193–199] for the $SU(4)$ theory with fundamental and two-index antisymmetric fermions, Refs. [148,155,156] for the $Sp(4)$ theory with $N_{\rm as} = 3$ and $N_{\rm f} = 2$, and Refs. [200,201] for the $SU(2)$ gauge theories with fundamental and adjoint matter.

This lattice theory is of interest in itself, as the strongly coupled origin of effective field theories (EFTs) based on the $SU(6)/SO(6)$ coset. Such EFTs can be used to provide an alternative CHM, which includes a composite dark matter candidate [41]. The SIMP mechanism could also be realized in this theory, by generalizing the $SU(4)/SO(4)$ analysis in Ref. [86].

A further reason why this lattice theory is interesting *per se* pertains the mapping of the phase space of gauge theories at zero temperature. Given the large multiplicity of its fermion matter fields, it is important to check with an *ab initio* calculation how far the $Sp(4)$ theory with $N_{\rm as} = 3$ sits from the lower edge of the conformal window [202–210]—see also the higher-loop analyses in Refs. [211–221], which generalize the Banks-Zaks (BZ) fixed point [222,223] to higher-loop orders using the results in Refs. [224–227]. Nonperturbative hints of near conformal dynamics might manifest themselves in the slow running of the coupling (walking [228–230]), and

---

[1] The $SU(4)/Sp(4)$ coset appears also in $SU(2)$ lattice theories [183–192]. In this case, though, the antisymmetric representation is trivial, and TPC cannot be realized in the same way.

unconventional scaling of composite operators [203,231]. We are going to test these possibilities, and provide evidence that this theory confines and breaks its global, approximate, continuous symmetries, in a way not dissimilar from QCD, the theory of strong nuclear forces. The literature on lattice studies of candidate theories with unconventional, near conformal, strongly coupled dynamics—see, for instance, Refs. [232–282]—is reviewed in Ref. [283].

For this work, we adopt the standard (unimproved) Wilson gauge action and Wilson-Dirac fermions. Their dynamical implementation is achieved through the rational hybrid Monte-Carlo (RHMC) algorithm [284,285]. Preliminary results have been presented in Ref. [160]. We use the Wilson flow [286–288] to set the scale, and also as a smoothening procedure in computing the topology of the ensembles, with which we monitor their autocorrelations. To measure the meson mass spectra, we complement the use of stochastic wall sources [289] by the implementation of Wuppertal smearing of sources and sinks [290–292], supplemented by APE smearing of the link variables [293,294]. The spectrum of the vector meson sector is obtained from a generalized eigenvalue problem (GEVP)—see also Ref. [156]. We compute also (renormalized) meson decay constants [295,296], where this is possible with our available data. We perform an extensive study of finite-volume effects. We extrapolate our numerical results toward the massless and continuum limits, relying on Wilson chiral perturbation theory (WχPT) [297,298] by borrowing ideas from Ref. [299], and from the literature on improvement [300,301].

This is the first systematic, dedicated calculation, in this lattice gauge theory, to allow for an extrapolation toward the continuum limit. We benchmark our results against existing measurements, obtained either in the quenched approximation of the same theory, or in other related theories with dynamical fermions: the $Sp(4)$ theory coupled to $N_{\mathrm{f}} = 2$ fermions, and the $SU(3)$ theory with three quarks—we remind the reader that, in $SU(3)$, the two-index antisymmetric representation coincides with the conjugate of the fundamental one. Interesting trends emerge from these critical comparisons, which we highlight later in the paper.

The paper is organized as follows. We introduce the (continuum and lattice) theories of interest in Sec. II. We devote Sec. III to studying the properties of the lattice theory. We identify its bulk phase transitions in (lattice) parameter space. We perform a finite-volume study, to identify criteria that allow us to ensure that such systematic effects can be neglected, in comparison with existing statistical uncertainties. We introduce at this stage our treatment of the Wilson flow, and its complementary uses to set the scale and to compute the topology in our configurations. Section IV details our definitions of meson operators, correlation functions, masses, and decay constants, and the processes we follow in our measurements. The numerical results are summarized in Sec. V, which describes also our approach to the continuum and massless limits. We discuss our main results and outline future avenues for investigation in Sec. VI. Appendixes A–D contain tables of intermediate numerical results and technical details that may be helpful in reproducing our analysis—we provide access to our data and the analysis code in Refs. [302,303].

Appendix E presents a preliminary, alternative analysis of the spectral measurements we collected, performed in the light of dilaton effective field theory (dEFT) [304–319].[2] It provides an unconventional interpretation and analysis tool, with respect to the Wilson chiral perturbation theory adopted in the main body of the paper. This new instrument has given interesting results in dynamical theories with near conformal dynamics, such as the case of $SU(3)$ theories with $N_{\mathrm{f}} = 8$ fundamental fermions [339–347], or $N_{(s)} = 2$ fermions transforming in the two-index symmetric representation [348–353]. We hence decided to perform and report this exercise, although we anticipate that our results are inconclusive. Such an analysis promises to become important for future higher statistics calculations, performed at smaller fermion masses and closer to the continuum limit, particularly if flavor-singlet scalar mesons are accessible.

II. THE $Sp(4)$ THEORY OF INTEREST

The field content of the $Sp(4)$ gauge theory of interest consists of the gauge fields, $V_\mu \equiv \sum_A V_\mu^A T^A$ (where T^A, for $A = 1, \ldots, 10$, are the hermitian generators of the group, normalized so that $\mathrm{Tr}T^A T^B = \frac{1}{2}\delta^{AB}$), and three flavors of massive (degenerate) hyperquarks, Ψ. These Dirac fermions, that are described by antisymmetric 4×4 matrices in $Sp(4)$, obey the condition $\mathrm{Tr}[\Omega\Psi] = 0$, where the symplectic matrix, Ω, is

$$\Omega \equiv \begin{pmatrix} 0 & \mathbb{1}_{2\times 2} \\ -\mathbb{1}_{2\times 2} & 0 \end{pmatrix}. \qquad (1)$$

The fermions transform in the antisymmetric, two-index representation, as $\Psi \to U\Psi U^T$, under the action of a group element, $U \in Sp(4)$. The continuum Lagrangian density is

$$\mathcal{L} = -\frac{1}{2}\mathrm{Tr}V_{\mu\nu}V^{\mu\nu} + \overline{\Psi^j}(iD_\mu\gamma^\mu - m)\Psi^j, \qquad (2)$$

---

[2] The idea that a light scalar particle, the dilaton, associated with the spontaneous breaking of scale invariance, might appear in proximity of the lower edge of the conformal window is quite old [229,320,321], and so is the first effective field theory (EFT) description of its behavior [322,323]. The striking phenomenological implications for new physics of the emergence of a dilaton [324] are the subject of a vast literature—an incomplete selection of interesting work includes Refs. [69,325–335] and references therein. Examples of application of dEFT in the CHM context can be found in Refs. [317,318]—see also related earlier work in Refs. [336–338].

where $\mu,\ \nu = 1,\ 2,\ 3,\ 4$ are space-time indexes and $j = 1, 2, 3$ flavor indexes, while summations over repeated indices are understood. In our convention the Minkowski metric has signature $(+,-,-,-)$. The field strength tensor, $V_{\mu\nu}$, and the covariant derivative, D_μ, are defined by

$$V_{\mu\nu} \equiv \partial_\mu V_\nu - \partial_\nu V_\mu + ig[V_\mu, V_\nu], \tag{3}$$

$$D_\mu \Psi \equiv \partial_\mu \Psi + igV_\mu \Psi + ig\Psi V_\mu^T, \tag{4}$$

where g is the gauge coupling.

The fermion degrees of freedom populating the entries of the antisymmetric matrices, Ψ^{ab}, with $a, b = 1, \ldots, 4$, span an irreducible representations of $Sp(4)$, which, as the group is locally isomorphic to $SO(5)$, coincides with the vectorial representation, **5**, of $SO(5)$, after imposing the aforementioned Ω-traceless requirement on Ψ. Because such a representation is real, the global (flavor) symmetry acting on $N_{(\mathrm{as})} = 3$ Dirac fermions is enhanced from $U(3)_L \times U(3)_R$ to $U(1) \times SU(6)$. In this paper, we ignore the (anomalous) $U(1)$, focusing on nontrivial representations of the non-Abelian, $SU(6)$, factor. This symmetry is broken to the maximal $SO(6)$ subgroup by the nonzero, degenerate fermion mass, m. In the massless case, the $SU(6)$ global symmetry is also spontaneously broken along the same pattern, if a nonvanishing condensate, $\langle \bar{\Psi}\Psi \rangle \neq 0$, emerges.

A. Lattice action

The lattice theory is written by applying a Wick rotation to the four-dimensional space-time, and discretizing the Euclidean space on hypercubic lattice of size $N_t \times N_s^3 = (T/a) \times (L/a)^3$, with a the lattice spacing, T and L the temporal and spatial extents, respectively. As the discretized version of the action based on the Lagrangian density in Eq. (2), we adopt the standard plaquette action for the gauge fields, supplemented by the Wilson-Dirac fermion formulation for hyperquarks, Ψ, and write

$$S \equiv \beta \sum_{n,\mu<\nu} \left(1 - \frac{1}{4}\mathrm{ReTr}\mathcal{P}_{\mu\nu}(n)\right) + a^4 \sum_n \bar{\Psi}_j(n) D^{(as)} \Psi_j(n), \tag{5}$$

where $\mu, \nu = 1, 2, 3, 4$ are space-time indexes, $j = 1, 2, 3$ the flavor indexes, and n denotes the lattice sites. The lattice bare coupling, β, is related with the gauge coupling, g, by $\beta = 8/g^2$. The elementary plaquette, $\mathcal{P}_{\mu\nu}$, is defined as

$$\mathcal{P}_{\mu\nu}(n) \equiv U_\mu(n) U_\nu(n+\hat{\mu}) U_\mu^\dagger(n+\hat{\nu}) U_\nu^\dagger(n), \tag{6}$$

where $U_\mu \in Sp(4)$ denotes the gauge link, which satisfies the condition $U^* = \Omega U \Omega^\dagger$. We impose periodic boundary conditions on all the fields, except for the temporal directions for the fermion fields, Ψ, which obey antiperiodic boundary conditions.

We exploit the aforementioned properties of the irreducible representation of the fermions, **5**, to write the Wilson-Dirac operator in terms of the link variable for the antisymmetric representation, $U_\mu^{(\mathrm{as})}$, and the bare hyperquark mass, m_0, as

$$\begin{aligned} D^{(as)}\Psi_j(x) \equiv{}& (4/a + m_0)\Psi_j(x) \\ &- \frac{1}{2a}\sum_\mu \Big\{ (1-\gamma_\mu) U_\mu^{(\mathrm{as})}(x)\Psi_j(x+\hat{\mu}) \\ &+ (1+\gamma_\mu) U_\mu^{(\mathrm{as})\dagger}(x-\hat{\mu})\Psi_j(x-\hat{\mu}) \Big\}. \end{aligned} \tag{7}$$

The relation to the fundamental link, U_μ, reads

$$U_{\mu,AB}^{(as)}(x) \equiv \mathrm{Tr}\left[e_A^{(as)\dagger} U_\mu(x) e_B^{(as)} U_\mu^{\mathrm{T}}(x) \right], \tag{8}$$

where the multi-indexes, $A = (ab)$ and $B = (cd)$, denote the ordered pairs with $1 \leq a(c) < b(d) \leq 4$. The basis matrices, $e_A^{(as)}$, are antisymmetric, and obey the defining relations $\mathrm{Tr}[\Omega e_A^{(as)}] = 0$ (they are Ω-traceless) and

$$\left(e_{A=(ab)}^{(as)}\right)_{cd} = \frac{1}{\sqrt{2}}\left(\delta_{ad}\delta_{bc} - \delta_{ac}\delta_{bd}\right), \tag{9}$$

except for $A = (24)$, which is given by

$$e_{A=(24)}^{(as)} = \begin{pmatrix} 0 & 0 & \frac{1}{2} & 0 \\ 0 & 0 & 0 & -\frac{1}{2} \\ -\frac{1}{2} & 0 & 0 & 0 \\ 0 & \frac{1}{2} & 0 & 0 \end{pmatrix}. \tag{10}$$

These five basis matrices satisfy also the orthonormalization condition $\mathrm{Tr}[e_A^{(as)T} e_B^{(as)}] = \delta_{AB}$.

B. Simulation details

Throughout this work, we employ standard bootstrap methods in our statistical analyses. We perform numerical calculations using a branch of the HiRep code [233], in which some of us implemented the $Sp(2N)$ gauge groups [143]. Dynamical gauge ensembles are generated with an admixture of both the Hybrid Monte Carlo (HMC) and Rational HMC (RHMC) [285,354] algorithms[3]; we introduce two pseudofermions, one in the HMC (for two flavor species) and the other (for the third species) in the RHMC evolutions, and dial their masses to reproduce the presence of three mass-degenerate Wilson-Dirac fermions—we verified elsewhere that this choice yields

---

[3] Using HiRep commit IDs `d3ab8d8` [355] and `9e66e56` [356].

compatible result with using the RHMC algorithm for all three species [148,152]. The determinant of the Dirac operator is real and positive for fermions in the antisymmetric representation (even with an odd number of them), thus numerical simulations are free from sign problems. The molecular dynamics (MD) evolution is implemented using a second-order Omelyan integrator [357].

The main properties of all our ensembles are summarized in Table I. Each ensemble consists of N_{cfg} thermalized configurations. The lattice coupling, β, and the bare hyperquark mass, am_0, as well as the lattice volume, $N_t \times N_s^3$, are chosen in such a way that our numerical results do not suffer from two typical artefacts due to the implementation of dynamical fermions in lattice calculations: the presence of first-order bulk transition and finite volume effects. We will discuss them in details in the next section.

For each ensemble we present the expectation value, $\langle \mathcal{P} \rangle$, of the average plaquette, $\mathcal{P}$, defined as

$$\mathcal{P} \equiv \frac{1}{6 N_t N_s^3} \sum_n \sum_{\mu<\nu} \left[\frac{1}{4} \mathrm{Re}\mathrm{Tr} \mathcal{P}_{\mu\nu}(n) \right]. \qquad (11)$$

TABLE I. Ensembles of dynamical $Sp(4)$ lattice gauge theories coupled to $N_{\mathrm{as}} = 3$ Wilson-Dirac hyperquarks transforming in the two-index antisymmetric representation of the gauge group. For each ensemble analyzed, we report the lattice extent, $N_t \times N_s^3$, the bare coupling, β, the fermion mass, am_0, the number of configurations, N_{cfg}, and the expectation value of average plaquette, $\langle P \rangle$. We also include a comment in the last column, discussed in the body of the paper.

Ensemble	$N_t \times N_s^3$	β	am_0	N_{cfg}	$\langle \mathcal{P} \rangle$	Comment
ASB0M1	48×18^3	6.6	−1.075	100	0.580347(15)	Heavy
ASB0M2	48×24^3	6.6	−1.08	140	0.582733(10)	Heavy
ASB0M3	48×32^3	6.6	−1.085	130	0.5849929(62)	
ASB1M1	48×18^3	6.65	−1.05	128	0.579896(12)	Heavy
ASB1M2	48×18^3	6.65	−1.06	120	0.583984(12)	Heavy
ASB1M3	48×18^3	6.65	−1.063	135	0.585150(14)	Heavy
ASB1M4	48×24^3	6.65	−1.07	137	0.5877893(86)	
ASB1M5	48×28^3	6.65	−1.075	215	0.5896176(54)	
ASB1M6	48×32^3	6.65	−1.08	180	0.5914586(56)	
ASB2M1	48×16^3	6.7	−1.02	200	0.578740(28)	Heavy
ASB2M2	48×16^3	6.7	−1.03	110	0.582264(35)	Heavy
ASB2M3	48×18^3	6.7	−1.04	100	0.585678(14)	Heavy
ASB2M4	48×24^3	6.7	−1.045	120	0.5873337(84)	Heavy
ASB2M5	48×24^3	6.7	−1.05	110	0.5889499(90)	Heavy
ASB2M6	48×24^3	6.7	−1.055	180	0.5905740(86)	
ASB2M7	54×28^3	6.7	−1.06	201	0.5921942(59)	
ASB2M8	54×28^3	6.7	−1.063	150	0.5931513(75)	
ASB2M9	54×32^3	6.7	−1.065	150	0.5937583(54)	
ASB2M10	54×36^3	6.7	−1.067	195	0.5944477(41)	
ASB2M11	54×36^3	6.7	−1.069	218	0.5950649(38)	
ASB3M1	54×18^3	6.75	−1.03	180	0.590439(12)	Heavy
ASB3M2	54×24^3	6.75	−1.041	120	0.5935363(84)	
ASB3M3	54×24^3	6.75	−1.046	180	0.5949951(72)	
ASB3M4	54×28^3	6.75	−1.051	196	0.5963914(66)	
ASB3M5	54×32^3	6.75	−1.055	225	0.5975680(48)	
ASB4M1	56×16^3	6.8	−1.01	171	0.592230(14)	Heavy
ASB4M2	54×16^3	6.8	−1.02	165	0.594777(13)	Heavy
ASB4M3	54×24^3	6.8	−1.03	180	0.5972763(73)	
ASB4M4	56×24^3	6.8	−1.035	275	0.5985597(78)	
ASB4M5	54×32^3	6.8	−1.04	170	0.5998238(50)	
ASB4M6	54×32^3	6.8	−1.043	251	0.6006178(38)	
ASB4M7	54×36^3	6.8	−1.046	219	0.6014000(34)	
ASB5M1	54×24^3	6.9	−1.01	391	0.6045303(54)	
ASB5M2	54×32^3	6.9	−1.017	216	0.6060103(43)	

We also investigate the history of the average plaquette along the trajectories to ensure that the system is thermalized. We discard a few hundreds of initial trajectories, the precise number of which, for each ensemble, is chosen by monitoring the value of $\mathcal{P}$. We compute the autocorrelation length of the average plaquette, $\tau^{\mathcal{P}}_{\rm exp}$, over the thermalized configurations, and separate them by $\delta_{\rm traj}$ trajectories, with $\delta_{\rm traj} \gtrsim \tau^{\mathcal{P}}_{\rm exp}$. The definition and the resulting values of $\tau^{\mathcal{P}}_{\rm exp}$, as well as our choices of $\delta_{\rm traj}$, can be found in Appendix B.

In the last column of Table I, we also anticipate some qualitative assessment of the properties of the ensembles, that will be discussed in more details later in the body of the paper. We denote as "heavy" those ensembles in which the bare mass is so large that an unexpected behavior (to be discussed in Sec. V) shows up in the measured spectral quantities; we exclude such ensembles from the continuum extrapolation.

III. CHARACTERIZATION OF THE LATTICE THEORY

We devote this section to the characterization of the lattice theory of interest. This part of the numerical investigation determines the range of lattice theory bare parameters and volumes used in the generation of gauge ensembles and physics measurements. We reveal the existence of a first-order bulk phase transition separating the range of lattice parameters that is connected to the continuum theory from the lattice strong coupling regime. We assess the size of finite-volume effects on spectroscopic observables. We introduce the Wilson flow as a scale setting procedure, and as a tool to compute the topological properties of the configurations.

A. Phase space

The lattice spacing, a, serves as an ultraviolet (UV) regulator. The continuum theory of interest is recovered in the limit $a \to 0$, corresponding to the quantum critical point of the lattice theory. In the space of lattice parameters, the continuum theory can be approached by extrapolating physical measurements toward the limit $\beta \to \infty$. In the presence of fermions, there is also a second free parameter, the bare mass, am_0, which must be dialed toward the limit of interest. In the Wilson-Dirac formulation of the fermions, this parameter is affected by additive renormalization, which further complicates extrapolations toward physically interesting regions of parameter space. Yet, the main concern is the existence of potential bulk phase transitions, restricting the basin of attraction of the Gaussian fixed point in lattice parameter space.

Preliminary studies have shown the existence of a first-order bulk phase transition in the strong coupling regime [152,157], highlighted by evidence of hysteresis in the average plaquette, $\langle \mathcal{P} \rangle$. Phase transition points appear to lie along a line in the plane of lattice parameters, (am_0, β), with the line ending at a critical point. For this publication, we conducted an additional study, which refines earlier findings by narrowing down the range of β values to $\beta = 6.4, 6.45, 6.5$, near the critical point, and increasing the statistics. The results are shown in Fig. 1. The transition is first order for $\beta = 6.4$, but becomes a smooth crossover at $\beta \simeq 6.45$. We therefore restrict our computations to the weak coupling regime, defined by the constraint $\beta > 6.45$.

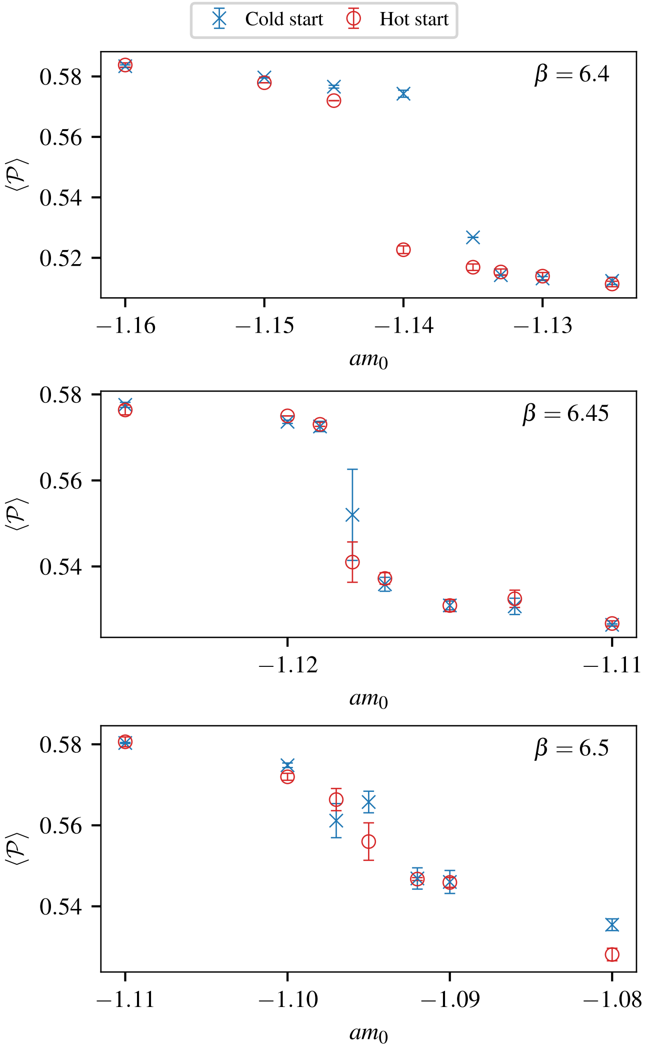

FIG. 1. Numerical measurement of the ensemble average of the plaquette, $\langle \mathcal{P} \rangle$, as a function of the (degenerate) bare mass, am_0, of the fermions transforming as the antisymmetric representation of the $Sp(4)$ gauge group, for three representative values of the lattice coupling, $\beta = 6.4$, 6.45, 6.5 (top to bottom panels, respectively). Results are presented for isotropic lattices with extent $N_t N_s^3 = 8^4$. Average plaquette values are measured using thermalized configurations with both cold (unit) and hot (random) starts; we denote the former by blue crosses and the latter by red empty circles.

B. Finite volume effects

The finiteness of the volume introduces a spurious discretization of all physical spectra measured on the lattice. The volume itself appears as an unphysical scale, acting as an infrared (IR) regulator, and affects all spectral quantities. For the purpose of assessing (and minimizing) the size of these finite volume (FV) effects, in this brief subsection we anticipate some preliminary results of our analysis of spectral quantities. We identify general criteria that we later apply to select the ensembles we retain in the physical analysis in the body of the paper. Having done so, FV effects will be ignored in subsequent sections.

In confining theories, spectral observables are expected to receive exponentially suppressed corrections due to FV effects, as long as the spatial length, $L = aN_s$, is larger than the longest intrinsic length scale in the physical system, the Compton wavelength of the lightest composite state. As can be confirmed *a posteriori*, the pseudoscalar (ps) meson is the lightest among the composite states considered in this work. We hence focus attention on the mass of the ground state in the ps channel, and study its dependence on the spatial volume—we return to describing this measurement in the next section.

In Table II, we present an example of the numerical results we collected for the purpose of FV effects study. We fix the lattice parameters, $\beta = 6.8$ and $am_0 = -1.03$, the length of the time direction in the lattice, $N_t = 54$. We also provide some details about the characterization of the ensembles. We consider six different volumes, with $N_s = L/a = 8$, 12, 16, 18, 20, 24, and for each measure the mass of the lightest ps state, $am_{\rm ps}$. For completeness, in the table we report the (bare) partially-conserved axial current (PCAC) mass, $am_{\rm PCAC}$, which can be used as a more physical assessment of the fermion mass, being free of additive renormalization. Finally, we show the value of the mass of the lightest vector meson, $am_{\rm v}$.

In the upper panel of Fig. 2, we show the measured mass of the ps mesons, $am_{\rm ps}$, as a function of $m_{\rm ps}^{\rm inf}L$. We estimate

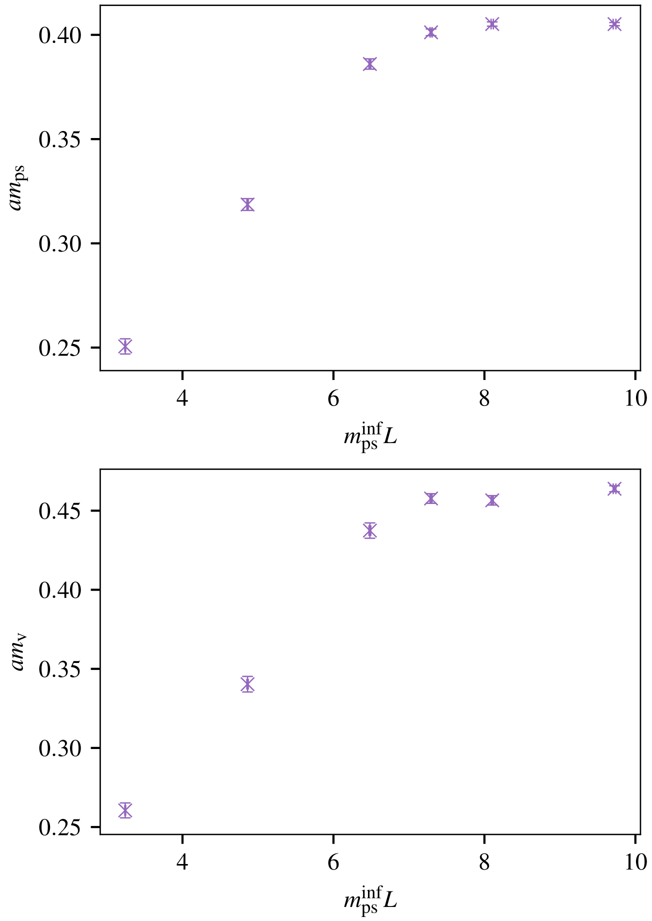

FIG. 2. Pseudoscalar meson mass, $am_{\rm ps}$ (top panel), and vector meson mass, $am_{\rm v}$ (bottom panel), as a function of the infinite-volume pseudoscalar mass, $am_{\rm ps}^{\rm inf}$, multiplied by the spatial extent $N_s = L/a$. The lattice coupling and the bare hyperquark mass used for the calculations are $\beta = 6.8$ and $m_0 = -1.03$, respectively. The pseudoscalar mass at infinite volume, $m_{\rm ps}^{\rm inf}$, is estimated by taking the one measured in the largest available lattice, with $N_t \times N_s^3 = 54 \times 24^3$.

TABLE II. Ensembles generated for the study of finite volume effects. The lattice coupling and the bare mass are fixed to $\beta = 6.8$ and $am_0 = -1.03$, respectively, while $N_{\rm cfg}$ is the number of configurations, separated by $\delta_{\rm traj} = 12$ trajectories between adjacent configurations, and $\langle \mathcal{P} \rangle$ is the average plaquette. The measured PCAC hyperquark and meson masses are expressed in lattice units, while $m_{\rm ps}^{\rm inf}$ denotes the pseudoscalar mass at infinite volume which is estimated as the mass measured at the largest available lattice.

$N_t \times N_s^3$	$N_{\rm cfg}$	$\langle \mathcal{P} \rangle$	$am_{\rm PCAC}$	$am_{\rm ps}$	$am_{\rm v}$	$m_{\rm ps}^{\rm inf}L$
54×8	200	0.596973(37)	0.05742(64)	0.2506(36)	0.2605(47)	3.2413(60)
54×12	300	0.597306(14)	0.05837(24)	0.3186(28)	0.3403(49)	4.8619(91)
54×16	209	0.597278(13)	0.05926(18)	0.3860(25)	0.4374(48)	6.483(12)
54×18	200	0.5972729(99)	0.05975(14)	0.4012(16)	0.4577(30)	7.293(14)
54×20	200	0.5972551(91)	0.05987(12)	0.4052(10)	0.4565(30)	8.103(15)
54×24	180	0.5972763(73)	0.059877(85)	0.40516(75)	0.4639(19)	9.724(18)

$m_{\rm ps}^{\rm inf}$ by assuming it coincides with the mass measured at the largest available lattice, $N_t \times N_s^3 = 54 \times 24^3$.[4] As expected, the ps mass quickly converges to its infinite-volume asymptotic value as the volume increases. The results for the two largest-volume lattices are indistinguishable, given present statistical uncertainties, indicating that FV effects can be ignored, when $m_{\rm ps}^{\rm inf} L \gtrsim 7.5$. We show also $am_{\rm v}$ as a function of $m_{\rm ps}^{\rm inf} L$, in the lower panel of Fig. 2. In the case of the three largest lattice volumes, the size of FV effects affecting $am_{\rm v}$ is comparable to the statistical uncertainty, which confirms that FV effects are negligible for $m_{\rm ps}^{\rm inf} L \gtrsim 7.5$.

This requirement is somewhat stronger than the analogous bound on the lattice volume applied to typical calculations in QCD, but significantly weaker than in theories known to be in the conformal window such as $SU(2)$ with two adjoint fermions [358]. Assuming that our theory is deep inside the confined and chirally broken phase, like is the case in QCD, this effect might be due to the fact that our dynamical ensembles probe a region of parameter space with relatively large mass, as will be discussed in Sec. V, where FV effects are enlarged by a factor of $m_{\rm ps}^2$. The observed, negative contribution of FV effects to $am_{\rm ps}$ is consistent with next-to-leading-order chiral perturbation theory (NLO χPT) expectations, as the sign of the coefficient of the contribution due to FV corrections, at the one-loop level, solely depends on the chiral symmetry breaking pattern [359]. We refer the reader to Refs. [148,151,159] for further details and discussion of FV effects in the $Sp(4)$ theory with dynamical fermions in different representations.

C. Wilson flow and scale setting procedure

We adopt the gradient flow and its lattice implementation, the Wilson flow [286–288], to set the scale in our lattice results and extrapolate them toward the continuum limit. This scale-setting procedure relies only on theoretical input, and amounts to the study of a diffusion process, in five dimensions, along a fictitious time, t. Gradient flow and Wilson flow can also be used to study the nonperturbative evolution of renormalized couplings [360,361]. Furthermore, they provide a smoothening procedure, suppressing short-distance fluctuations and optimizing the computation of long-distance properties, such as the topological charge, Q. We follow the ideas exposed in Ref. [362] to further reduce discretization effects.

The diffusion equation defining the gradient flow is

$$\frac{d}{dt} V_\mu(x,t) = -V_\mu(x,t) \frac{\partial S(V_\mu)}{\partial V_\mu(x,t)}, \tag{12}$$

and the flow variable, V_μ, at $t=0$ obeys the initial condition $V_\mu(x,0) = U_\mu(x)$. The flow equation can be solved via numerical integration, with infinitesimal flow time, δt. For the gauge action in Eq. (12), S, one can use the Wilson plaquette action, the first term of Eq. (5), which defines the *Wilson flow.* (One can replace, in S, the plaquette $\mathcal{P}_{\mu\nu}$, with a different object, so that the results differ only by terms that vanish in the continuum, $a \to 0$, limit.) As the fictitious time, t, flows, the gauge fields diffuse and high momentum fluctuations (discretization effects) are suppressed, while long-distance physics is preserved.

The gradient (Wilson) flow acts as Gaussian smoothening operator on the fields (configurations), removing short-distance singularities. The diffusion radius associated with this smoothening process has a characteristic length scale $\sim 1/\sqrt{8t}$ [286]. For $t > 0$, furthermore, it has been shown that correlation functions are finite to all orders in perturbation theory, in the sense described in Ref. [287]. Hence, one can fix a physical scale by assigning a reference value to one, conveniently chosen, physical observable. Following the proposal in Ref. [286], one can consider the energy density

$$E(t) \equiv \frac{1}{2} {\rm Tr} G_{\mu\nu}(t) G_{\mu\nu}(t), \tag{13}$$

where $G_{\mu\nu}$ is the field strength tensor associated with V_μ. As the expectation value of $E(t)$ has dimension of a mass to the fourth power, while t scales as the inverse of a mass squared, one defines the following dimensionless quantities, defined for any $t > 0$ [286,362]:

$$\mathcal{E}(t) \equiv t^2 \langle E(t) \rangle, \tag{14}$$

and its (logarithmic) derivative,

$$\mathcal{W}(t) \equiv t \frac{\rm d}{{\rm d}t} \mathcal{E}(t). \tag{15}$$

One then defines two alternative scales, t_0 and w_0, by imposing the following conditions, respectively:

$$\mathcal{E}(t)|_{t=t_0} = \mathcal{E}_0, \quad \text{or} \quad \mathcal{W}(t)|_{t=w_0^2} = \mathcal{W}_0. \tag{16}$$

The references values, $\mathcal{E}_0$ or $\mathcal{W}_0$, are chosen empirically, by aiming at minimizing systematic effects, such as lattice spacing and finite volume artefacts. To assess the size of discretization effects, we adopt two distinct, alternative definitions for the field-strength tensor, $G_{\mu\nu}$, obtained with either the plaquette in Eq. (6), $\mathcal{P}_{\mu\nu}$, or the clover-leaf, $\mathcal{C}_{\mu\nu}$ [297,363],

---

[4] We remark that the commonly used exponential fit in the mass of the pseudoscalar to determine the latter in the infinite volume limit does not appear to work in the regime of our calculation.

$$\begin{aligned}\mathcal{C}_{\mu\nu}(x) \equiv \frac{1}{8}\{&U_\mu(x)U_\nu(x+\hat{\mu})U^\dagger_\mu(x+\hat{\nu})U^\dagger_\nu(x)\\&+U_\nu(x)U^\dagger_\mu(x+\hat{\nu}-\hat{\mu})U^\dagger_\nu(x-\hat{\mu})U_\mu(x-\hat{\mu})\\&+U^\dagger_\mu(x-\hat{\mu})U^\dagger_\nu(x-\hat{\nu}-\hat{\mu})U_\mu(x-\hat{\nu}-\hat{\mu})\\&\times U_\nu(x-\hat{\nu})+U^\dagger_\nu(x-\hat{\nu})U_\mu(x-\hat{\nu})\\&\times U_\nu(x-\hat{\nu}+\hat{\mu})U^\dagger_\mu(x)-\text{H.c.}\},\end{aligned} \tag{17}$$

built out of the discretized lattice link variables by replacing $U_\mu(x)$ with $V_\mu(x,t)$, at $t>0$. With our ensembles, we could demonstrate the fact that, for $\mathcal{E}(t)$, the plaquette and clover definitions are not in complete agreement, yet show little discernible difference if we choose $\mathcal{E}_0 \gtrsim 0.25$. As illustrated in the example in Fig. 3, though, we find that the two definitions yield statistically consistent results, if one instead uses $\mathcal{W}(t)$, and $\mathcal{W}_0 \gtrsim 0.1$.

In view of these considerations, in our numerical study we use w_0 as the gradient flow scale, measured with the choice $\mathcal{W}_0 = 0.28125$, applied to the clover-leaf definition of the energy density. This numerical choice for $\mathcal{W}_0$ is derived by first adopting $\mathcal{W}_0 = 0.3$ for the $SU(3)$ Yang-Mills theory, and then applying plausible assumptions to the large-N_c scaling of the relevant observables, to compare to $Sp(4)$ [147].[5] For this choice of $\mathcal{W}_0$, we find that finite volume effects are at most $\mathcal{O}(5\%)$, as $\sqrt{8t_0}/L \lesssim 0.35$, according to the estimates in Ref. [360], except for a few heavy ensembles and for $\beta = 6.9$.

Another potential source of sizable systematic errors, particularly in ensembles with large β and small am_0, is the presence of autocorrelation in the measurements of the Wilson flow, which can be quantified by the autocorrelation time $\tau^{w_0}_{\rm exp}$ of the action density, $\mathcal{E}(t)$, evaluated at $t = w_0^2$. We refer the reader to Appendix B for the details of the determination of $\tau^{w_0}_{\rm exp}$ and to Table XI for the result. We find that $\tau^{w_0}_{\rm exp}$ is substantially larger than $\delta_{\rm traj}$ in any given ensemble. We therefore enlarge the separation between adjacent configurations to $\delta^{\rm GF}_{\rm traj} \gtrsim \tau^{w_0}_{\rm exp}$ in the measurements of the gradient flow scale. We report in Table III the measured values of w_0/a, obtained from $N^{\rm GF}_{\rm traj}$ configurations, separated by $\delta^{\rm GF}_{\rm traj}$ trajectories. In some cases, we are left with only a handful of independent configurations, hence we alert the reader to use caution in assessing the size of the statistical errors. Similar considerations will reappear later in the paper, when discussing the topological charge.

We rewrite all dimensionful quantities in terms of the Wilson flow scale, w_0. We denote the resulting quantities as $\hat{m} = mw_0$ and $\hat{f} = fw_0$, for masses and decay constants, respectively. As shown in Fig. 4, we find that the values of w_0/a grow as β grows, over the range $\beta \in [6.6, 6.9]$ available for this work. We also find evidence of a significant mass dependence in w_0/a, which is different to lattice QCD [362], but has been observed in lattice calculations for other gauge theories with dynamical fermions [145,193,276]. Following Refs. [145,193], throughout this work we adopt a mass-dependent scale-setting scheme, and rescale all dimensional quantities using the value of w_0/a as measured in the individual ensembles. The implications for our spectral measurementss are discussed in Sec. VA and Appendix C.

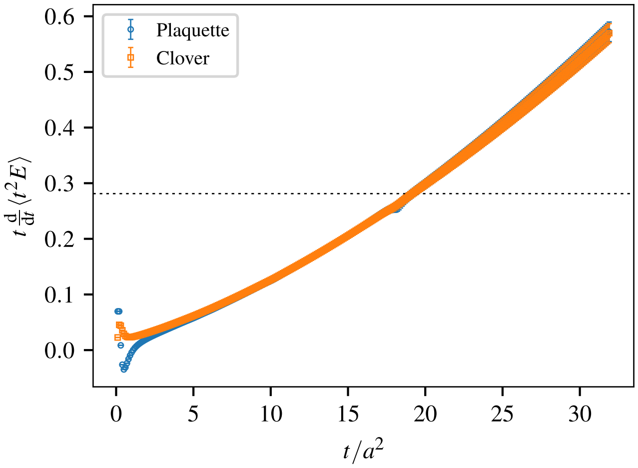

FIG. 3. The derivative of the expectation value of the energy density, $\mathcal{W}(t) \equiv td\langle t^2E\rangle/dt$, defined in Eq. (15), and built from the field strength tensor, $G_{\mu\nu}$, obtained either with the plaquette (blue circle) or the alternative, clover-leaf (orange square) definitions, as a function of flow time, t, in the ensemble ASB4M5. The black dashed line denotes our choice of reference value, $\mathcal{W}_0 = 0.28125$. Qualitatively equivalent plots can be obtained with other available ensembles.

D. Topology

The approach to the continuum limit of lattice calculations is affected by the critical slowing down of the local update algorithms, such as the HMC and RHMC used in this work. The topological charge, Q, is particularly sensitive to this problem. Its autocorrelation time rapidly grows as the lattice spacing decreases, and eventually becomes one of the longest ones in the system, as shown in Ref. [364] for $SU(N_c)$ and Ref. [150] for $Sp(N_c = 2N)$ gauge theories. If one keeps reducing the lattice spacing naively, asymptotically the algorithm gets trapped into one topological sector, rather than sampling the space, and violates ergodicity conditions.

This phenomenon of *topological freezing* may introduce sizable systematic effects in physical observables. For instance, 2-point correlation functions of flavor-singlet

---

[5] The renormalized coupling at the scale $\mu = 1/\sqrt{8t}$ is given by $\alpha(\mu) = k_\alpha \mathcal{E}(t)$ at the leading order in the perturbative expansion, with $k_\alpha^{-1} = 3N_c C_2(G)/16\pi$, and $C_2(G)$ the quadratic Casimir operator of the gauge group, G. Combined with the numerical value of $k_\alpha = 16\pi/15$ for the $Sp(4)$ theory, our choice of $\mathcal{W}_0 = 0.28125$ yields that $\alpha(\mu) \simeq 0.94$, suggesting that we are indeed testing the theory at the scale of hadronic physics.

TABLE III. Measurement of the gradient flow scale, w_0/a, and the measurement of the topological charge, Q, with Gaussian fit of the resulting distributions, in the ensembles used in this work. For each ensemble, the central value, Q_0, and standard deviation, σ_Q, are tabulated. Regarding the measurement of w_0/a, the number of uncorrelated configurations, $N_{\mathrm{traj}}^{\mathrm{GF}}$, is also presented. In the case of ASB5M1, the gradient flow scale is not available, because for some of the configurations we cannot reach the reference scale $\mathcal{W}_0$ in the measurement of $\mathcal{W}(t)$.

Ensemble	$N_{\mathrm{traj}}^{\mathrm{GF}}$	w_0/a	Q_0	σ_Q
ASB0M1	32	1.855(12)	−0.37(48)	3.61(42)
ASB0M2	46	2.1435(70)	1.84(46)	4.14(38)
ASB0M3	18	2.575(12)	−3.37(46)	4.04(39)
ASB1M1	42	1.6260(80)	−1.31(60)	4.69(47)
ASB1M2	23	1.982(17)	−1.21(45)	3.71(34)
ASB1M3	26	2.148(19)	−0.67(34)	3.19(29)
ASB1M4	33	2.600(19)	0.10(26)	2.40(23)
ASB1M5	17	3.063(29)	0.13(16)	2.00(11)
ASB1M6	8	3.654(56)	0.03(11)	1.386(86)
ASB2M1	66	1.4303(39)	0.06(38)	4.51(32)
ASB2M2	36	1.6262(70)	0.20(38)	3.17(32)
ASB2M3	16	1.925(21)	0.28(39)	2.91(33)
ASB2M4	39	2.1132(86)	−1.31(39)	3.34(32)
ASB2M5	27	2.342(17)	0.61(48)	3.93(39)
ASB2M6	14	2.630(36)	0.37(25)	2.86(19)
ASB2M7	9	3.125(68)	1.75(32)	2.33(24)
ASB2M8	18	3.405(41)	0.42(23)	2.22(17)
ASB2M9	12	3.614(56)	−0.814(89)	1.001(70)
ASB2M10	21	4.183(41)	0.426(77)	0.963(65)
ASB2M11	10	4.330(56)	1.462(76)	0.714(59)
ASB3M1	25	2.206(16)	−0.79(20)	2.34(17)
ASB3M2	19	2.634(24)	0.61(31)	2.74(26)
ASB3M3	22	3.059(37)	1.82(11)	1.302(87)
ASB3M4	9	3.628(51)	0.21(23)	2.08(16)
ASB3M5	12	4.079(55)	−2.46(16)	1.49(11)
ASB4M1	33	2.101(14)	−0.429(86)	1.839(62)
ASB4M2	23	2.437(36)	−1.38(15)	1.60(12)
ASB4M3	19	2.958(28)	−1.08(11)	1.296(86)
ASB4M4	21	3.365(36)	0.814(80)	1.075(47)
ASB4M5	28	3.828(22)	−1.30(13)	1.310(81)
ASB4M6	35	4.378(38)	−0.025(54)	0.697(39)
ASB4M7	13	4.692(52)	3.506(55)	0.591(46)
ASB5M1	…	…	0.053(60)	0.781(33)
ASB5M2	35	4.304(27)	−0.239(43)	0.407(30)

pseudoscalar mesons are expected to receive corrections of $\mathcal{O}(Q^2/V^2)$, with V the lattice volume, at large Euclidean time [365]. Since our primary interest is in the spectrum of flavored mesons, the problem might be less severe. Nevertheless, we do monitor the topological charge of our Monte Carlo trajectories, to assess whether any physical measurements are performed with ensembles that are affected by topological freezing.

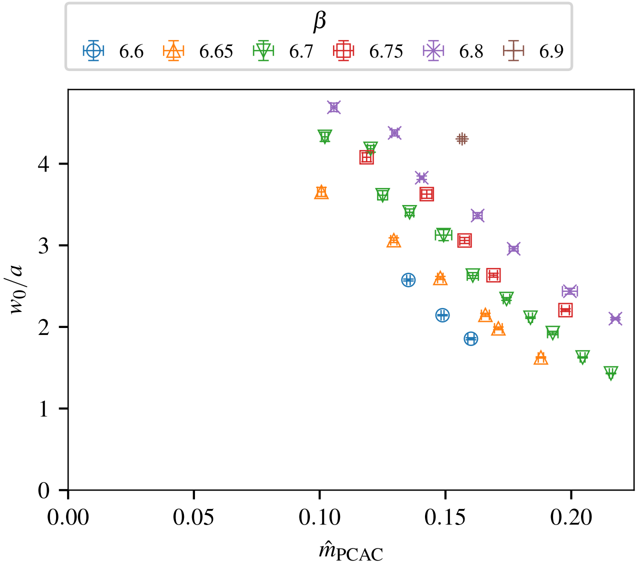

FIG. 4. The Wilson flow scale, w_0/a, measured in all the ensembles considered in this work, as a function of $\hat{m}_{\mathrm{PCAC}} \equiv m_{\mathrm{PCAC}} w_0$. The clover-leaf definition has been adopted in the energy density, while the reference value $\mathcal{W}_0 = 0.28125$ has been used in the scale-setting exercise. The value of β is indicated by the color and marker, as shown in the legend.

Because the gradient flow is a diffusion process which essentially smoothens out the quantum fields and thus suppresses UV fluctuations, we take advantage of it to study the topological charge on the lattice, $Q_L(t) \equiv \sum_x q_L(x,t)$, which is otherwise difficult to compute [286]. We define the lattice topological charge density, $q_L(x,t)$, in terms of the clover-leaf operator, $\mathcal{C}_{\mu\nu}(x,t)$, obtained from the flowed gauge fields, $V_\mu(x,t)$

$$q_L(x,t) \equiv \frac{1}{32\pi^2} \epsilon^{\mu\nu\rho\sigma} \mathrm{Tr} \mathcal{C}_{\mu\nu}(x,t) \mathcal{C}_{\rho\sigma}(x,t). \tag{18}$$

As the fields, V_μ, flow along the flow time, t, the values assumed by $Q_L(t)$ approach quasi-integer numbers, and their distribution displays a clear separation into different topological sectors. For large enough t, the measurement of $Q_L(t)$ becomes independent of t. In practice, we evaluate it at $t = t_Q \equiv L^2/32$. For notational convenience, we drop the subscript L from Q_L, for the rest of this section, being it understood that our topology measurements are always performed on the lattice.

In Fig. 5, we show examples of the history of the topological charge, Q, along the (R)HMC trajectory, for four representative ensembles. In the figure, going from left to right we reduce the fermion mass, while holding fixed β value, and from top to bottom we increase the value of β. We also perform a Gaussian fit of the histogram distribution of Q, and display the results of the maximum likelihood analysis, by using the fit function

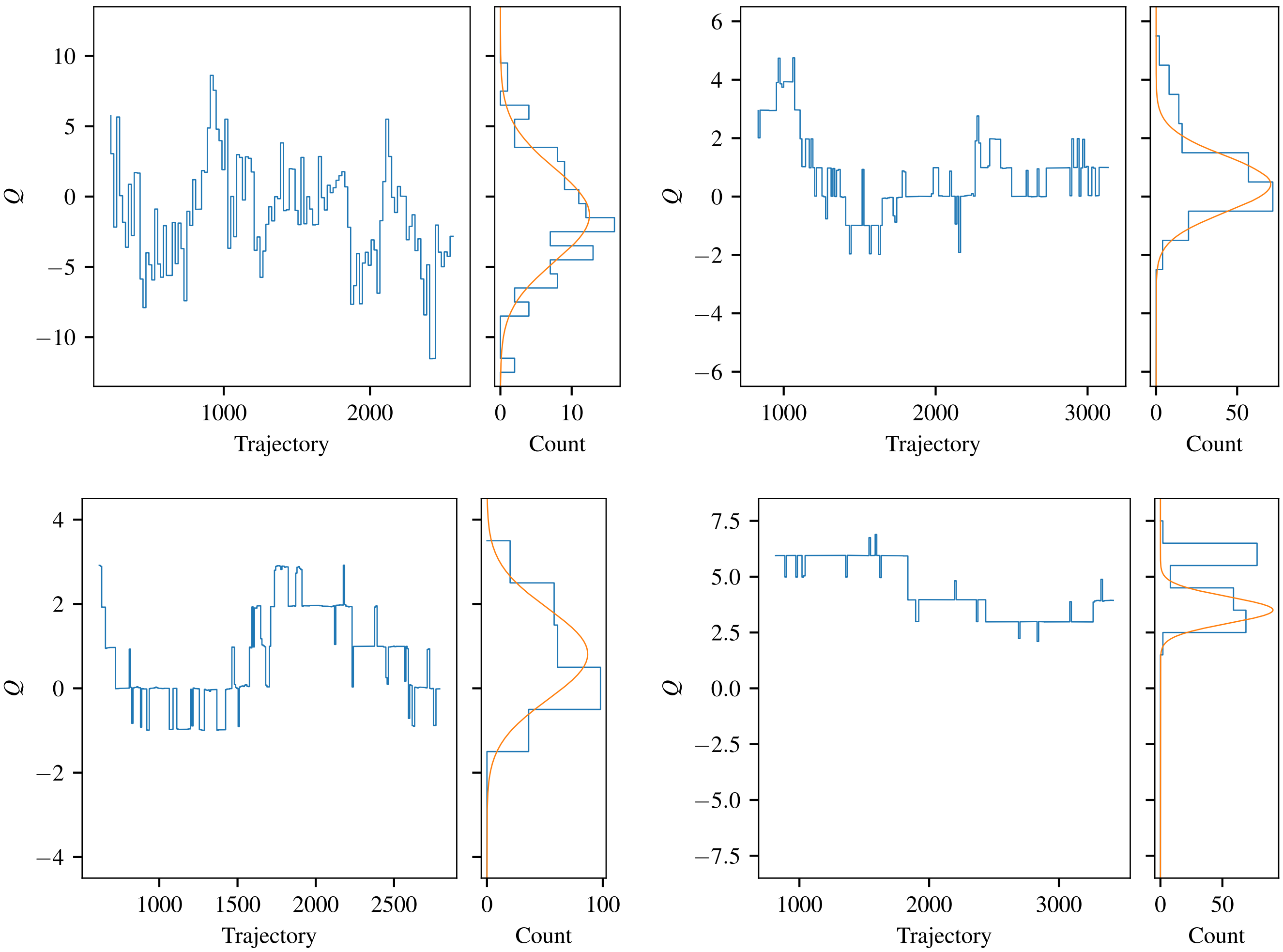

FIG. 5. Examples of the history of the topological charge, Q, along the (R)HMC trajectories. The lattice parameters, (β, am_0), used for the figures are $(6.7, -1.045)$ (top-left), $(6.7, -1.067)$ (top-right), $(6.8, -1.035)$ (bottom-left), and $(6.8, -1.046)$ (bottom-right). For each figure we also present an histogram of the distribution of Q, superimposed onto a Gaussian fit of the results.

$$n(Q) \equiv A_n \exp\left(-\frac{(Q - Q_0)^2}{2\sigma_Q^2}\right), \qquad (19)$$

in which Q_0 and σ_Q are the mean and the standard deviation, respectively. Our results for Q_0 and σ_Q are summarized in Table III. Except for a few light ensembles at larger β values, we find that the distribution of topological charge in the ensemble reproduces the expected Gaussian around zero.

The examples in Fig. 5 show long autocorrelation in the history of the topological charge along the trajectories. We estimate the autocorrelation time, $\tau^Q_{\rm exp}$, from exponential fit to the autocorrelation function for Q. In Appendix B, we present the results for $\tau^Q_{\rm exp}$ in Table XI. Because in each ensemble the fermion mass is different, one must use caution in making comparisons between different lattice couplings, yet the general trend is that the autocorrelation time, $\tau^Q_{\rm exp}$, increases while going toward finer lattices. Furthermore, $\tau^Q_{\rm exp}$ rapidly grows, for fixed β, as the fermion mass decreases. In the cases of light and fine ensembles, we find that the topological charge is almost frozen and the estimate of $\tau^Q_{\rm exp}$ is comparable in size to that of the available ensemble. The mass dependence of our results agrees with what we found in the calculation of the gradient flow scale, w_0/a, as well as its autocorrelation time, $\tau^{w_0}_{\rm exp}$: $\tau^Q_{\rm exp}$ and $\tau^{w_0}_{\rm exp}$ rapidly grow as the lattice becomes finer and/or the fermions are lighter.

IV. MESON SPECTROSCOPY

This section is devoted to defining the observables relevant to our study. We list the meson operators in the theory, the correlation functions we measure, and we describe the processes by which we extract the masses and decay constants of the composite states of interest.

A. Interpolating operators

In Table IV, we list the operators considered in this work. They are gauge invariant hyperquark bilinears, in the form

TABLE IV. Interpolating operators, $\mathcal{O}_M$, for mesons with spin $J = 0$, 1, and parity $P = \pm 1$, built of Dirac fermions in the antisymmetric representation, Ψ^{iab}, of $Sp(4)$. We show explicitly the flavor indices $i \neq j = 1, 2, 3$, while color and spinor indices are implicit and summed over. We also show the spin and parity quantum numbers, J^P, the corresponding QCD meson sourced by the analogous operator, and the irreducible representation of the unbroken global $SO(6)$ spanned by the meson, ignoring the $SO(6)$-singlets.

Label M	Interpolating operator $\mathcal{O}_M$	Meson in QCD	J^P	$SO(6)$
ps	$\overline{\Psi^i}\gamma_5\Psi^j$	π	0^-	$20'$
s	$\overline{\Psi^i}\Psi^j$	a_0	0^+	$20'$
v	$\overline{\Psi^i}\gamma_\mu\Psi^j$	ρ	1^-	15
t	$\overline{\Psi^i}\gamma_0\gamma_\mu\Psi^j$	ρ	1^-	15
av	$\overline{\Psi^i}\gamma_5\gamma_\mu\Psi^j$	a_1	1^+	$20'$
at	$\overline{\Psi^i}\gamma_5\gamma_0\gamma_\mu\Psi^j$	b_1	1^+	15

$O_M(x) \equiv \bar{\Psi}^i(x)\Gamma_M\Psi^j(x)$, and we refer to them as *mesons*, borrowing terminology from QCD. The index, $M = \mathrm{ps, s, v, t, av, at}$, denotes pseudoscalar, scalar, vector, tensor, axial-vector, and axial-tensor mesons, respectively. We restrict attention to combinations with flavor indexes $i \neq j$, and for each of them we specify the corresponding irreducible representations of the global (flavor) symmetry group, $SO(6)$. This choice introduces a simplification, as we are only required to compute connected diagrams. For completeness, the table reports also the spin and parity quantum numbers, J^P, associated to each operator. (Charge conjugation is trivial.)

We anticipate here an observation that is going to be useful later in the paper. The vector (v) and tensor (t) operators carry the same $SO(6)$ quantum numbers, and thus interpolate the same meson states in the continuum theory. As will be demonstrated by our numerical results, even on the discretized lattice the masses of these two mesons are statistically compatible. We exploit this property with a GEVP analysis, that allows us to extract the first excited state in the vector meson channel.

B. Two-point correlation functions

We write the zero-momentum correlation functions involving source meson operators, $O_{M'}$, located at $x \equiv (t, \vec{x})$, and sink, O_M, at $y \equiv (t_0, \vec{y})$, as follows

$$C_{M,M'}(t - t_0) = \sum_{\vec{x},\vec{y}} \langle O_M(x) O^\dagger_{M'}(y)\rangle. \tag{20}$$

We omit flavor indexes, $i, j = 1, \ldots, 3$, for which we only consider the nondiagonal terms with $i \neq j$. After applying the appropriate Wick contractions, we write

$$C_{M,M'}(t-t_0) = -\sum_{\vec{x},\vec{y}} \mathrm{Tr}\left[\gamma^5\Gamma_M S_i(x,y)\bar{\Gamma}_{M'}\gamma^5 S_j^\dagger(x,y)\right], \tag{21}$$

where $\bar{\Gamma} \equiv \gamma^0\Gamma^\dagger\gamma^0$ and the trace is taken over color and spinor indices. The hyperquark propagator, $S_j(x,y)$, carrying flavor, j, is defined by

$$S^{AB}_{j,\alpha\beta}(x,y) = \langle \Psi^A_{j\alpha}(x)\bar{\Psi}^B_{j\beta}(y)\rangle, \tag{22}$$

where A, B and α, β are (ordered) pairs of color and spinor indexes, respectively. Without loss of generality, we set the initial time of the source operator to be zero, $t_0 = 0$.

The spectral decomposition of two-point functions in finite (Euclidean) space-time volume, $\tilde{V}$, is discrete. Finite energy eigenvalues, E_n, are labeled by an integer, $n = 0, 1, 2, \ldots$. At sufficiently large Euclidean times, the two-point function is dominated by the contribution of the ground state, with the lowest energy, E_0, while that of excited states has exponentially suppressed. For $M = M'$, this state is the lightest meson, $|M\rangle$, with mass m_M, interpolated by O_M. The correlation function approaches the functional form

$$C_{M,M}(t) \to \frac{|\langle 0|O_M|M\rangle|^2}{2m_M}\left(e^{-m_M t} + e^{-m_M(T-t)}\right). \tag{23}$$

The second term arises from the contribution of backward propagation, with finite temporal extent, T. We then extract the meson masses and the matrix elements by fitting the lattice correlation function to Eq. (23), having restricted the fit range to large Euclidean time.

The matrix elements of vector, (v), and axial-vector, (av), operators (currents), bracketed between the relevant one-meson state and the vacuum, are related to the decay constants of the corresponding mesons, f_v and f_av, respectively. For vanishing three-momentum, $\vec{p} = 0$, they are parametrized as follows:

$$\langle 0|O^\mu_\mathrm{v}|\mathrm{v}\rangle = \sqrt{2} f_\mathrm{v} m_\mathrm{v} \epsilon^\mu, \tag{24}$$

$$\langle 0|O^\mu_\mathrm{av}|\mathrm{av}\rangle = \sqrt{2} f_\mathrm{av} m_\mathrm{av} \epsilon^\mu, \tag{25}$$

where ϵ_μ is the polarization four-vector obeying the defining relations $p_\mu\epsilon_\mu = 0$ and $\epsilon^*_\mu\epsilon_\mu = 1$.

The wave-functions of the pseudoscalar mesons overlap with the axial-vector current. We adopt the following definition for the pseudoscalar decay constant, f_ps[6]

$$\langle 0|O^0_\mathrm{av}|\mathrm{ps}\rangle = \sqrt{2} f_\mathrm{ps} m_\mathrm{ps}. \tag{26}$$

---

[6] Analogous conventions and normalizations yield, in QCD, the pion decay constant, $f_\pi \simeq 93$ MeV, in lieu of f_ps.

To determine $f_{\rm ps}$, we calculate $C_{\rm ps,ps}(t)$, as well as the following correlation function:

$$C_{\rm av,ps}(t) \to \frac{f_{\rm ps}\langle 0|O_{\rm ps}|{\rm ps}\rangle^*}{\sqrt{2}}(e^{-m_{\rm ps}t} - e^{-m_{\rm ps}(T-t)}). \qquad (27)$$

By combining these correlation functions, $C_{\rm ps,ps}$ and $C_{\rm av,ps}$, and exploiting the PCAC relation, we also define the PCAC mass, $am_{\rm PCAC}$ (see Appendix D), which provides a useful definition of the hyperquark mass, in place of the (additively renormalized) Wilson bare mass, am_0.

The decay constants, extracted from lattice matrix elements, must be renormalized and matched to their continuum counterparts. We adopt a renormalization procedure based on the analytical evaluation of 1-loop integrals in lattice perturbation theory with Wilson fermions, in the $\overline{\rm MS}$ scheme [295]. The conversion factors from lattice results, $f_M^{\rm latt}$, to continuum ones, $f_M^{\rm con}$, read as follows:

$$f^{\rm con}_{\rm ps(av)} = \left(1 + C_{\rm R}(\Delta_{\Sigma_1} + \Delta_{\gamma_\mu\gamma_5})\frac{\tilde{g}^2}{16\pi^2}\right)f^{\rm latt}_{\rm ps(av)}, \qquad (28)$$

$$f^{\rm con}_{\rm v} = \left(1 + C_{\rm R}(\Delta_{\Sigma_1} + \Delta_{\gamma_\mu})\frac{\tilde{g}^2}{16\pi^2}\right)f^{\rm latt}_{\rm v}. \qquad (29)$$

In these relations, the eigenvalue of the quadratic Casimir operator for antisymmetric fermions in the $Sp(4)$ gauge theory is $C_{\rm R=as} = 2$. The first numerical factor, $\Delta_{\Sigma_1} = -12.82$, arises from wave function renormalization, while $\Delta_{\gamma_\mu} = -7.75$ and $\Delta_{\gamma_\mu\gamma_5} = -3.0$ descend from vertex renormalization. Perturbative matching can further be improved, as discussed in Ref. [296], by using as definition of the effective coupling the combination $\tilde{g}^2 \equiv g^2/\langle P\rangle$, instead of the bare gauge coupling, where $\langle P\rangle$ is the average plaquette. This approach is effectively equivalent to a mean-field approximation, in which the contributions of tadpole diagrams, which are absent in the continuum theory, are subtracted from the gauge links.

Our numerical calculation of 2-point correlation functions adopts two different and complementary strategies in the construction of source and sink operators. Both procedures are well established in the lattice QCD literature. We have developed and tested these implementations in the present work.

We first consider $Z_2 \otimes Z_2$ stochastic wall sources, with the one-end trick—see, e.g., Ref. [289]—implemented in the HiRep code. In comparison with using naive point sources (delta functions), this choice allows to improve the signal, and determine masses and decay constants with higher precision. We set the number of hits to 3, for all meson correlation functions and for all the ensembles listed in Table I. We verified that this strategy leads to a reduction of statistical noise and the appearance of a cleaner plateau in the effective mass plots at large Euclidean time, compared to the point source, but for the same computational cost.

Having completed these measurements, we select a subset of our ensembles that are useful for our first extrapolation of the meson spectroscopy observables toward the continuum and massless limits. We repeat the measurement of meson masses in these ensembles, by applying a more sophisticated combination of two noise reduction techniques, referred to as APE smearing [293,294] and Wuppertal smearing [290–292], respectively. Both smearing procedures introduce non-nearest-neighbor interactions, and some degree of nonlocality in the measurement process, as we shall explain.

APE smearing is a procedure that smoothens out the UV fluctuations of the gauge links, by combining staples and gauge link iteratively [293]. The smearing procedure is controlled by two parameters, the smearing step-size, $\alpha_{\rm APE}$, and the number of iterations, $N_{\rm APE}$, the choices of which have to be optimized.

Gauge covariant Wuppertal smearing, by contrast, acts on the hyperquark fields and composite operators, by replacing pointlike sources and sinks with extended configurations, defined through an iterative diffusion process [290]. Doing so increases the overlap between smeared interpolating operators and meson eigenstates of interest, by suppressing contributions to correlation functions coming from other states. This procedure requires optimizing (on a channel-by-channel basis, in principle), its step-size, ϵ_W, and the number of iterations, $N_{\rm source}$ and $N_{\rm sink}$, with the aim of maximizing the overlaps, without introducing unwanted systematic errors.

A typical consequence of smearing is that the plateau in the effective mass plots start at earlier Euclidean time. This is particularly useful in measuring the properties of comparatively heavy states, for which one loses signal into noise, at large time. The increase in fitting range also yields a reduction of statistical uncertainties.

A drawback of the adoption of smeared operators is that their nonlocal nature alters the correlation functions in respect to those built of local operators in Eq. (23). One can still extract the decay constants in Eqs. (24)–(26) by performing a simultaneous fit to smeared-smeared and smeared-point correlation functions, but one expects little to no numerical gain, in terms of noise reduction, in doing so. Hence, in our measurement of meson decay constants, we revert to $Z_2 \otimes Z_2$ stochastic wall sources.

Both APE and Wuppertal smearing have been recently implemented in the HiRep code,[7] extensively tested and used for the measurements of spin-1/2 chimera baryons in quenched $Sp(4)$ gauge theories [153,356]. Their use in the study of connected diagram contributions to flavor-singlet meson correlation functions in the $Sp(4)$ theory

---

[7] Specifically, commit ID `1b204b6` [366].

coupled to $N_{\mathrm{f}} = 2$ fundamental and $N_{\mathrm{as}} = 3$ antisymmetric fermions dramatically improves noise control, and makes it possible to perform measurements in this sector of the theory [156]. Application to the same theory further provides a supporting tool for the spectral density approach to lattice spectroscopy [155].

Finally, as anticipated in Sec. IV A, the vector, v, and tensor, t, operators interpolate the same physical states. We exploit this observation to optimize the extraction of the first excited state, by formulating (and solving) a GEVP, taking the form

$$\mathcal{C}(t)v_n(t,t_1) = \lambda_n(t,t_1)\mathcal{C}(t_1)v_n(t,t_1), \tag{30}$$

where the 2×2 matrix-valued correlation function, $\mathcal{C}(t)$, is defined by

$$\mathcal{C}(t) \equiv \begin{pmatrix} C_{\mathrm{v,v}}(t) & C_{\mathrm{v,t}}(t) \\ C_{\mathrm{t,v}}(t) & C_{\mathrm{t,t}}(t) \end{pmatrix}. \tag{31}$$

For fixed $t_1 = 1$, and choosing $t > t_1$, the resulting eigenvalues, $\lambda_0(t,t_1)$ and $\lambda_1(t,t_1)$, exhibit single-exponential decays at large Euclidean time, with the decay rates measured by the masses of ground state and first excited state of the system, respectively.

V. NUMERICAL RESULTS

In this section we report our measurements of masses and decay constants, for the flavored mesons sourced by the operators in Table IV. A first, preliminary analysis of the fermion mass dependence of the relevant observables allows us to identify two distinct regions of parameter space explored by our ensembles, at lower and higher masses, respectively, that exhibit different dynamical properties. We then restrict our attention to ensembles in the lower-mass region, within which the mass dependence of the observables is compatible with expectations from Wilson chiral perturbation theory, truncated at the next-to-leading order (NLO). In the resulting, restricted set of ensembles, we refine our measurements, fix the scale with the gradient flow method discussed in Sec. III C, and perform the first continuum and massless extrapolations of the spectroscopic observables in the theory. We critically discuss our numerical results, by comparing them to the quenched studies reported in Ref. [145].

We deploy a GEVP analysis to extract the mass of the ground and first excited states of the vector mesons, the flavored spin-1 composite states with negative parity. We also measure the ratio $m_{\mathrm{v}}/f_{\mathrm{ps}}$, and compare our results to other related theories. If one takes at face value the phenomenological Kawarabayashi-Suzuki-Riazuddin-Fayyazuddin (KSRF) relation, $m_{\mathrm{v}}^2 = 2g_{\mathrm{v\,ps\,ps}}^2 f_{\mathrm{ps}}^2$ [367,368], these measurements provide a first, naive estimate of the effective coupling, $g_{\mathrm{v\,ps\,ps}}$, associated with the decay of vector into pairs of pseudoscalar mesons.

A. Masses and decay constants

We start by discussing measurements extracted from correlation functions defined with $Z_2 \otimes Z_2$ stochastic wall sources. The complete spectroscopic results are reported in Appendix A, for all the ensembles listed in Table I. In this section, we restrict our discussion to the ensembles with lattice coupling $\beta = 6.7$, for convenience. Similar considerations to those exposed in the following apply to other ensembles as well.

In a typical non-Abelian gauge theory, in which confinement appears at long distances, and is accompanied by the formation of a bilinear fermion condensate, with the associated spontaneous breaking of approximate global symmetries, one expects chiral perturbation theory (χPT) to apply. The pseudoscalar meson is the lightest particle in the spectrum, and its mass is expected to approach zero with the functional form $m_{\mathrm{ps}} \propto \sqrt{m_f}$, where m_f stands for a measurement of the fermion mass.

By contrast, in a theory with IR-conformal dynamics, in which the massless theory does not confine, but rather flows into a new, nontrivial fixed point of the renormalization group flow at long distances, all the meson masses are expected to approach zero with the same exponent, $m_M \propto (m_f)^{1/(1+\gamma^*)}$, with γ^* an anomalous dimension, measured at the IR fixed point [369].

We start by testing the hypothesis of IR conformality. We focus on the pseudoscalar and vector mesons, as the measurements of their mass and decay constant are the most precise available to us. In Fig. 6, we plot the ratio between the pseudoscalar and vector meson masses,

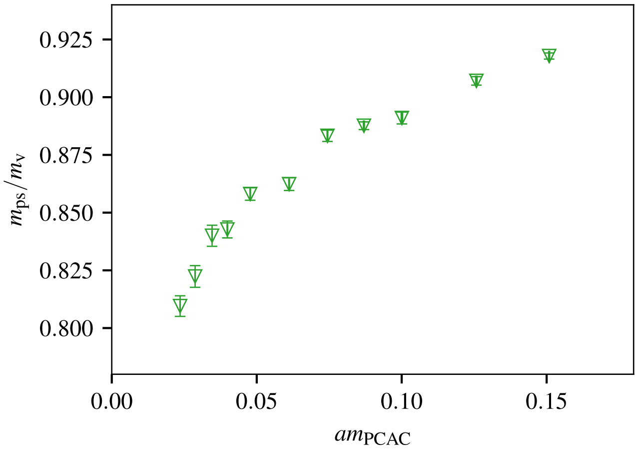

FIG. 6. The ratio between masses of ground-state pseudoscalar and vector mesons, $m_{\mathrm{ps}}/m_{\mathrm{v}}$, extracted using $Z_2 \otimes Z_2$ stochastic wall sources in the definition of the correlation functions. The lattice coupling, $\beta = 6.7$, is held fixed, while the bare mass of the hyperquarks, am_0, varies, and so does the PCAC hyperquark mass, am_{PCAC}.

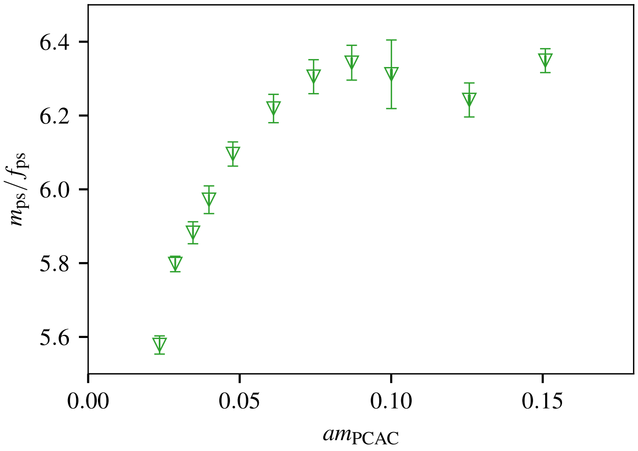

FIG. 7. The ratio between mass and decay constant of ground-state pseudoscalar mesons, $m_{\mathrm{ps}}/f_{\mathrm{ps}}$, extracted using $Z_2 \otimes Z_2$ stochastic wall sources in the definition of the correlation functions. The lattice coupling, $\beta = 6.7$, is held fixed, while the bare mass of the hyperquarks, am_0, varies, and so does the PCAC hyperquark mass, am_{PCAC}.

$m_{\mathrm{ps}}/m_{\mathrm{v}}$. In the available ensembles, the smallest value of this ratio is approximately $m_{\mathrm{ps}}/m_{\mathrm{v}} \sim 0.8$, for the lightest ensemble, which is quite far away from the opening of the kinematical threshold for vector decay to two pseudoscalars. In a IR-conformal theory this ratio should be independent of the fermion mass; conversely we find clear evidence of a variation of this ratio, as the hyperquark mass (represented here by am_{PCAC}) changes. The ratio decreases as the hyperquark mass is reduced, and furthermore, the slope of the resulting curve becomes steeper at lower masses.

We show the numerical results for the ratio of the mass and decay constant of the pseudoscalar meson, $m_{\mathrm{ps}}/f_{\mathrm{ps}}$, in Fig. 7. We find evidence of two distinct dynamical regimes. For $am_{\mathrm{PCAC}} \gtrsim 0.07$, our measurements form a plateau at an approximately constant value, $m_{\mathrm{ps}}/f_{\mathrm{ps}} \sim 6.3$. However, this ratio sharply drops for $am_{\mathrm{PCAC}} \lesssim 0.07$. Combined with our evidence of significant mass dependence for the ratio $m_{\mathrm{ps}}/m_{\mathrm{v}}$, the results for the lighter ensembles contradict the hyperscaling hypothesis, and we infer that the theory in the limit of vanishing hyperquark mass is not IR conformal.

We have evidence in our numerical results suggesting that in the limit of massless hyperquarks of the theory, confinement is taking place, with spontaneous breaking of the (approximate) non-Abelian global symmetry.[8] The resulting low-energy spectrum contains light pseudoscalar meson states identified as the pseudo Nambu-Goldstone bosons. Yet, despite the wide range of hyperquark masses we explored, our results suggest that we expect to see significant deviations from the predictions of leading order (LO) chiral perturbation theory, as none of the ensembles are close enough to the massless limit. We devote the next paragraphs to presenting this evidence and discussing its implications.

In Fig. 8, we present the masses of flavored mesons as a function both of the bare hyperquark mass, am_0, and of the alternative PCAC mass. As expected, over the range of masses considered, the lightest state in the spectrum is the pseudoscalar meson, followed by the vector meson. The tensor mesons are almost degenerate with the vectors, and thus we omit them from the plots, for simplicity. The scalar, axial-vector and axial-tensor flavored mesons are heavier, and the correlation functions from which they are extracted are affected by significant amounts of statistical noise, which is reflected in larger errors in the measurements. The overall trend displayed in Fig. 8 is that the masses grow approximately linearly with the hyperquark mass for $am_{\mathrm{PCAC}} \lesssim 0.07$, but show deviations from such trend for larger fermion masses, $am_{\mathrm{PCAC}} \gtrsim 0.07$.

The decay constants for the pseudoscalar, vector and axial-vector mesons are displayed in Fig. 9. The pseudoscalar decay constant, f_{ps}, is consistently smaller than the vector one, f_{v}. The measurements for the axial-vector decay constants are affected by larger uncertainties, yet their value is close to that of the vectors, when $am_{\mathrm{PCAC}} \lesssim 0.07$. All three decay constants grow approximately linearly with the hyperquark mass, and seem to approach a nonvanishing value if naively extrapolated toward the massless limit. This observation further disfavors the hypothesis that the continuum, massless theory is IR-conformal, and is consistent with the expectations of a confining theory with spontaneous breaking of approximate global symmetries.

In Fig. 10 we combine our measurements of the masses of ps, v, s, av, and at mesons, and present them in units of the decay constant of the ps meson, f_{ps}. We display the results as a function of am_{PCAC}. The figure highlights the contrast between the scaling properties of the ps meson, and all the other mesons. This observation further enforces the conclusion that the massless extrapolation of this theory is chirally broken, not IR conformal, and the ps mesons are indeed (light) Goldstone bosons. This therefore justifies the adoption of an analysis strategy that assumes confinement and spontaneous symmetry breaking of (approximate) global symmetry.

In Fig. 11, we show a comparison between measurements in the $Sp(4)$ theory with $N_{\mathrm{as}} = 3$ antisymmetric fermions (for fixed $\beta = 6.7$), and those reported in Ref. [144], for the $Sp(4)$ theory with $N_{\mathrm{f}} = 2$ fundamental fermions (for fixed $\beta = 7.2$). We display the mass squared of the vector mesons, in the two theories, denoted by m_{v}^2 and m_{V}^2, as a function of the mass squared of the pseudoscalar mesons, m_{ps}^2 and m_{PS}^2, respectively. The masses are expressed in units of the gradient flow scale, w_0. In the

---

[8] As we have clear evidence of symmetry breaking, even in naive extrapolations to the massless limit, we do not discuss symmetric mass generation—see Ref. [370] and references therein.

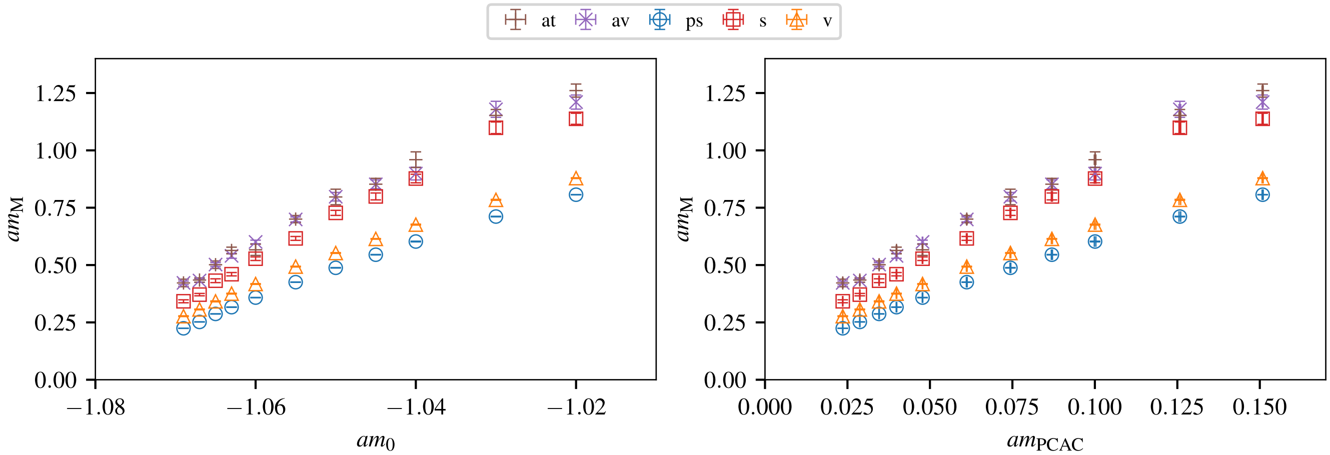

FIG. 8. Masses of flavored mesons, am_M, extracted using $Z_2 \otimes Z_2$ stochastic wall sources in defining the correlation functions, in ensembles with fixed lattice coupling, $\beta = 6.7$, and varying Wilson-Dirac mass of the hyperquarks, am_0 (left panel), or, equivalently, the PCAC hyperquark mass, am_{PCAC} (right panel). The color and marker in the legend denote measurements with $M = \mathrm{ps, v, s, av, at}$ for pseudoscalar, vector, scalar, axial-vector, and axial-tensor mesons.

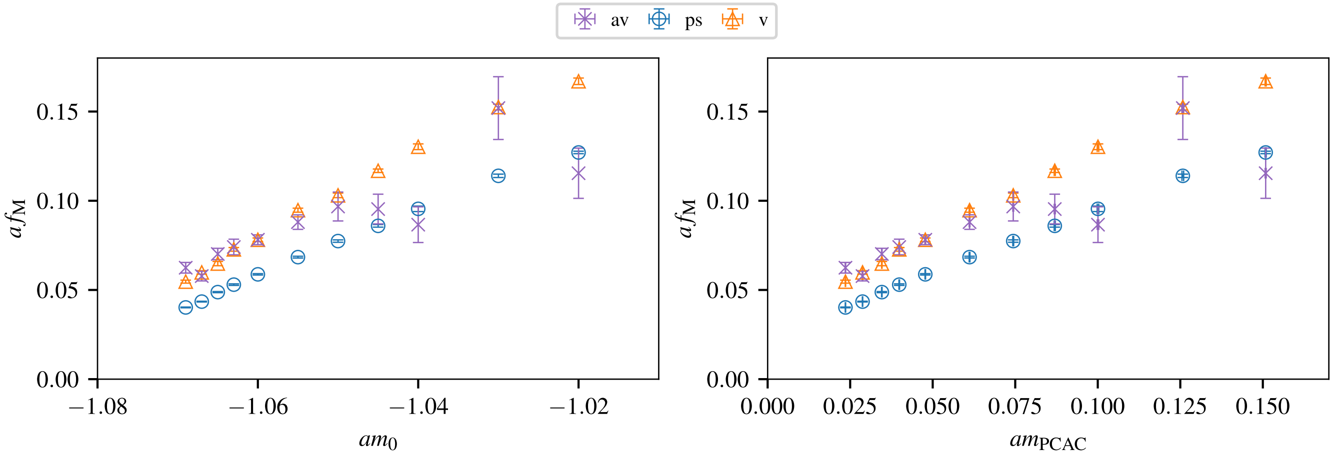

FIG. 9. Decay constants of flavored mesons, af_M, extracted using $Z_2 \otimes Z_2$ stochastic wall sources in the definition of the correlation functions. We display only results obtained in ensembles with lattice coupling $\beta = 6.7$, and vary the Wilson-Dirac mass of the hyperquarks, am_0 (left panel), or, equivalently, the PCAC hyperquark mass, am_{PCAC} (right panel). The color and marker in the legend denote measurements with $M = \mathrm{ps, v, av}$ for pseudoscalar, vector, axial-vector mesons.

$N_{\mathrm{f}} = 2$ theory, $\hat{m}_{\mathrm{V}}^2$ clearly displays a linear dependence on $\hat{m}_{\mathrm{PS}}^2$, over a wide range of different values for the masses. In the case of the $N_{\mathrm{as}} = 3$ theory, on the other hand, the figure shows that both the pseudoscalar and vector mesons are heavier, in respect to the $N_{\mathrm{f}} = 2$ case, and hence the extrapolation toward the massless limit is less reliable. We note that, when we express the mass measurements in lattice units, both datasets span the similar mass ranges, $0.04 \lesssim (am_{\mathrm{ps,PS}})^2 \lesssim 0.7$, and can be shown to be well described by polynomial functions with an appropriate massless limit, as discussed with our preliminary results in Ref. [160]. However, care should be taken in performing the massless extrapolation, setting the scale with w_0 highlights that the physical scale of the masses is far away from the massless limit.

Furthermore, only for the lightest ensembles, those with $am_{\mathrm{PCAC}} \lesssim 0.07$, does one see evidence of an increase of $\hat{m}_{\mathrm{v}}^2$ with $\hat{m}_{\mathrm{ps}}^2$. Conversely, an unexpected qualitative behavior appears for the measurements in heavier ensembles, those with $am_{\mathrm{PCAC}} \gtrsim 0.07$, which cluster together in a small region of parameter space. We conservatively discard these heaviest ensembles from the rest of the subsequent analysis, attributing their behavior to artefacts of the lattice theory, when used far from the continuum and massless limits.

The mass dependence of the Wilson flow governs the qualitative changes observed in Fig. 11. Ultimately, this phenomenon descends from the dynamics of the theory. We have presented convincing evidence supporting an interpretation of long distance data in terms of confinement with

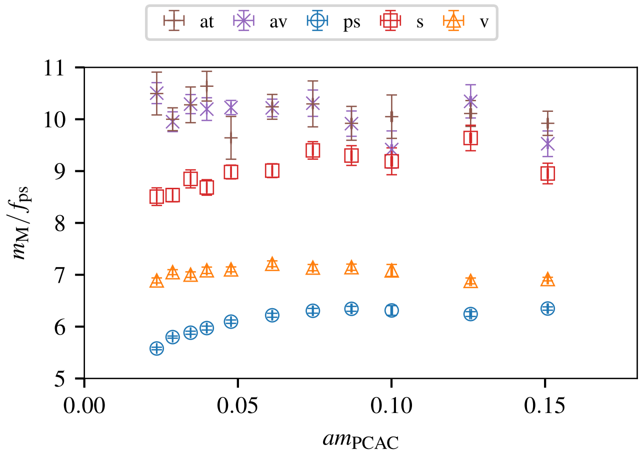

FIG. 10. Mesons masses, expressed in units of the pseudoscalar decay constant, f_{ps}, extracted using $Z_2 \otimes Z_2$ stochastic wall sources in the definition of the correlation functions. We display only results obtained in ensembles with lattice coupling $\beta = 6.7$, and vary the Wilson-Dirac mass of the hyperquarks, am_0, or, equivalently, the PCAC hyperquark mass, am_{PCAC}. The color and marker in the legend denote measurements with $M = \mathrm{ps}, \mathrm{v}, \mathrm{s}, \mathrm{av}, \mathrm{at}$ for pseudoscalar, vector, scalar, axial-vector, and axial-tensor mesons.

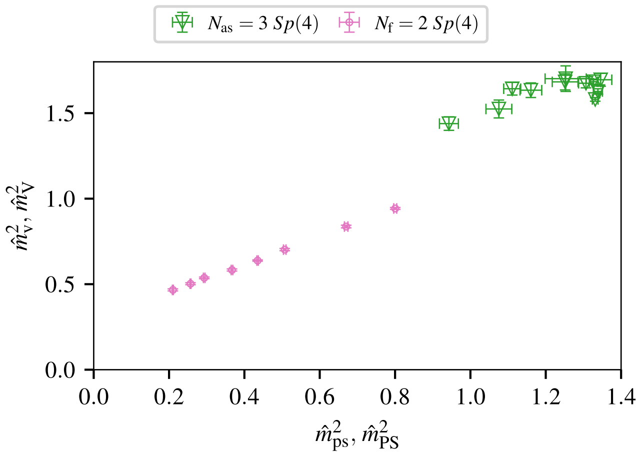

FIG. 11. The square of the masses of vector mesons in the $Sp(4)$ theory coupled to $N_{\mathrm{as}} = 3$ Dirac fermions transforming in the antisymmetric representation, m_{v}^2, as a function of the pseudoscalar masses, m_{ps}^2 (along the abscissa), and the $Sp(4)$ theory with $N_{\mathrm{f}} = 2$ fermions transforming in the fundamental, m_{V}^2, as a function of the pseudoscalar masses, m_{PS}^2 (along the abscissa). Numerical data on the $N_{\mathrm{f}} = 2$ theory with the fixed lattice coupling of $\beta = 7.2$ is taken from Ref. [144], and the measurements displayed for the $N_{\mathrm{as}} = 3$ theory have been performed on ensembles with $\beta = 6.7$. Both vector and pseudoscalar masses are expressed in units of the Wilson flow scale, w_0.

spontaneous symmetry breaking. Yet, the ratios $m_{\mathrm{ps}}/m_{\mathrm{v}}$ and $m_{\mathrm{ps}}/f_{\mathrm{ps}}$ vary at most by about 15%, while am_{ps} spans a wide range, with the largest values about $3 \div 4$ times larger than the smallest available ones. The slow evolution of dimensionless ratios, visible even at smaller hyperquark masses, might be a consequence of the nontrivial properties associated with near-conformal dynamics. We relegate to Appendix C a more extensive set of results, in particular by including measurements obtained at different values of β.

Despite all these cautionary remarks, the six lightest ensembles with $\beta = 6.7$ do exhibit the expected behavior, $\hat{m}_{\mathrm{v}}^2$ depending linearly on $\hat{m}_{\mathrm{ps}}^2$, as shown in Fig. 11. Similar results hold for the other available ensembles. Based on our investigation of the ensembles with $\beta = 6.65$ and $\beta = 6.7$, we consistently find that the aforementioned linear behavior appears when $am_{\mathrm{ps}} \lesssim 0.45$, and we apply this upper bound to restrict the available ensembles, even those for which we do not have enough independent measurements to carry out a fixed-β analysis. With the resulting, restricted set of ensembles, we repeat and refine the measurements by implementing noise-reduction techniques (smearing), and perform a first massless and continuum extrapolation.

We close this subsection with a technical, but important, comment on the limitations of our calculations. As we saw in Fig. 7, there appears to be a maximum value in the ratio of $m_{\mathrm{ps}}/f_{\mathrm{ps}}$. Similarly, the masses of composite states, expressed in units of the gradient flow scale, w_0, are bounded from above, as shown in Fig. 11. These upper bounds can be exceeded only if the lattice coupling increases, as shown in Appendix C. Alas, numerical studies of finer lattices are hindered by the difficulties related with topological freezing. In the opposite direction, exploring small masses, $\hat{m}_{\mathrm{ps}}$, requires using larger lattice sizes, in order to overcome finite volume effects. This is not feasible, at the present time, with realistic computing resources. In summary, the ensembles we reported here provide a good representation of the region of parameter space that is accessible to us with the technology deployed for this study. Compared to the $Sp(4)$ theory with $N_{\mathrm{f}} = 2$, such a region is far more restricted, and, to gain further numerical progress in the $N_{\mathrm{as}} = 3$ theory, we will require to improve the action, possibly by adopting also a different formulation for the fermions.

B. Continuum extrapolations

We adopt fitting *Ansätze* inspired by the NLO Wilson chiral perturbation theory to perform continuum extrapolations in which we combine the available lattice data obtained at six different beta values, $\beta = 6.6$, 6.65, 6.7, 6.75, 6.8, and 6.9. We also assume a linear dependence on $\hat{m}_M^2$ of the measurements performed in ensembles with different masses. As discussed in Sec. V A, we restrict attention to ensembles in which $am_{\mathrm{ps}} \lesssim 0.45$. We refine the measurement of the masses of the mesons by applying APE and Wuppertal smearing. We extract the masses of the first excited states of vector mesons using the GEVP method, as explained in Sec. IV B. For the decay constants, we retain the formulation of the correlation functions in terms of

TABLE V. Fit coefficients appearing in NLO Wilson chiral perturbation theory, Eqs. (32) and (33). We also present the normalized chi-square values, $\chi^2/\mathrm{N_{d.o.f.}}$, associated with the individual fits.

M	$\hat{f}^2_{M,\chi}$	L^f_{M}	W^f_M	$\chi^2/\mathrm{N_{d.o.f.}}$
ps	0.01769(97)	0.913(88)	−0.0130(17)	0.41
v	0.0464(37)	0.47(10)	−0.0374(68)	1.55
av	0.087(14)	0.00(14)	−0.089(28)	1.70

M	$\hat{m}^2_{M,\chi}$	L^m_{M}	W^m_M	$\chi^2/\mathrm{N_{d.o.f.}}$
v	0.644(24)	1.570(81)	−0.676(33)	0.28
t	0.637(24)	1.604(85)	−0.692(33)	0.38
av	1.841(98)	0.741(76)	−1.14(17)	1.36
at	2.37(12)	0.475(58)	−1.54(19)	2.66
s	1.098(79)	1.27(14)	−0.51(13)	7.98
v′	3.41(44)	0.40(13)	−0.90(68)	4.36

$Z_2 \otimes Z_2$ stochastic wall sources. The functional dependence we assume for the observables is the following:

$$\hat{m}^2_M = \hat{m}^2_{M,\chi}(1 + L^m_M \hat{m}^2_{\mathrm{PS}}) + W^m_M \hat{a}, \qquad (32)$$

$$\hat{f}^2_M = \hat{f}^2_{M,\chi}(1 + L^f_M \hat{m}^2_{\mathrm{PS}}) + W^f_M \hat{a}, \qquad (33)$$

where $\hat{m}_{M,\chi}$, $\hat{f}_{M,\chi}$, L^m_M, and W^m_M are the low-energy constants (LECs) determined with the fits.

The resulting best-fit values of these LECs are presented in Table V. The values of $\hat{m}^2_{M,\chi}$ and $\hat{f}^2_{M,\chi}$ correspond to the massless and continuum extrapolations of meson masses and decay constants. We must utilize caution in using and interpreting these numbers, in view of the considerations exposed in Sec. V A, in particular the long extrapolation toward the massless limit they make use of. Nevertheless, these quantities are finite and positive in the massless limit, $\hat{m}^2_{\mathrm{ps}} \to 0$, and display qualitatively the expected features, in particular the fact that $\hat{m}_{\mathrm{v},\chi} = \hat{m}_{\mathrm{t},\chi} < \hat{m}_{\mathrm{av},\chi}$.

In Figs. 12 and 13, we present our measurements of the meson masses and decay constants, expressed in units of the gradient flow scale. We also display the continuum-limit extrapolations, obtained by using Eqs. (32) and (33), together with the best-fit values in Table V, to subtract finite lattice-spacing corrections. Mass ratios, such as $\hat{m}^2_{\mathrm{v}}/\hat{m}^2_{\mathrm{ps}}$, computed after this subtraction, are larger, as all the W_M coefficients in Table V are negative. The masses of vector and tensor states are compatible with each other, as expected. The axial-tensor mesons are the heaviest states among the ground states, though no statistically significant difference with the axial-vector is present. The scalar meson lies between the vector (tensor) and axial-vector mesons.

We also present the results for the first excited states of the vector mesons. They are heavier than the ground state mesons in all channels considered. This measurement uses the subset of the available ensembles for which there is sufficient numerical data to perform the GEVP analysis successfully. In Fig. 14, we show a summary plot of the continuum extrapolations for the masses of all flavored mesons.

Looking at the decay constants, in Fig. 13, we observe that of the pseudoscalar meson, $\hat{f}_{\mathrm{ps}}$, is the smallest of the three over the whole range of masses considered. It further shows a strong mass dependence, yet the extrapolation toward massless and continuum limits is positive. The decay constant of axial vector meson shows large statistical and systematical uncertainties, hence its extrapolation has to be taken with caution.

While our extrapolations to the massless and continuum limits have to be taken with a grain of salt, especially because of potentially large systematic uncertainties due to the long extrapolations, it is legitimate to compare them to the results of the quenched calculations reported in Refs. [145,154]—see Table III of Ref. [154]. We find good agreement, within statistical errors, for the masses of vector, tensor, axial-vector, and axial-tensor mesons. The noticeable exception is the scalar meson, our value of the mass squared being about 35% smaller than in the quenched case. Our current results for the decay constant squared are about 30% and 15% larger than the in the quenched case, for the pseudoscalar and vector mesons, respectively. For the axial-vector meson we find that the dynamical result is statistically compatible with the quenched one. In summary, the comparison with the quenched results shows that our calculations are robust, and indeed confirm that we are exploring a region of parameter space which is not close to the massless limit. This is suitable for applications to composite Higgs or strongly coupled dark matter models.

C. More about vector mesons

The vector meson subsystem is particularly suitable to our numerical strategy, as we study the region of parameter space in which the decay channels for the decay of the v mesons are kinematically forbidden. Thanks also to the application of the GEVP method, we both obtain good control over statistical errors, and gain access to the first excited state, which we denote as v′. Details can be found in the tables in Appendix A. We devote this section to commenting on these results, and comparing them to those obtained in closely related theories.

A particularly interesting quantity is the ratio between the vector meson mass and the pseudoscalar decay constant, $m_{\mathrm{v}}/f_{\mathrm{ps}}$. As it shows only a mild dependence on the pseudoscalar mass squared, $\hat{m}^2_{\mathrm{ps}}$, as well as the lattice coupling $\hat{a}$, as an exercise we perform a linear fit to the values of $m_{\mathrm{v}}/f_{\mathrm{ps}}$ with a double expansion in $\hat{m}^2_{\mathrm{ps}}$ and $\hat{a}$,

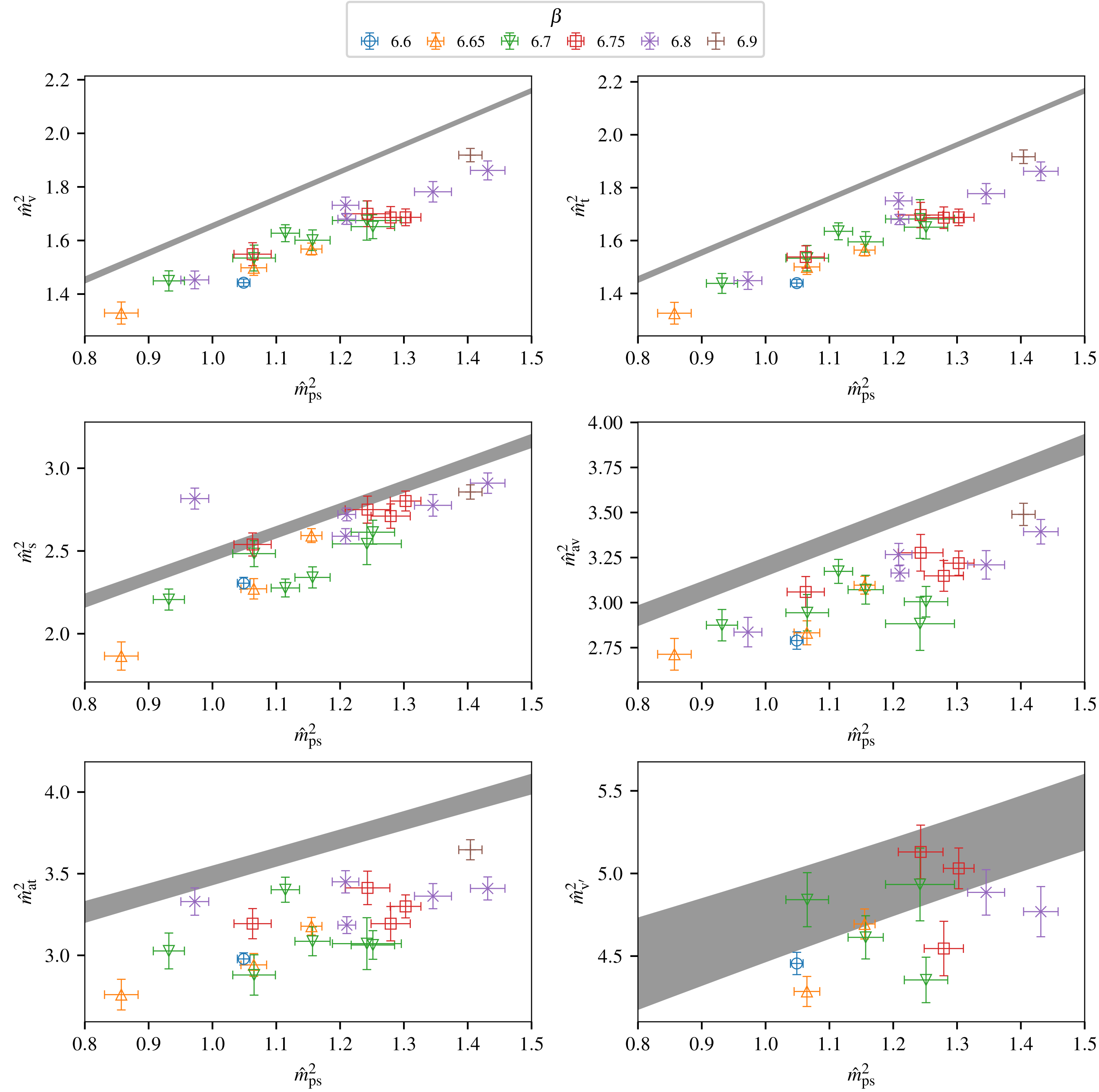

FIG. 12. Square of the meson masses, $\hat{m}_M^2$, expressed in units of the Wilson flow scale, w_0, plotted as a function of the mass squared of the pseudoscalar meson, $\hat{m}_{\rm ps}^2$, in the $Sp(4)$ lattice gauge theory coupled to $N_{\rm as} = 3$ dynamical fermions. These measurements are obtained implementing Wuppertal and APE smearing, and are restricted to ensembles satisfying the upper bound $am_{\rm ps} \lesssim 0.45$. Top to bottom, and left to right, we display the individual measurements of $\hat{m}_{\rm v}^2$, $\hat{m}_{\rm t}^2$, $\hat{m}_{\rm av}^2$, $\hat{m}_{\rm at}^2$, $\hat{m}_{\rm s}^2$, and, finally, $\hat{m}_{\rm v'}^2$, the first excited state sourced by the $({\rm v},{\rm t})$ operators. The value of β is indicated by the color and marker, as shown in the legend. The gray bands denote the result of the extrapolation to the continuum limit, as defined in Eq. (32).

analogous to the continuum extrapolation discussed in the previous section, using the functional dependence

$$\frac{m_{\rm v}}{f_{\rm ps}} = \frac{m_{{\rm v},\chi}}{f_{{\rm ps},\chi}}(1 + c_\ell \hat{m}_{\rm ps}^2) + c_w \hat{a}, \tag{34}$$

and find

$$\frac{m_{{\rm v},\chi}}{f_{{\rm ps},\chi}} = 6.59(11), \qquad c_\ell = 0.069(15), \qquad c_w = -0.10(21). \tag{35}$$

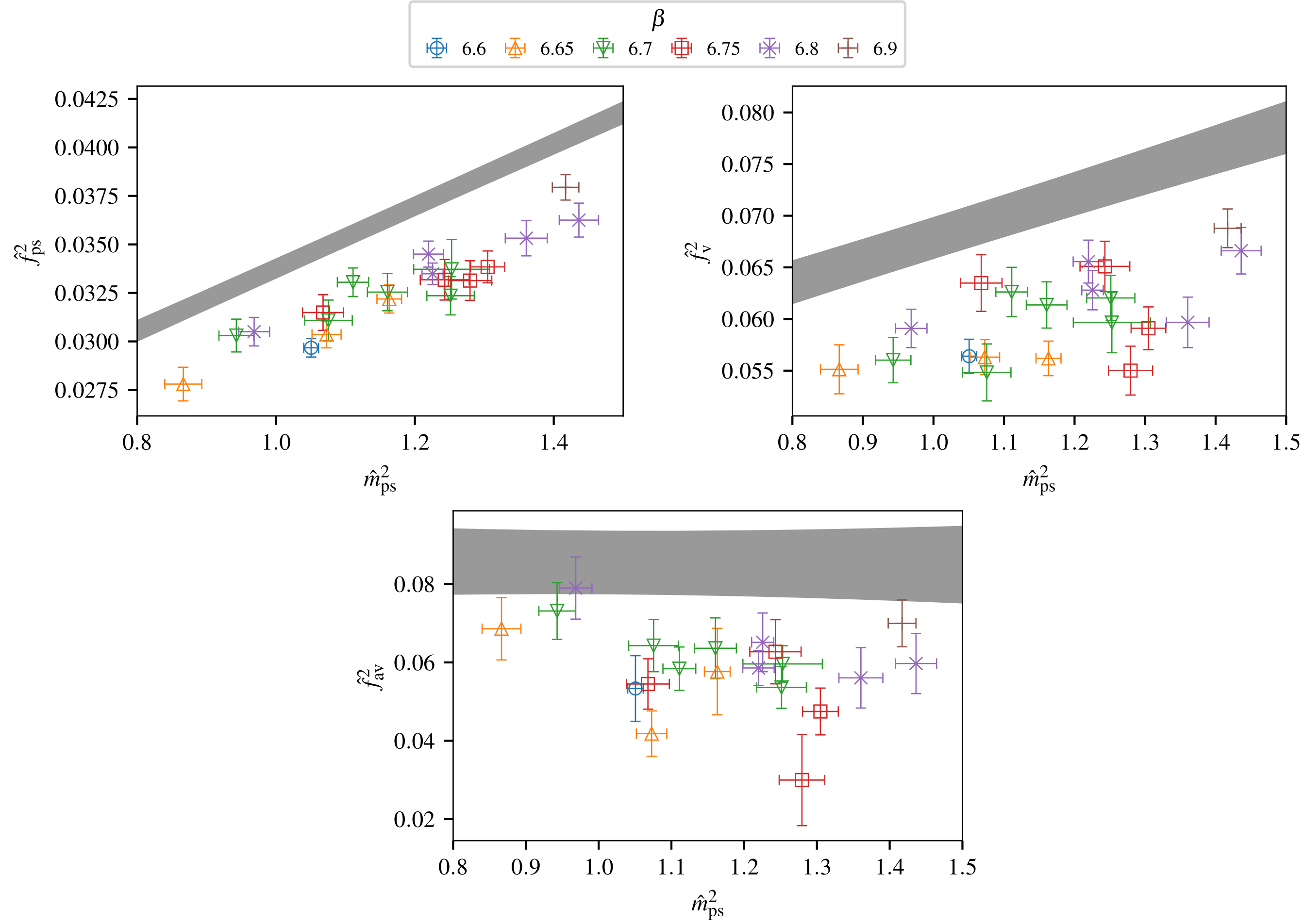

FIG. 13. Square of the decay constants of the mesons, $\hat{f}^2_M$, expressed in units of the Wilson flow scale, w_0, plotted as a function of the mass squared of the pseudoscalar meson, $\hat{m}^2_{\rm ps}$, in the $Sp(4)$ lattice gauge theory coupled to $N_{\rm as} = 3$ dynamical fermions. These measurements of the masses are obtained implementing Wuppertal and APE smearing, and are restricted to ensembles satisfying the upper bound $am_{\rm ps} \lesssim 0.45$. The decay constants are extracted from correlation functions defined with $Z_2 \otimes Z_2$ stochastic wall sources. Top to bottom, and left to right, we display the individual measurements of $\hat{f}^2_{\rm ps}$, $\hat{f}^2_{\rm v}$, and $\hat{f}^2_{\rm av}$, respectively. The value of β is indicated by the color and marker, as shown in the legend. The gray bands denote the result of the extrapolation to the continuum limit, as defined in Eq. (33).

The resulting value of the ratio in the massless and continuum limits can be compared to the one obtained by taking the ratio between the individual extrapolations of the spectral observables, $\hat{m}_{{\rm v},\chi}$ and $\hat{f}_{{\rm ps},\chi}$, reported in Table V. This exercise yields $\hat{m}_{{\rm v},\chi}/\hat{f}_{{\rm ps},\chi} = 6.04(13)$. The discrepancy between these two results points to the fact that the hyperquark masses are still large, hence long extrapolations toward the massless limit are being used, so that subleading terms truncated in the expansion in Eq. (34) are not entirely negligible.

In Fig. 15, we present the continuum extrapolated values of this ratio, $m_{\rm v}/f_{\rm ps}$, which are obtained by subtracting the last term in Eq. (34) from the lattice measurements. For comparison purposes, we also present the corresponding results of the $Sp(4)$ theory with $N_f = 2$ fundamental fermions, taken from Ref. [144]. As the mass ranges considered are quite different, in the two studies, a direct comparison is not possible. Yet, the ratio for the case of $N_{\rm as} = 3$ antisymmetric fermions is consistently smaller than in the $N_{\rm f} = 2$ case.

Somewhat speculatively, we compare this finding to expectations arising from large-N scaling arguments. One expects the meson masses in $Sp(2N)$ theories to scale as $(2N)^0$, while the decay constant in the fundamental and 2-index antisymmetric representation can be argued to scale as the square root of the dimension of the representation, hence as $\sqrt{2N}$ and $\sqrt{(2N+1)(N-1)}$, respectively, by generalizing the arguments in Ref. [371]. Furthermore, various lattice calculations in strongly coupled gauge theories with different gauge group and fermion content suggest that $m_{\rm v}/f_{\rm ps}$ might be independent of the number of fermions, at least in the confined phase of

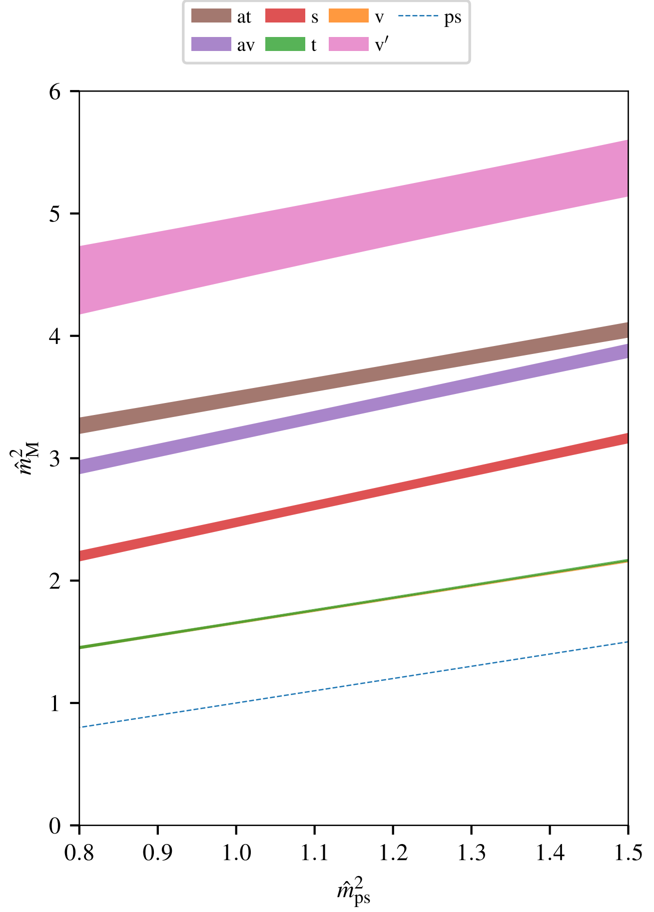

FIG. 14. Summary plot of the meson spectrum in the continuum limit, obtained by applying the *Ansätze* in Eq. (32), inspired by NLO Wilson chiral perturbation theory, to the $Sp(4)$ theory with $N_{\rm as} = 3$ fermions. The masses have been measured using a combination of APE and Wuppertal smearing, on ensembles restricted to a comparatively low mass regime. The colored bands represent the uncertainty of the extrapolation of the fitting results. Lightest to heavier, we display, as a function of the pseudoscalar mass squared, the mass squared of the pseudoscalar (ps), vector (v) and tensor (t), scalar (s), axial-vector (av), axial-tensor (at), and the first-excited state of vector (v′) mesons.

the gauge theory [372–374]. If we take these scaling relations to hold also for $Sp(4)$, we arrive at the prediction that the ratio, $m_{\rm v}/f_{\rm ps} = \sqrt{4/5}m_{\rm V}/f_{\rm PS} \simeq 0.89 m_{\rm V}/f_{\rm PS}$, which is consistent with what we observe numerically in Fig. 15.

Even more speculatively, this ratio, $m_{\rm v}/f_{\rm ps}$, can be used to provide a rough estimate of the on-shell coupling constant associated with the decay of the vector into two pseudoscalar mesons, $g_{\rm v\,ps\,ps}$, via the phenomenological KSRF relation, $g_{\rm v\,ps\,ps} = m_{\rm v}/\sqrt{2}f_{\rm ps}$ [367,368]. In the continuum and massless limits, our numerical results yield $g_{\rm v\,ps\,ps} = 4.656(80)$, which is smaller than the QCD value of ~5.9 [375] and the one in the $Sp(4)$ gauge theory with two fundamental fermions, $m_{\rm V}/\sqrt{2}f_{\rm PS} = 5.72(18)(13)$ [144]. It would be interesting to perform a direct measurement of the coupling $g_{\rm v\,ps\,ps}$, which requires to study the theory with lower hyperquark masses.

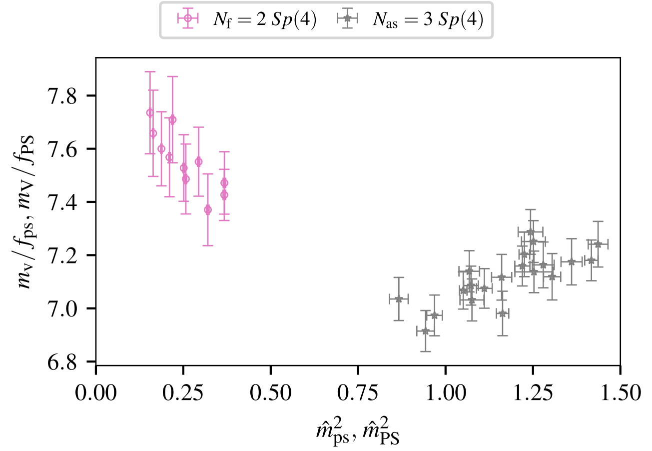

FIG. 15. The ratio between vector meson mass and pseudoscalar decay constant, $m_{\rm v}/f_{\rm ps}$, extrapolated to the continuum limit by means of our simplified WχPT best-fit results, as a function of the mass squared of the pseudoscalar, $\hat{m}^2_{\rm ps}$, expressed in units of the Wilson flow, w_0. For comparison purposes, besides the results for the $Sp(4)$ with $N_{\rm as} = 3$ obtained in this work, we also present those for the $Sp(4)$ theory with $N_{\rm f} = 2$ fundamental Dirac flavors, $m_{\rm V}/f_{\rm PS}$ as a function of $\hat{m}^2_{\rm PS}$, taken from Ref. [144].

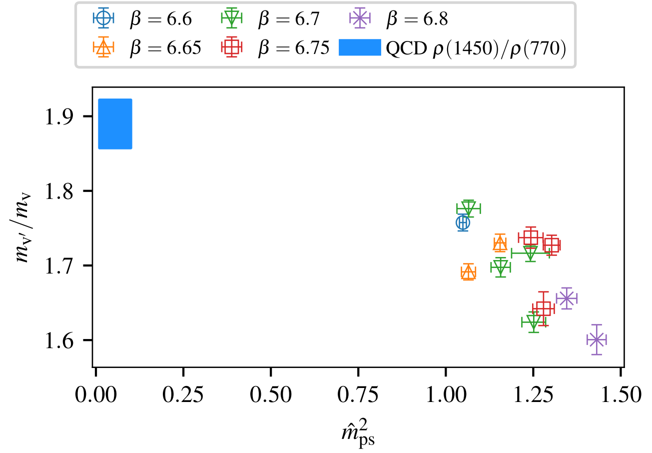

FIG. 16. The mass ratio between the ground and first excited states of the vector meson, $m_{\rm v'}/m_{\rm v}$. The value of β is indicated by the color and marker, as shown in the legend. The blue rectangle denotes the QCD value for $\rho(1450)$, whose width represents the experimental uncertainty.

Finally, in Fig. 16, we present our results for the ratio between the mass of the ground state and the first excited state of the vector meson, $m_{\rm v'}/m_{\rm v}$, for all available values of the bare coupling and hyperquark mass for which the GEVP analysis yields statistically significant results. We uncover clear evidence that this ratio depends on the mass of the pseudoscalar meson, increasing toward the massles limit. Yet, this measurement is affected by non-negligible systematic effects, arising from the fact that the determination of the first-excited states, even with the GEVP method, is limited by the short time extent for the plateau. We hence do not try to model the dependence of this ratio of the lattice parameter, but only compare to the analogous quantity in QCD. For all the ensembles our measurements yield a smaller ratio than the QCD value obtained from experimental results, $m_{\rho(1440)}/m_{\rho(770)} \simeq 1.89(32)$ [375].

VI. SUMMARY AND OUTLOOK

We reported the results of an extensive numerical study of the $Sp(4)$ (hypercolor) lattice gauge theory coupled to $N_{\mathrm{as}} = 3$ Dirac fermions transforming in the two-index antisymmetric representation of the gauge group. The enhanced global $SU(6)$ symmetry acting on the fermions is broken to its $SO(6)$ subgroup because of the presence of nonzero (degenerate) hyperquark masses and the formation of hyperquark condensate. The corresponding continuum theory is of interest to the model building community, as it may serve as an ultraviolet realization of a class of composite Higgs models with top partial compositeness. Alternatively, it can give rise to a candidate composite dark matter model.

The Euclidean, four dimensional lattice theory is formulated in terms of the (unimproved) plaquette action, coupled to Wilson fermions. We explored the two-dimensional parameter space of the lattice theory, and identified the presence of a line of first-order bulk phase transitions, terminating at the critical lattice coupling $\beta^c \simeq 6.45$. We conducted a preliminary, finite-volume study, and ascertained that finite-volume corrections to the mass of the lightest mesons have opposite sign in respect to that observed in the literature on $SU(3)$ theories coupled to fundamental matter fields. We found that finite-volume effects are statistically negligible as long as the lattice size satisfies the empirical relation $m_{\mathrm{ps}}^{\mathrm{inf}} L \geq 7.5$. We generated gauge ensembles with six different values of lattice coupling, $\beta > \beta^c$, and a broad range of hyperquark masses, am_0, with volumes sufficiently large to satisfy the relation $m_{\mathrm{ps}}^{\mathrm{inf}} L \geq 7.5$.

We adopted the gradient (Wilson) flow method for the purpose of setting the scale, and as a noise reduction technique in the computation of the topological charge. As observed in earlier lattice studies of new physics scenarios, the Wilson flow scale displays strong dependence on the hyperquark mass. The choices of lattice parameters used for this study are good representatives of the portion of parameter space that is accessible with the type of lattice action and algorithms we deployed. We saw hints of topological freezing in the available ensembles with lightest masses and largest couplings. The masses of the mesons, the pseudoscalar ones in particular, are comparatively large. The decay of the lightest vector meson into pairs of pseudoscalars is kinematically forbidden. To be able to produce and analyse ensembles testing the lattice parameter space close to the massless and continuum limit would require a drastic change of simulation strategy. Nevertheless, this is the main regime of interest to composite Higgs models and strongly interacting dark matter, hence our results have applicability to new physics models.

We reported our determination of masses and decay constants of composite states interpolated by flavored hyperquark bilinear operators (mesons). In the lightest ensembles available, we find clear evidence of mass-dependence in dimensionless combinations, such as the ratio of mass and decay constant of the lightest pseudoscalar particle, $m_{\mathrm{ps}}/f_{\mathrm{ps}}$. This is inconsistent with the hyperscaling hypothesis, motivated by IR conformal dynamics. We have evidence that the theory displays confinement, accompanied by spontaneous breaking of its (approximately) global symmetries. This is the main result of this paper. We also performed a preliminary analysis of the available data in light of dEFT, as a test of near-conformal dynamics in the confining theory. Such exercise proved inconclusive, with available ensembles.

We find that the mass squared and the decay constant squared of composite states, measured at fixed lattice coupling, β, exhibit a linear dependence on the pseudoscalar mass squared, in all the ensembles in which $am_{\mathrm{ps}} \lesssim 0.45$. We therefore perform continuum and massless extrapolations of our measurements, restricted to these (lighter) ensembles. We first express our measurements in units of the Wilson-flow scale. Inspired by Wilson chiral perturbation theory, we then adopt a fit *Ansatz* for the masses, $\hat{m}_{\mathrm{M}}^2$, and the decay constants, $\hat{f}_{\mathrm{M}}^2$, that is linear in both $\hat{m}_{\mathrm{ps}}^2$ and $\hat{a}$. The resulting linear fit well describes the numerical data. Yet, the massless extrapolations are rather long, and hence the results of this analysis might be affected by significant systematic extrapolation effects.

Our results for the masses of mesons, extrapolated to the continuum and massless limits, are overall comparable to the quenched results reported in Ref. [154]. Yet, the discrepancies are about 20% for the scalar mesons. For pseudoscalar and vector meson decay constants, results obtained with dynamical fermions are larger than the quenched case. We pay particular attention to the vector meson states, for which we develop a bespoke GEVP analysis that allows to extract the masses of both the ground and first excited states.

In the future, it would be interesting to explore the region of parameter space closer to the massless limit. By doing so, it should be possible to improve significantly our control over the massless extrapolation, and hence our spectroscopic results. While doing so may not be a priority for the phenomenological purposes related to composite Higgs and dark matter model building, it would be valuable as a way to address the more general theoretical question of understanding whether this theory lies close to the lower edge of the conformal window. To do so, it will be necessary to introduce more sophisticated versions of the lattice theory, involving improvement, and possibly modifying our treatment of fermions.

Furthermore, it would be of interest to measure the properties of mesons that do not carry flavor, in particular the masses of the lightest scalar and pseudoscalar flavor singlets. The former might be a candidate dilaton, with applicability to alternative models of electroweak symmetry breaking. The latter might be of interest as an axion, which could play a role in a different type of dark matter models. In either case, pursuing these goals would require significant new investment in software development, optimization, and testing, and in computing resources. We leave all these endeavors for the future.

Finally, we envision a complementary, equally ambitious, research programme of study of the phase space of the theory. There is not a sign problem, given the real nature of the fermion representations, hence its behavior in the presence of a (isospin) chemical potential can be studied numerically, from first principles. Even at zero chemical potential, as this might be used as a model of a new dark sector it is of general interest to understand whether this theory undergoes a first-order deconfinement phase transition at high temperature. If this is the case, bubble dynamics may leave a relic stochastic background of gravitational waves, as mentioned in the introduction—see also Ref. [376].

The highly challenging goal of measuring, in strongly coupled theories, those parameters that enter into the calculation of the power spectrum of gravitation waves is currently being pursued via several complementary investigation strategies [126–131], that use, for example, of effective tools as the Polyakov-loop [377–385] or the matrix models [386–394]. The Logarithmic Linear Relaxation (LLR) algorithm [395–398] offers a new, alternative opportunity to perform such high precision numerical studies. Finite-temperature studies of Yang-Mills theories using the LLR exist for $Sp(4)$ [142], $SU(3)$ [134,135,139], $SU(4)$ [136,137], and general $SU(N_c)$ [138,141]. It would be interesting to generalize these studies to theories with matter content, such as the one proposed here.

ACKNOWLEDGMENTS

We would like to thank Giacomo Cacciapaglia, Gabriele Ferretti, Thomas Flacke, Anna Hasenfratz, Chulwoo Jung, and Sarada Rajeev, for very helpful discussions during the “PNU Workshop on Composite Higgs: Lattice study and all,” at Haeundae, Busan, in February 2024, where preliminary results of this study were presented. We also thank Will Detmold, Alberto Ramos, and André Walker-Loud for useful discussions. The work of E. B. and B. L. is supported in part by the EPSRC ExCALIBUR program ExaTEPP (Project No. EP/X017168/1). The work of E. B., B. L., and M. P. has been supported by the STFC Consolidated Grant No. ST/X000648/1. The work of E. B. has also been supported by the UKRI Science and Technology Facilities Council (STFC) Research Software Engineering Fellowship EP/V052489/1. The work of D. K. H. was supported by Basic Science Research Program through the National Research Foundation of Korea (NRF) funded by the Ministry of Education (NRF-2017R1D1A1B06033701). The work of D. K. H. was further supported by the National Research Foundation of Korea (NRF) grant funded by the Korea government (MSIT) (2021R1A4A5031460). The work of J.-W. L. is supported by IBS under the Project code, IBS-R018-D1. The work of H. H. and C.-J. D. L. is supported by the Taiwanese MoST Grant No. 109-2112-M-009-006-MY3 and NSTC Grant No. 112-2112-M-A49-021-MY3. The work of C.-J. D. L. is also supported by Grants No. 112-2639-M-002-006-ASP and No. 113-2119-M-007-013. The work of B. L. and M. P. has been further supported in part by the STFC Consolidated Grant No. ST/T000813/1. B. L. and M. P. received funding from the European Research Council (ERC) under the European Union’s Horizon 2020 research and innovation program under Grant Agreement No. 813942. The work of D. V. is supported by STFC under Consolidated Grant No. ST/X000680/1. Numerical simulations have been performed on the Swansea University SUNBIRD cluster (part of the Supercomputing Wales project) and AccelerateAI A100 GPU system, on the local HPC clusters in Pusan National University (PNU), in Institute for Basic Science (IBS) and in National Yang Ming Chiao Tung University (NYCU), and on the DiRAC Data Intensive service at Leicester. The Swansea University SUNBIRD system and AccelerateAI are part funded by the European Regional Development Fund (ERDF) via Welsh Government. The DiRAC Data Intensive service at Leicester is operated by the University of Leicester IT Services, which forms part of the STFC DiRAC HPC Facility (https://dirac.ac.uk/). The DiRAC Data Intensive service equipment at Leicester was funded by BEIS capital funding via STFC capital Grants No. ST/K000373/1 and No. ST/R002363/1 and STFC DiRAC Operations Grant No. ST/R001014/1. DiRAC is part of the National e-Infrastructure.

DATA AVAILABILITY

The data that support the findings of this article [302] and the analysis workflow used to obtain them [303] are openly available.

APPENDIX A: MORE NUMERICAL RESULTS

In this appendix, we summarize all the new numerical results on lattice measurements of meson masses and decay constants which have been carried out for this work. We adopted two different strategies for the analysis of the correlation function. Measurement extracted from correlation functions defined with $Z_2 \otimes Z_2$ stochastic wall sources and sinks, for all the ensembles listed in Table I, are tabulated in Tables VI and VII, and are discussed in Sec. V A and Appendix C. We also report the results for the PCAC (unrenormalized) hyperquark mass, $am_{\rm PCAC}$, and for the quantities, $m_{\rm ps}L$ and $f_{\rm ps}L$. To facilitate comparison with phenomenological models and applications to model building, we find it useful to express the measurements also in units of the decay constant of the pseudoscalar meson, $f_{\rm ps}$, in Table VIII.

As explained in the body of the paper, we select a subset of the ensembles, which we use for the massless and continuum extrapolation, and apply a combination of APE and Wuppertal smearing, to repeat the mass measurements, performing also the extraction of the first-excited states of vector mesons with the GEVP method. The results are tabulated in Table IX, and discussed in Secs. V B and V C. We express them in units of $f_{\rm ps}$, in Table X, in which we also report the ratio between the first excited and ground states of vector meson.

TABLE VI. Hyperquark mass, defined through the PCAC, $am_{\rm PCAC}$, masses and decay constants of flavored spin-0 mesons, in the pseudoscalar (ps) and scalar (s) channels, expressed in lattice units. For the ps mesons, we also express them in units of the spatial extent, as $m_{\rm ps}L$ and $f_{\rm ps}L$. All measurements use $Z_2 \otimes Z_2$ stochastic wall sources and sinks. The decay constants are renormalized using one-loop perturbative matching with tadpole improvement.

Ensemble	$am_{\rm PCAC}$	$am_{\rm ps}$	$af_{\rm ps}$	$am_{\rm s}$	$m_{\rm ps}L$	$f_{\rm ps}L$
ASB0M1	0.08631(27)	0.5640(15)	0.0919(11)	0.820(35)	10.152(27)	1.655(19)
ASB0M2	0.06943(13)	0.48451(74)	0.08092(56)	0.714(20)	11.628(18)	1.942(13)
ASB0M3	0.052539(88)	0.39808(64)	0.06690(39)	0.603(15)	12.738(21)	2.141(13)
ASB1M1	0.11558(25)	0.6797(11)	0.1083(10)	1.006(25)	12.234(19)	1.950(18)
ASB1M2	0.08628(19)	0.5527(11)	0.08901(72)	0.782(34)	9.949(20)	1.602(13)
ASB1M3	0.07723(19)	0.5122(14)	0.0828(12)	0.769(13)	9.219(25)	1.490(21)
ASB1M4	0.05690(11)	0.41476(80)	0.06900(57)	0.623(14)	9.954(19)	1.656(14)
ASB1M5	0.042270(77)	0.33816(61)	0.05689(34)	0.5108(57)	9.469(17)	1.5928(95)
ASB1M6	0.027553(84)	0.25472(66)	0.04563(26)	0.4087(67)	8.151(21)	1.4600(82)
ASB2M1	0.15086(17)	0.80669(61)	0.12706(69)	1.138(24)	12.9070(97)	2.033(11)
ASB2M2	0.12577(25)	0.7114(11)	0.11397(94)	1.098(25)	11.383(17)	1.823(15)
ASB2M3	0.10007(24)	0.6026(15)	0.0955(15)	0.877(19)	10.846(27)	1.718(28)
ASB2M4	0.08697(17)	0.54507(94)	0.08593(73)	0.799(15)	13.082(23)	2.062(18)
ASB2M5	0.07440(13)	0.4880(10)	0.07740(67)	0.727(11)	11.712(24)	1.857(16)
ASB2M6	0.06117(11)	0.42535(79)	0.06840(50)	0.6161(84)	10.208(19)	1.641(12)
ASB2M7	0.047757(77)	0.35813(67)	0.05875(38)	0.5277(78)	10.028(19)	1.645(11)
ASB2M8	0.039866(85)	0.31637(87)	0.05298(43)	0.4601(73)	8.858(24)	1.483(12)
ASB2M9	0.034595(65)	0.28696(65)	0.04878(31)	0.4317(83)	9.183(21)	1.5611(99)
ASB2M10	0.028748(53)	0.25200(54)	0.04347(21)	0.3711(52)	9.072(20)	1.5648(74)
ASB2M11	0.023573(50)	0.22427(48)	0.04020(20)	0.3420(65)	8.074(17)	1.4473(73)
ASB3M1	0.08962(17)	0.54658(92)	0.08402(87)	0.824(16)	9.838(17)	1.512(16)
ASB3M2	0.06421(11)	0.43374(78)	0.06985(53)	0.6520(89)	10.410(19)	1.676(13)
ASB3M3	0.051517(99)	0.36973(98)	0.05950(56)	0.499(12)	8.874(24)	1.428(14)
ASB3M4	0.039302(69)	0.30733(65)	0.05021(35)	0.430(11)	8.605(18)	1.4059(98)
ASB3M5	0.029091(59)	0.25332(61)	0.04350(22)	0.3971(46)	8.106(20)	1.3921(70)
ASB4M1	0.10354(17)	0.59853(92)	0.09217(72)	0.880(10)	9.577(15)	1.475(11)
ASB4M2	0.08184(18)	0.5055(11)	0.07765(77)	0.719(15)	8.087(18)	1.242(12)
ASB4M3	0.059877(85)	0.40516(75)	0.06437(50)	0.5920(70)	9.724(18)	1.545(12)
ASB4M4	0.048377(62)	0.34663(60)	0.05585(36)	0.5123(87)	8.319(14)	1.3404(86)
ASB4M5	0.036719(71)	0.28917(60)	0.04780(30)	0.4414(58)	9.254(19)	1.5296(95)
ASB4M6	0.029649(53)	0.25227(51)	0.04243(21)	0.3721(41)	8.073(16)	1.3577(67)
ASB4M7	0.022517(45)	0.20975(66)	0.03722(20)	0.3641(31)	7.551(24)	1.3401(73)
ASB5M1	0.050683(52)	0.34583(63)	0.05424(34)	0.4945(52)	8.300(15)	1.3017(82)
ASB5M2	0.036389(50)	0.27657(59)	0.04525(24)	0.3906(56)	8.850(19)	1.4482(78)

TABLE VII. Masses and decay constants of spin-1 flavored vector (v) and axial-vector (av) mesons, and masses in the tensor (t) and axial-tensor (at) mesons, in lattice units. All measurements use $Z_2 \otimes Z_2$ stochastic wall sources and sinks. The decay constants are renormalized using the one-loop perturbative matching with tadpole improvement.

Ensemble	$am_{\rm v}$	$af_{\rm v}$	$am_{\rm av}$	$af_{\rm av}$	$am_{\rm t}$	$am_{\rm at}$
ASB0M1	0.6445(22)	0.1265(18)	0.898(30)	0.101(13)	0.6437(33)	0.976(27)
ASB0M2	0.5608(16)	0.1110(12)	0.807(21)	0.0972(91)	0.5630(20)	0.804(30)
ASB0M3	0.4701(16)	0.0922(12)	0.686(16)	0.0897(69)	0.4691(21)	0.686(17)
ASB1M1	0.7558(19)	0.1473(20)	1.126(42)	0.140(24)	0.7542(25)	1.161(39)
ASB1M2	0.6272(21)	0.1211(17)	0.916(22)	0.1113(94)	0.6287(26)	0.932(23)
ASB1M3	0.5835(22)	0.1136(15)	0.821(21)	0.0932(82)	0.5807(38)	0.873(18)
ASB1M4	0.4789(20)	0.0912(12)	0.703(19)	0.0923(85)	0.4749(30)	0.712(41)
ASB1M5	0.4011(15)	0.07748(90)	0.553(12)	0.0668(46)	0.4025(17)	0.558(21)
ASB1M6	0.3197(23)	0.0643(11)	0.484(11)	0.0717(41)	0.3209(37)	0.474(22)
ASB2M1	0.8789(15)	0.1670(18)	1.211(31)	0.115(14)	0.8784(19)	1.261(29)
ASB2M2	0.7843(20)	0.1525(16)	1.179(35)	0.152(18)	0.7825(26)	1.152(26)
ASB2M3	0.6763(21)	0.1303(16)	0.899(28)	0.087(10)	0.6735(28)	0.959(34)
ASB2M4	0.6141(13)	0.11681(97)	0.852(19)	0.0953(83)	0.6127(19)	0.853(26)
ASB2M5	0.5525(17)	0.1030(13)	0.798(19)	0.0968(81)	0.5529(23)	0.797(34)
ASB2M6	0.4933(16)	0.0947(11)	0.699(11)	0.0880(41)	0.4915(25)	0.700(16)
ASB2M7	0.4174(16)	0.07815(99)	0.6008(78)	0.0781(27)	0.4195(21)	0.566(24)
ASB2M8	0.3754(17)	0.0728(10)	0.540(11)	0.0741(44)	0.3752(24)	0.564(15)
ASB2M9	0.3416(20)	0.0648(12)	0.5021(84)	0.0702(32)	0.3443(27)	0.501(16)
ASB2M10	0.3064(17)	0.05983(98)	0.4325(79)	0.0578(27)	0.3054(28)	0.4346(93)
ASB2M11	0.2770(16)	0.05466(84)	0.4223(79)	0.0625(30)	0.2803(26)	0.422(16)
ASB3M1	0.6133(17)	0.1151(14)	0.870(31)	0.107(18)	0.6152(23)	0.843(17)
ASB3M2	0.4945(19)	0.0923(13)	0.691(15)	0.0827(51)	0.4968(22)	0.729(16)
ASB3M3	0.4242(23)	0.0767(14)	0.565(24)	0.0566(97)	0.4246(32)	0.635(24)
ASB3M4	0.3645(17)	0.07033(89)	0.517(11)	0.0690(44)	0.3597(23)	0.541(10)
ASB3M5	0.3095(18)	0.06177(99)	0.4310(92)	0.0572(33)	0.3074(21)	0.441(16)
ASB4M1	0.6587(16)	0.1200(14)	0.934(16)	0.1108(63)	0.6592(21)	0.941(18)
ASB4M2	0.5668(22)	0.1042(15)	0.773(23)	0.084(10)	0.5683(29)	0.759(28)
ASB4M3	0.4639(19)	0.0873(13)	0.652(12)	0.0826(52)	0.4638(28)	0.674(17)
ASB4M4	0.3990(19)	0.0726(12)	0.563(11)	0.0704(46)	0.4001(22)	0.610(14)
ASB4M5	0.3430(16)	0.06546(93)	0.4936(97)	0.0667(38)	0.3426(27)	0.493(13)
ASB4M6	0.3028(15)	0.05849(78)	0.4172(62)	0.0553(21)	0.3011(21)	0.433(12)
ASB4M7	0.2588(16)	0.05181(65)	0.3925(77)	0.0599(29)	0.2583(25)	0.4161(86)
ASB5M1	0.3911(15)	0.0703(10)	0.5481(86)	0.0674(33)	0.3927(16)	0.557(11)
ASB5M2	0.3239(13)	0.06093(71)	0.4560(69)	0.0615(25)	0.3213(21)	0.447(15)

TABLE VIII. Ratio of the masses of flavored mesons to the pseudoscalar decay constant, $m_M/f_{\rm ps}$, measured with $Z_2 \otimes Z_2$ stochastic wall sources and sinks. Decay constants are renormalized with tadpole improved one-loop perturbative matching.

Ensemble	$m_{\rm ps}/f_{\rm ps}$	$m_{\rm s}/f_{\rm ps}$	$m_{\rm v}/f_{\rm ps}$	$m_{\rm t}/f_{\rm ps}$	$m_{\rm av}/f_{\rm ps}$	$m_{\rm at}/f_{\rm ps}$
ASB0M1	6.134(60)	8.92(41)	7.010(75)	7.001(86)	9.77(36)	10.61(34)
ASB0M2	5.988(37)	8.83(25)	6.930(46)	6.958(48)	9.97(27)	9.93(37)
ASB0M3	5.950(29)	9.01(22)	7.027(41)	7.011(43)	10.25(25)	10.26(26)
ASB1M1	6.274(53)	9.29(24)	6.976(62)	6.962(63)	10.39(39)	10.72(38)
ASB1M2	6.210(41)	8.79(38)	7.046(53)	7.064(58)	10.29(26)	10.47(29)
ASB1M3	6.188(74)	9.30(20)	7.05(10)	7.016(99)	9.93(28)	10.55(28)
ASB1M4	6.011(46)	9.02(21)	6.941(58)	6.883(62)	10.19(29)	10.31(59)
ASB1M5	5.945(29)	8.98(12)	7.052(44)	7.076(51)	9.71(23)	9.80(37)
ASB1M6	5.583(28)	8.96(16)	7.007(56)	7.033(92)	10.60(24)	10.39(47)

(Table continued)

TABLE VIII. *(Continued)*

Ensemble	$m_{\rm ps}/f_{\rm ps}$	$m_{\rm s}/f_{\rm ps}$	$m_{\rm v}/f_{\rm ps}$	$m_{\rm t}/f_{\rm ps}$	$m_{\rm av}/f_{\rm ps}$	$m_{\rm at}/f_{\rm ps}$
ASB2M1	6.349(32)	8.95(20)	6.917(35)	6.913(35)	9.53(25)	9.92(23)
ASB2M2	6.242(46)	9.64(25)	6.882(56)	6.866(56)	10.34(32)	10.11(25)
ASB2M3	6.312(93)	9.19(26)	7.08(12)	7.06(12)	9.42(36)	10.05(42)
ASB2M4	6.343(47)	9.30(19)	7.146(60)	7.130(59)	9.91(24)	9.92(33)
ASB2M5	6.305(46)	9.40(17)	7.139(61)	7.143(67)	10.31(25)	10.30(44)
ASB2M6	6.219(38)	9.01(13)	7.212(57)	7.187(63)	10.22(17)	10.24(24)
ASB2M7	6.096(33)	8.98(13)	7.104(47)	7.140(49)	10.23(14)	9.64(41)
ASB2M8	5.972(38)	8.68(15)	7.087(62)	7.082(66)	10.20(22)	10.64(29)
ASB2M9	5.882(30)	8.85(17)	7.003(53)	7.059(69)	10.29(18)	10.28(34)
ASB2M10	5.798(21)	8.54(13)	7.050(48)	7.027(66)	9.95(19)	10.00(22)
ASB2M11	5.578(25)	8.51(17)	6.891(49)	6.972(70)	10.50(20)	10.50(41)
ASB3M1	6.505(61)	9.80(23)	7.300(74)	7.322(77)	10.35(40)	10.04(24)
ASB3M2	6.209(42)	9.33(15)	7.079(56)	7.112(57)	9.89(22)	10.44(25)
ASB3M3	6.214(47)	8.39(20)	7.130(61)	7.135(68)	9.50(42)	10.66(41)
ASB3M4	6.121(36)	8.56(23)	7.259(57)	7.165(68)	10.29(23)	10.77(22)
ASB3M5	5.823(23)	9.13(11)	7.114(50)	7.067(56)	9.91(21)	10.13(37)
ASB4M1	6.494(45)	9.55(13)	7.147(52)	7.151(54)	10.13(19)	10.21(22)
ASB4M2	6.509(56)	9.26(21)	7.300(70)	7.318(71)	9.95(30)	9.77(36)
ASB4M3	6.294(42)	9.20(12)	7.206(60)	7.205(66)	10.13(20)	10.47(26)
ASB4M4	6.206(35)	9.17(17)	7.144(54)	7.164(59)	10.08(21)	10.92(25)
ASB4M5	6.050(30)	9.23(12)	7.176(57)	7.167(71)	10.33(21)	10.32(28)
ASB4M6	5.946(24)	8.77(10)	7.136(47)	7.097(57)	9.83(16)	10.20(29)
ASB4M7	5.635(24)	9.780(95)	6.951(55)	6.939(74)	10.54(21)	11.18(24)
ASB5M1	6.376(33)	9.12(11)	7.210(44)	7.241(50)	10.10(17)	10.26(23)
ASB5M2	6.111(26)	8.63(13)	7.156(46)	7.099(52)	10.08(16)	9.88(35)

TABLE IX. Masses, am_M, of the flavored mesons included in the continuum and massless extrapolations, measured by applying APE and Wuppertal smearing in the definition of the correlation functions. The mass of the first excited state of vector meson, v′, is determined through a GEVP analysis that includes the two, inequivalent, vector and tensor meson operators.

Ensemble	$am_{\rm ps}$	$am_{\rm s}$	$m_{\rm v}$	$am_{\rm t}$	$m_{\rm av}$	$m_{\rm at}$	$m_{\rm v'}$
ASB0M3	0.39776(34)	0.5897(36)	0.46643(59)	0.46591(63)	0.6486(45)	0.6702(26)	0.8198(51)
ASB1M4	0.41334(35)	0.6193(20)	0.48158(48)	0.48095(56)	0.6768(23)	0.6856(30)	0.8333(58)
ASB1M5	0.33690(33)	0.4921(51)	0.39960(62)	0.39990(55)	0.5495(37)	0.5600(38)	0.6759(42)
ASB1M6	0.25334(34)	0.3737(65)	0.31548(59)	0.31502(70)	0.4507(21)	0.4546(41)	⋯
ASB2M6	0.42536(34)	0.6147(21)	0.48865(50)	0.48851(52)	0.6591(39)	0.6655(53)	0.7936(68)
ASB2M7	0.35657(43)	0.5102(56)	0.41402(71)	0.41489(73)	0.5432(79)	0.5608(96)	0.7107(45)
ASB2M8	0.31587(41)	0.4493(33)	0.37160(70)	0.37091(86)	0.5147(29)	0.5159(44)	0.6308(46)
ASB2M9	0.28559(29)	0.4361(14)	0.34276(42)	0.34264(51)	0.4747(28)	0.4696(60)	0.6088(38)
ASB2M10	0.25237(27)	0.3607(25)	0.30498(45)	0.30571(43)	0.4259(19)	0.4410(26)	⋯
ASB2M11	0.22293(24)	0.3431(18)	0.27802(56)	0.27696(58)	0.3916(22)	0.4018(39)	⋯
ASB3M2	0.43338(36)	0.6356(38)	0.49310(72)	0.49329(78)	0.6812(40)	0.6898(47)	0.8517(66)
ASB3M3	0.36971(36)	0.5382(28)	0.42442(59)	0.42449(71)	0.5800(33)	0.5842(60)	0.6969(96)
ASB3M4	0.30733(31)	0.4571(21)	0.35938(52)	0.35904(61)	0.4990(32)	0.5093(23)	0.6244(51)
ASB3M5	0.25275(38)	0.3906(15)	0.30510(65)	0.30402(58)	0.4288(23)	0.4381(25)	⋯
ASB4M3	0.40446(27)	0.5767(22)	0.46126(38)	0.46130(43)	0.6228(19)	0.6243(25)	0.7383(93)
ASB4M4	0.34472(33)	0.4951(18)	0.39669(56)	0.39619(57)	0.5324(23)	0.5449(23)	0.6569(55)
ASB4M5	0.28740(27)	0.4309(16)	0.33855(42)	0.33856(50)	0.4646(20)	0.4662(28)	⋯
ASB4M6	0.25112(28)	0.3675(13)	0.30058(45)	0.30219(43)	0.4129(21)	0.4243(21)	⋯
ASB4M7	0.21017(31)	0.3577(11)	0.25691(49)	0.25652(52)	0.3590(34)	0.3889(22)	⋯
ASB5M1	0.34496(50)	0.4881(25)	0.39154(72)	0.39107(77)	0.5333(28)	0.5343(28)	0.6501(40)
ASB5M2	0.27531(36)	0.3927(17)	0.32183(49)	0.32167(56)	0.4340(28)	0.4437(26)	⋯

TABLE X. Ratio of the masses of the flavored mesons included in the continuum and massless extrapolations, to the pseudoscalar decay constant, $m_M/f_{\rm ps}$. The masses are measured by applying APE and Wuppertal smearing in the definition of the correlation functions. The mass of the first excited state of vector mesons, v′, is determined through a GEVP analysis that includes the two, inequivalent, vector and tensor meson operators. We also report the ratio of the masses of the first-excited and ground states of the vector meson, $m_{\rm v'}/m_{\rm v}$.

Ensemble	$m_{\rm ps}/f_{\rm ps}$	$m_{\rm s}/f_{\rm ps}$	$m_{\rm v}/f_{\rm ps}$	$m_{\rm t}/f_{\rm ps}$	$m_{\rm av}/f_{\rm ps}$	$m_{\rm at}/f_{\rm ps}$	$m_{\rm v'}/f_{\rm ps}$	$m_{\rm v'}/m_{\rm v}$
ASB0M3	5.946(35)	8.814(73)	6.972(42)	6.964(42)	9.696(86)	10.018(70)	12.25(11)	1.758(11)
ASB1M4	5.991(50)	8.975(83)	6.980(59)	6.971(59)	9.809(88)	9.937(95)	12.08(13)	1.730(12)
ASB1M5	5.922(36)	8.650(96)	7.025(44)	7.030(44)	9.659(86)	9.844(88)	11.88(11)	1.691(11)
ASB1M6	5.553(32)	8.19(15)	6.915(40)	6.905(41)	9.879(74)	9.96(11)	⋯	⋯
ASB2M6	6.219(46)	8.987(71)	7.145(53)	7.142(53)	9.637(93)	9.73(10)	11.60(13)	1.624(14)
ASB2M7	6.069(39)	8.68(11)	7.047(47)	7.062(46)	9.25(14)	9.54(17)	12.10(11)	1.716(11)
ASB2M8	5.962(49)	8.480(96)	7.014(57)	7.001(59)	9.716(95)	9.74(11)	11.91(13)	1.698(13)
ASB2M9	5.854(37)	8.939(62)	7.026(46)	7.024(45)	9.732(85)	9.63(13)	12.48(11)	1.776(11)
ASB2M10	5.806(28)	8.299(71)	7.017(36)	7.033(35)	9.799(62)	10.145(68)	⋯	⋯
ASB2M11	5.545(29)	8.533(66)	6.915(37)	6.889(38)	9.740(74)	9.99(11)	⋯	⋯
ASB3M2	6.204(47)	9.099(88)	7.059(55)	7.062(55)	9.753(93)	9.87(10)	12.19(13)	1.727(13)
ASB3M3	6.213(59)	9.045(96)	7.133(69)	7.134(69)	9.75(11)	9.82(14)	11.71(19)	1.642(23)
ASB3M4	6.121(42)	9.104(70)	7.158(49)	7.151(50)	9.938(86)	10.143(83)	12.44(14)	1.737(14)
ASB3M5	5.810(32)	8.980(58)	7.013(40)	6.989(39)	9.856(75)	10.072(81)	⋯	⋯
ASB4M3	6.283(49)	8.959(79)	7.166(55)	7.166(55)	9.675(82)	9.698(81)	11.47(17)	1.601(20)
ASB4M4	6.172(40)	8.865(63)	7.103(47)	7.094(47)	9.532(73)	9.757(77)	11.76(13)	1.656(14)
ASB4M5	6.012(38)	9.014(64)	7.083(45)	7.083(45)	9.720(69)	9.753(80)	⋯	⋯
ASB4M6	5.919(30)	8.662(54)	7.084(38)	7.122(37)	9.730(70)	10.000(73)	⋯	⋯
ASB4M7	5.646(33)	9.609(61)	6.902(41)	6.891(41)	9.64(10)	10.447(81)	⋯	⋯
ASB5M1	6.360(40)	8.999(66)	7.219(46)	7.211(46)	9.833(76)	9.852(76)	11.99(10)	1.660(11)
ASB5M2	6.084(34)	8.677(60)	7.111(40)	7.108(40)	9.590(80)	9.804(76)	⋯	⋯

APPENDIX B: AUTOCORRELATION

The local updates used by the (R)HMC algorithm necessarily lead to residual autocorrelation between the configurations retained in an ensemble. We devote this appendix to estimating the autocorrelation length of such effect, and to explaining the strategy adopted in our data analysis to ensure that our statistical analysis is not comprised by autocorrelation effects. As we shall see this is dependent on the observable. For a given observable, $\mathcal{O}$, we define the autocorrelation function, $C_{\mathcal{O}}(\tau)$, as follows:

$$C_{\mathcal{O}}(\tau) \equiv \sum_{i=1}^{N_{\rm traj}-\tau} \frac{(\mathcal{O}_i - \langle\mathcal{O}\rangle)(\mathcal{O}_{i+\tau} - \langle\mathcal{O}\rangle)}{\mathrm{var}(\mathcal{O})}, \tag{B1}$$

where τ labels the individual trajectory. In Eq. (B1), $\mathrm{var}(\mathcal{O})$ is the ensemble variance of $\mathcal{O}$, and $N_{\rm traj}$ is the total number of trajectories. After visually checking the behavior of $C_{\mathcal{O}}(\tau)$, the exponential autocorrelation time, $\tau^{\mathcal{O}}_{\rm exp}$, is estimated by fitting $C_{\mathcal{O}}(\tau)/C_{\mathcal{O}}(0) = \exp(-\tau/\tau^{\mathcal{O}}_{\rm exp})$.

The first observable we consider is the average plaquette, $\mathcal{P}$, defined in Eq. (6), measured on gauge configuration. The corresponding autocorrelation time, $\tau^{\mathcal{P}}_{\rm exp}$, is then used to determine the separation of trajectories, $\delta_{\rm traj}$, between two neighboring configurations selected for all the measurements of 2-point mesonic correlation functions such that $\delta_{\rm traj} \gtrsim \tau^{\mathcal{P}}_{\rm exp}$. We report our results in Table XI, by tabulating both the values of $\delta_{\rm traj}$ and $\tau^{\mathcal{P}}_{\rm exp}$. We additionally compute the autocorrelation length of the 2-point correlation function of the ps meson, taken at the choice of the Euclidean time at which a plateau appears in the effective mass. We denote this estimate of the autocorrelation as $\tau^{\rm ps}_{\rm exp}$. This measurement provides an alternative way to estimate the effect of autocorrelation in 2-pint functions involving mesons. The resulting values of $\tau^{\mathcal{P}}_{\rm exp}$ and $\tau^{\rm ps}_{\rm exp}$ are reported in Table XI, from which one can conclude that the choice of $\delta_{\rm traj}$ is sufficient to retain independent configurations for all the spectral measurements we performed in this work.

As discussed in Secs. III C and III D, the observables built from flowed fields through the gradient flow, including the action density $\mathcal{E}(t)$ and the topological charge Q, exhibit a long autocorrelation along the HMC trajectories. We calculate autocorrelation functions for the action density at $t = w_0^2$ and the topological charge at $t = L^2/32$, which we denote as $C_{\mathcal{E}}(\tau)$ and $C_Q(\tau)$, by replacing $\mathcal{O}$ in Eq. (B1) with $\mathcal{E}(t = w_0^2)$ and $Q(t = L^2/32)$, respectively. We then estimate the corresponding autocorrelation lengths, $\tau^{w_0}_{\rm exp}$ and $\tau^{Q}_{\rm exp}$, from exponential fits to $C_{\mathcal{E}}(\tau)$ and $C_Q(\tau)$.

TABLE XI. Autocorrelation lengths of the average plaquette, $\tau^{\mathcal{P}}_{\rm exp}$, of the 2-point correlation function of ps meson, $\tau^{\rm ps}_{\rm exp}$, of the energy density at the flow time $t = (w_0/a)^2$, $\tau^{w_0}_{\rm exp}$, and of the topological charge at the flow time $t = L^2/32$, $\tau^{Q}_{\rm exp}$, in units of HMC trajectories. The separations in trajectories between adjacent configurations used for the measurements of spectral quantities and the gradient flow scale are denoted by $\delta_{\rm traj}$ and $\delta^{\rm GF}_{\rm traj}$, respectively.

Ensemble	$\delta_{\rm traj}$	$\tau^{\mathcal{P}}_{\rm exp}$	$\tau^{\rm ps}_{\rm exp}$	$\delta^{\rm GF}_{\rm traj}$	$\tau^{w_0}_{\rm exp}$	$\tau^{Q}_{\rm exp}$
ASB0M1	24	15.3(1.8)	8.7(2.1)	72	74.1(8.2)	69.5(2.9)
ASB0M2	16	10.4(1.2)	4.35(83)	48	43.4(3.9)	130.2(7.8)
ASB0M3	16	10.6(1.3)	8.5(1.7)	112	119(12)	105(11)
ASB1M1	28	15.6(2.0)	6.0(1.3)	84	64.7(4.5)	32.4(3.0)
ASB1M2	20	7.4(1.2)	4.05(79)	100	94.7(5.0)	81.1(5.3)
ASB1M3	16	6.93(79)	7.5(1.6)	80	76.2(3.6)	64.6(2.2)
ASB1M4	16	8.08(67)	3.87(96)	64	77.8(2.6)	273(20)
ASB1M5	12	5.98(45)	4.31(68)	144	120.2(1.0)	115.6(4.4)
ASB1M6	12	5.63(62)	3.06(58)	240	259.0(6.4)	96.4(1.7)
ASB2M1	12	12.5(2.3)	4.98(68)	36	31.4(2.2)	22.9(1.1)
ASB2M2	20	18.3(5.3)	7.3(4.7)	60	62.6(5.5)	54.8(5.5)
ASB2M3	20	8.2(1.5)	8.4(1.7)	120	107.2(5.4)	63.3(5.1)
ASB2M4	20	12.5(1.9)	8.3(1.6)	60	65.4(7.5)	63.5(4.3)
ASB2M5	20	8.30(99)	5.8(1.1)	80	69.5(6.1)	159.2(7.1)
ASB2M6	12	6.09(68)	5.60(91)	144	124.43(93)	170.4(5.6)
ASB2M7	12	6.19(99)	6.5(1.7)	240	324(14)	225.6(7.9)
ASB2M8	20	6.35(52)	5.0(1.0)	160	191.8(5.9)	299.2(8.4)
ASB2M9	12	4.28(46)	4.77(93)	144	127.8(2.7)	61.5(8.3)
ASB2M10	12	5.38(29)	3.96(75)	108	89.3(3.1)	207(13)
ASB2M11	12	5.50(32)	3.80(48)	120	87.1(3.9)	47.5(6.8)
ASB3M1	12	6.36(65)	6.0(1.3)	84	88.7(2.1)	94.4(7.7)
ASB3M2	20	5.38(50)	3.53(85)	120	223(21)	118.3(5.1)
ASB3M3	12	3.64(36)	4.00(78)	96	80.5(1.9)	140.6(8.9)
ASB3M4	8	2.98(19)	4.23(93)	160	155.9(7.4)	348(12)
ASB3M5	8	3.40(43)	2.83(18)	144	125.9(1.6)	569(12)
ASB4M1	12	5.52(75)	2.61(44)	60	60.5(1.0)	30.00(93)
ASB4M2	12	3.92(41)	1.21(47)	84	82.5(2.2)	156.1(9.2)
ASB4M3	12	3.82(21)	4.16(84)	108	75.57(59)	88.1(4.0)
ASB4M4	8	3.44(35)	2.33(38)	104	88.6(1.1)	153.5(6.7)
ASB4M5	12	4.69(25)	4.06(80)	72	60.4(3.2)	491(30)
ASB4M6	12	4.33(31)	5.5(1.0)	84	63.1(1.0)	345(25)
ASB4M7	12	3.37(35)	5.19(97)	192	174(10)	814(52)
ASB5M1	8	3.89(15)	5.1(1.3)	···	···	368(18)
ASB5M2	12	5.95(80)	3.06(53)	72	74.4(2.9)	193(18)

We present the results for $\tau^{w_0}_{\rm exp}$ and $\tau^{Q}_{\rm exp}$ in Table XI. The measurements of the flowed observables have been carried out on the configurations already separated by $\delta_{\rm traj}$ trajectories, leaving a few hundred samples much smaller than $N_{\rm traj}$. We notice that some correlation lengths obtained in this way are much larger than $\delta_{\rm traj}$. In these cases, the exponential function may be insufficient to capture the detailed magnitude of autocorrelation effects. The errors quoted in our results have been estimated through standard bootstrapping technique. Nevertheless, the clear conclusion of this exercise is that the autocorrelation length of flowed observables is substantially larger than that of the average plaquette and the 2-point correlation functions of ps mesons. We use the estimated autocorrelation length, $\tau^{w_0}_{\rm exp}$, for guidance in the selection of the subset for a given ensemble, containing configurations separated by $\delta^{\rm GF}_{\rm traj} \simeq \tau^{w_0}_{\rm exp}$ trajectories, for the measurements of the gradient flow scale, w_0/a.

APPENDIX C: HYPERQUARK MASS DEPENDENCE

In this appendix we provide additional information on the dependence of physical observables on the hyperquark mass. We present our results for the Wilson flow scale, w_0/a, in Fig. 17. As expected, larger values of the lattice

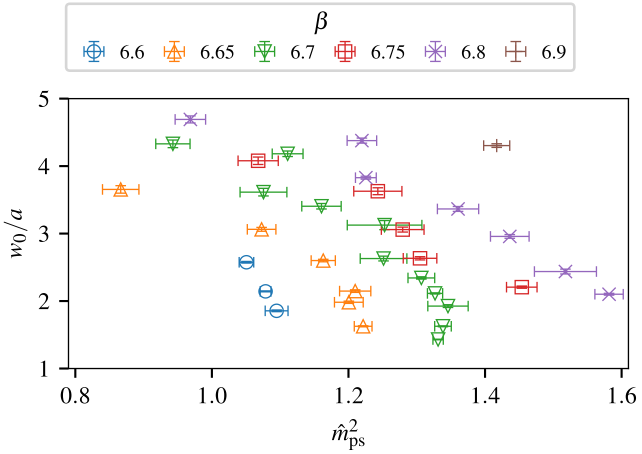

FIG. 17. The Wilson flow scale, w_0/a, as a function of the pseudoscalar mass squared, expressed in units of the Wilson scale, w_0, and denoted as $\hat{m}^2_{\rm ps}$, for all the available choices of lattice coupling, β. The measurement of the pseudoscalar mass is extracted from correlation functions defined with $Z_2 \otimes Z_2$ stochastic wall sources and sinks. The value of β is indicated by the color and marker, as shown in the legend.

coupling, β, generically translate into larger values of w_0/a, for any fixed value of the pseudoscalar mass squared, $\hat{m}^2_{\rm ps}$. But we also find that w_0/a changes substantially as the pseudoscalar mass varies, for fixed β. With a few exceptions (the three heaviest ensembles with $\beta = 6.65$ and the five heaviest with $\beta = 6.7$), we find approximately linear dependence of w_0/a on $\hat{m}^2_{\rm ps}$. In the eight exceptions, all characterized by large values of the hyperquark mass, we find that w_0/a changes significantly, despite the fact that the pseudoscalar mass, $\hat{m}_{\rm ps}$, is approximately constant. In particular, there appears to be an upper bound on the pseudoscalar mass, expressed in units of the Wilson flow scale, at fixed β.

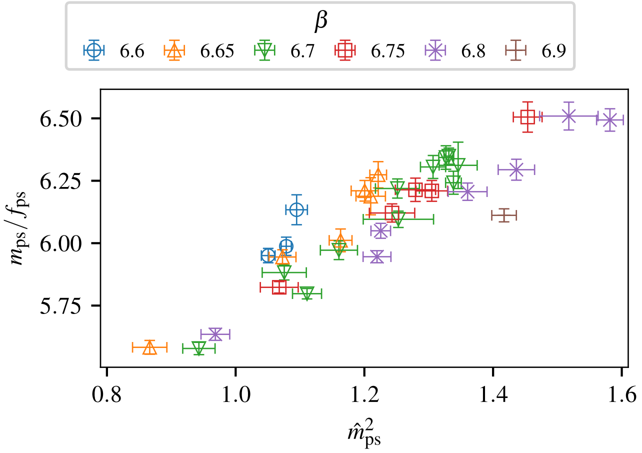

FIG. 18. The ratio between mass and decay constant of the flavored, pseudoscalar mesons, $m_{\rm ps}/f_{\rm ps}$, as a function of the square of the mass of the pseudoscalar, expressed in units of Wilson flow scale. The measurement are extracted from correlation functions defined with $Z_2 \otimes Z_2$ stochastic wall sources and sinks. The value of β is indicated by the color and marker, as shown in the legend.

The ratio between mass and decay constant of the flavored pseudoscalar meson, $m_{\rm ps}/f_{\rm ps}$, is shown in Fig. 18, as a function of $\hat{m}^2_{\rm ps}$, for all the ensembles. As discussed above, the measured values of $\hat{m}^2_{\rm ps}$ at fixed β value are bounded from above. We see that in the case of the heavy ensembles with $\beta = 6.65$ and 6.7, also the ratio $m_{\rm ps}/f_{\rm ps}$ converges, so that these heavier ensembles are, in practical terms, testing the same physical scales.

APPENDIX D: PCAC MASS

In the Wilson-Dirac fermionic action, the hyperquark mass receives additive renormalization. To provide a definition of hyperquark mass that vanishes when the global symmetry is restored, we use a Ward-Takahashi identity, and introduce the PCAC mass. We devote this appendix to providing such definition, and fixing conventions.

Using the PCAC relation, the variation of an operator, $\mathcal{O}$, under the action of an infinitesimal chiral transformation, can be written as

$$\langle 0|\delta_x \mathcal{O}(y)|0\rangle = \langle 0|\{\partial^\mu \mathcal{O}^\mu_{\rm av}(x) + 2m_{\rm PCAC}\mathcal{O}_{\rm ps}(x)\}\mathcal{O}(y)|0\rangle, \tag{D1}$$

where $m_{\rm PCAC}$ is the PCAC mass, while $\mathcal{O}^\mu_{\rm av}(x)$ and $\mathcal{O}_{\rm ps}(x)$ are the axial-vector current and the pseudoscalar density, respectively, defined as

$$\mathcal{O}^\mu_{\rm av}(x) = \bar{\Psi}(x)\gamma^5\gamma^\mu\Psi, \mathcal{O}_{\rm ps}(x) = \bar{\Psi}(x)\gamma^5\Psi. \tag{D2}$$

If one specifies $\mathcal{O}(x) = \mathcal{O}_{\rm ps}(x)$ and $\mu = 0$, and integrates over the spatial coordinates, the left-hand side of Eq. (D1) vanishes, and one finds

$$m_{\rm PCAC} = -\frac{\partial_0\langle \mathcal{O}^0_{\rm av}(t)\mathcal{O}_{\rm ps}(0)\rangle}{2\langle \mathcal{O}_{\rm ps}(t)\mathcal{O}_{\rm ps}(0)\rangle} = -\frac{\partial_0 C_{\rm av,ps}(t)}{2C_{\rm ps,ps}(t)}, \tag{D3}$$

In the case of discretized, Euclidean time, with finite extent, T, as in lattice calculations, after taking into account the asymptotic behavior of the correlation functions, one can define the effective PCAC mass as

$$m^{\rm eff}_{\rm PCAC} \equiv -\frac{m^{\rm eff}_{\rm ps}}{\sinh m^{\rm eff}_{\rm ps}} \frac{C_{\rm av,ps}(t+1) - C_{\rm av,ps}(t-1)}{4C_{\rm ps,ps}(t)}. \tag{D4}$$

We plot the resulting values for $am_{\rm PCAC}$, as a function of the bare mass, am_0, in Fig. 19. We perform polynomial fits to the data, for each choice of lattice coupling, β. We find that a linear fit describes well the results obtained from the

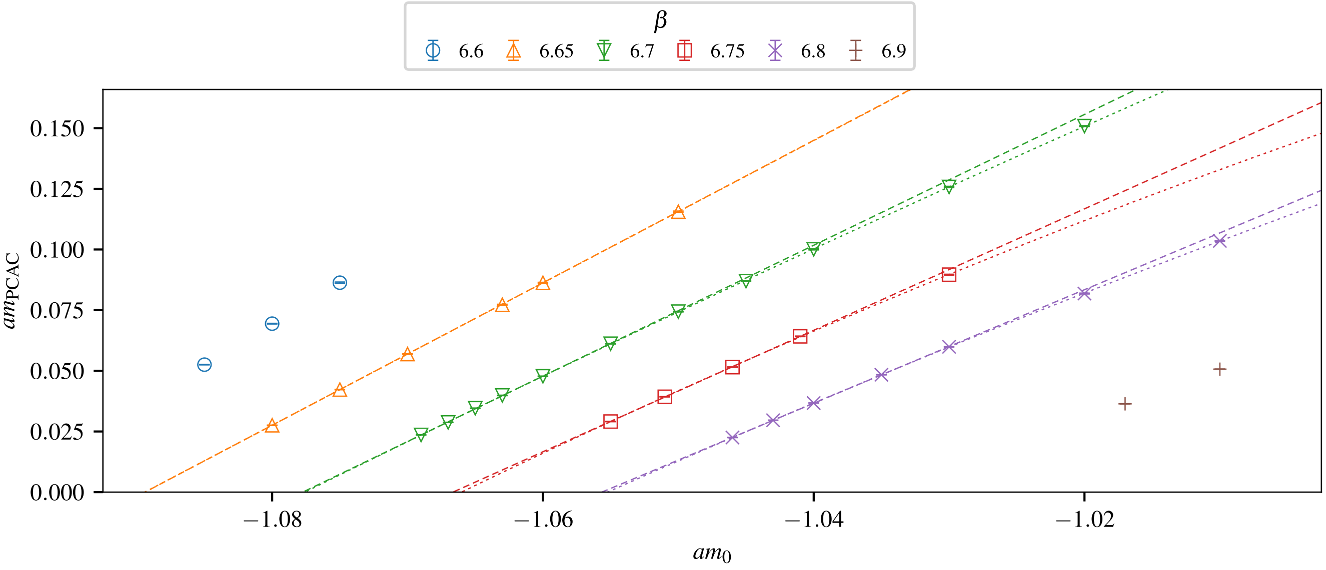

FIG. 19. The PCAC mass, $am_{\rm PCAC}$, as a function of the Wilson-Dirac mass, am_0, measured in all the ensembles used in this work, together with linear (dashed) and polynomial (dotted) fits obtained for fixed lattice coupling, β. The value of β is indicated by the color and marker, as shown in the legend.

ensembles used for the continuum extrapolations, while a quadratic term is required to extend the fits to all the ensembles, including the heavier ones. Because of the smallness of the uncertainties (which include only statistical errors), some of the values of the chi-square per degrees of freedom, $\chi^2/N_{\rm d.o.f}$, are larger than unity. Yet, for the qualitative purposes of this appendix, this is sufficient to provide support for the usage of $m_{\rm PCAC}$ as a replacement of bare hyperquark mass m_0 and for our choice of excluding the heavier ensembles from the continuum and massless extrapolations.

APPENDIX E: DEFT, SIMPLIFIED

We devote this appendix to examining an alternative approach, based upon dEFT [304–319], to the description of the long distance behavior of the theory. We restrict our attention to the mass and decay constant of the pseudoscalar mesons, ps, measured in lattice units, at fixed lattice couplings. We notice that the presence in the spectrum of a light scalar particle, the dilaton, is an essential feature of dEFT, which we cannot test with the available data and measurements. Nevertheless, the scaling relations built into dEFT can be tested without *a priori* knowledge of the properties (nor the existence) of such a particle, and it is hence legitimate to carry out this exercise. To this purpose, we borrow notation from Ref. [314], and write the scaling relation

$$m_{\rm ps}^2 f_{\rm ps}^{(2-y)} = C m_f, \tag{E1}$$

where the low-energy constant, C, is related to the fermion condensate, while y is associated with its scaling dimension [399]. We find it convenient to take the logarithm of this expression, and consider instead the expression

$$\log\left[\frac{am_{\rm ps}^2}{m_f}\right] = \tilde{C} + Y \log\left[a^2 f_{\rm ps}^2\right], \tag{E2}$$

where $Y = \frac{y}{2} - 1$, $\tilde{C} = \log C$, and we identify $m_f = m_{\rm PCAC}$.

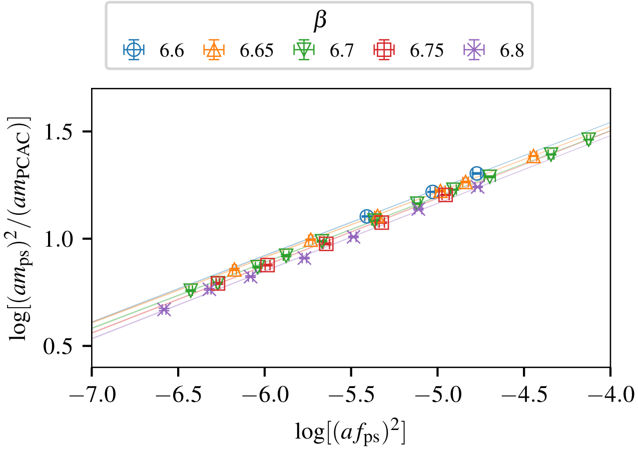

FIG. 20. Logarithmic plot of the scaling relation between fermion mass, $am_f = am_{\rm PCAC}$, pseudoscalar mass, $am_{\rm ps}$, and decay constant, $af_{\rm ps}$, for all the available values of the lattice coupling, β. The value of β is indicated by the color and marker, as shown in the legend. The solid lines are the results of dEFT fits.

In Fig. 20, we plot the left-hand side of Eq. (E2) as a function of $\log(a^2 f_{\rm ps}^2)$, for all the available values of the coupling, β. As shown in the figure, Eq. (E2) describes qualitatively well the results, over the whole mass range, while we find that the quality of the fits worsens as β increases. Surprisingly, the resulting values of the scaling dimension, y, are independent of the lattice coupling, $y \simeq 2.6$. This is lower than the naive, engineering dimension of the fermion condensate, $y_0 = 3$, but larger than the expectations for a theory in close proximity of edge of the conformal window, $y_* = 2$—see Ref. [203], the recent Ref. [400] and references therein.

We conclude by repeating that, even if the dEFT fit to the data yields intriguing results, it remains a somewhat speculative exercise. Besides the aforementioned fact that we do not know whether a light scalar singlet is present in the spectrum, this analysis relies on the use of continuum relations, while we know that the values of β available are such that significant corrections are expected to be for this analysis due to discretization effects. Another concern might originate from the observation that the quality of the dEFT fit worsens as the β value increases. Nevertheless, the results are encouraging, and it would be interesting to redo such analysis on lattice data that is closer to both the continuum and the massless limits.

[1] D. B. Kaplan and H. Georgi, $\mathrm{SU}(2) \times \mathrm{U}(1)$ breaking by vacuum misalignment, Phys. Lett. **136B**, 183 (1984).

[2] H. Georgi and D. B. Kaplan, Composite Higgs and custodial $SU(2)$, Phys. Lett. **145B**, 216 (1984).

[3] M. J. Dugan, H. Georgi, and D. B. Kaplan, Anatomy of a composite Higgs model, Nucl. Phys. **B254**, 299 (1985).

[4] G. Panico and A. Wulzer, The composite Nambu-Goldstone Higgs, Lect. Notes Phys. **913**, 1 (2016).

[5] O. Witzel, Review on composite Higgs models, Proc. Sci. LATTICE2018 (**2019**) 006 [arXiv:1901.08216].

[6] G. Cacciapaglia, C. Pica, and F. Sannino, Fundamental composite dynamics: A review, Phys. Rep. **877**, 1 (2020).

[7] G. Ferretti and D. Karateev, Fermionic UV completions of composite Higgs models, J. High Energy Phys. 03 (2014) 077.

[8] G. Ferretti, Gauge theories of partial compositeness: Scenarios for Run-II of the LHC, J. High Energy Phys. 06 (2016) 107.

[9] G. Cacciapaglia, G. Ferretti, T. Flacke, and H. Serôdio, Light scalars in composite Higgs models, Front. Phys. **7**, 22 (2019).

[10] E. Katz, A. E. Nelson, and D. G. E. Walker, The intermediate Higgs, J. High Energy Phys. 08 (2005) 074.

[11] R. Barbieri, B. Bellazzini, V. S. Rychkov, and A. Varagnolo, The Higgs boson from an extended symmetry, Phys. Rev. D **76**, 115008 (2007).

[12] P. Lodone, Vector-like quarks in a composite Higgs model, J. High Energy Phys. 12 (2008) 029.

[13] B. Gripaios, A. Pomarol, F. Riva, and J. Serra, Beyond the minimal composite Higgs model, J. High Energy Phys. 04 (2009) 070.

[14] J. Mrazek, A. Pomarol, R. Rattazzi, M. Redi, J. Serra, and A. Wulzer, The other natural two Higgs doublet model, Nucl. Phys. **B853**, 1 (2011).

[15] D. Marzocca, M. Serone, and J. Shu, General composite Higgs models, J. High Energy Phys. 08 (2012) 013.

[16] C. Grojean, O. Matsedonskyi, and G. Panico, Light top partners and precision physics, J. High Energy Phys. 10 (2013) 160.

[17] G. Cacciapaglia and F. Sannino, Fundamental composite (Goldstone) Higgs dynamics, J. High Energy Phys. 04 (2014) 111.

[18] G. Ferretti, UV completions of partial compositeness: The case for a SU(4) gauge group, J. High Energy Phys. 06 (2014) 142.

[19] A. Arbey, G. Cacciapaglia, H. Cai, A. Deandrea, S. Le Corre, and F. Sannino, Fundamental composite electroweak dynamics: Status at the LHC, Phys. Rev. D **95**, 015028 (2017).

[20] G. Cacciapaglia, H. Cai, A. Deandrea, T. Flacke, S. J. Lee, and A. Parolini, Composite scalars at the LHC: The Higgs, the Sextet and the Octet, J. High Energy Phys. 11 (2015) 201.

[21] F. Feruglio, B. Gavela, K. Kanshin, P. A. N. Machado, S. Rigolin, and S. Saa, The minimal linear σ model for the Goldstone Higgs, J. High Energy Phys. 06 (2016) 038.

[22] T. DeGrand, M. Golterman, E. T. Neil, and Y. Shamir, One-loop chiral perturbation theory with two fermion representations, Phys. Rev. D **94**, 025020 (2016).

[23] S. Fichet, G. von Gersdorff, E. Pontón, and R. Rosenfeld, The excitation of the global symmetry-breaking vacuum in composite Higgs models, J. High Energy Phys. 09 (2016) 158.

[24] J. Galloway, A. L. Kagan, and A. Martin, A UV complete partially composite-pNGB Higgs, Phys. Rev. D **95**, 035038 (2017).

[25] A. Agugliaro, O. Antipin, D. Becciolini, S. De Curtis, and M. Redi, UV complete composite Higgs models, Phys. Rev. D **95**, 035019 (2017).

[26] A. Belyaev, G. Cacciapaglia, H. Cai, G. Ferretti, T. Flacke, A. Parolini, and H. Serodio, Di-boson signatures as standard candles for partial compositeness, J. High Energy Phys. 01 (2017) 094.

[27] C. Csaki, T. Ma, and J. Shu, Maximally symmetric composite Higgs models, Phys. Rev. Lett. **119**, 131803 (2017).

[28] M. Chala, G. Durieux, C. Grojean, L. de Lima, and O. Matsedonskyi, Minimally extended SILH, J. High Energy Phys. 06 (2017) 088.

[29] M. Golterman and Y. Shamir, Effective potential in ultraviolet completions for composite Higgs models, Phys. Rev. D **97**, 095005 (2018).

[30] C. Csáki, T. Ma, and J. Shu, Trigonometric parity for composite Higgs models, Phys. Rev. Lett. **121**, 231801 (2018).

[31] T. Alanne, D. Buarque Franzosi, and M. T. Frandsen, A partially composite Goldstone Higgs, Phys. Rev. D **96**, 095012 (2017).

[32] T. Alanne, D. Buarque Franzosi, M. T. Frandsen, M. L. A. Kristensen, A. Meroni, and M. Rosenlyst, Partially composite Higgs models: Phenomenology and RG analysis, J. High Energy Phys. 01 (2018) 051.

[33] F. Sannino, P. Stangl, D. M. Straub, and A. E. Thomsen, Flavor physics and flavor anomalies in minimal fundamental partial compositeness, Phys. Rev. D **97**, 115046 (2018).

[34] T. Alanne, N. Bizot, G. Cacciapaglia, and F. Sannino, Classification of NLO operators for composite Higgs models, Phys. Rev. D **97**, 075028 (2018).

[35] N. Bizot, G. Cacciapaglia, and T. Flacke, Common exotic decays of top partners, J. High Energy Phys. 06 (2018) 065.

[36] C. Cai, G. Cacciapaglia, and H.-H. Zhang, Vacuum alignment in a composite 2HDM, J. High Energy Phys. 01 (2019) 130.

[37] A. Agugliaro, G. Cacciapaglia, A. Deandrea, and S. De Curtis, Vacuum misalignment and pattern of scalar masses in the SU(5)/SO(5) composite Higgs model, J. High Energy Phys. 02 (2019) 089.

[38] G. Cacciapaglia, T. Ma, S. Vatani, and Y. Wu, Towards a fundamental safe theory of composite Higgs and dark matter, Eur. Phys. J. C **80**, 1088 (2020).

[39] H. Gertov, A. E. Nelson, A. Perko, and D. G. E. Walker, Lattice-friendly gauge completion of a composite Higgs with top partners, J. High Energy Phys. 02 (2019) 181.

[40] V. Ayyar, M. F. Golterman, D. C. Hackett, W. Jay, E. T. Neil, Y. Shamir *et al.*, Radiative contribution to the composite-Higgs potential in a two-representation lattice model, Phys. Rev. D **99**, 094504 (2019).

[41] G. Cacciapaglia, H. Cai, A. Deandrea, and A. Kushwaha, Composite Higgs and dark matter model in SU(6)/SO(6), J. High Energy Phys. 10 (2019) 035.

[42] D. Buarque Franzosi and G. Ferretti, Anomalous dimensions of potential top-partners, SciPost Phys. **7**, 027 (2019).

[43] G. Cacciapaglia, S. Vatani, and C. Zhang, Composite Higgs meets Planck scale: Partial compositeness from partial unification, Phys. Lett. B **815**, 136177 (2021).

[44] G. Cacciapaglia, A. Deandrea, T. Flacke, and A. M. Iyer, Gluon-photon signatures for color octet at the LHC (and beyond), J. High Energy Phys. 05 (2020) 027.

[45] Z.-Y. Dong, C.-S. Guan, T. Ma, J. Shu, and X. Xue, UV completed composite Higgs model with heavy composite partners, Phys. Rev. D **104**, 035013 (2021).

[46] G. Cacciapaglia, T. Flacke, M. Kunkel, and W. Porod, Phenomenology of unusual top partners in composite Higgs models, J. High Energy Phys. 02 (2022) 208.

[47] A. Banerjee, D. B. Franzosi, and G. Ferretti, Modelling vector-like quarks in partial compositeness framework, J. High Energy Phys. 03 (2022) 200.

[48] G. Ferretti, Compositeness above the electroweak scale and a proposed test at LHCb, EPJ Web Conf. **258**, 08002 (2022).

[49] H. Cai and G. Cacciapaglia, Partial compositeness under precision scrutiny, J. High Energy Phys. 12 (2022) 104.

[50] G. Cacciapaglia, A. Deandrea, M. Kunkel, and W. Porod, Coloured spin-1 states in composite Higgs models, J. High Energy Phys. 06 (2024) 092.

[51] A. Banerjee, E. Bergeaas Kuutmann, V. Ellajosyula, R. Enberg, G. Ferretti, and L. Panizzi, Vector-like quarks: Status and new directions at the LHC, SciPost Phys. Core **7**, 079 (2024).

[52] R. Contino, Y. Nomura, and A. Pomarol, Higgs as a holographic pseudoGoldstone boson, Nucl. Phys. **B671**, 148 (2003).

[53] K. Agashe, R. Contino, and A. Pomarol, The minimal composite Higgs model, Nucl. Phys. **B719**, 165 (2005).

[54] K. Agashe and R. Contino, The minimal composite Higgs model and electroweak precision tests, Nucl. Phys. **B742**, 59 (2006).

[55] K. Agashe, R. Contino, L. Da Rold, and A. Pomarol, A custodial symmetry for $Zb\bar{b}$, Phys. Lett. B **641**, 62 (2006).

[56] R. Contino, L. Da Rold, and A. Pomarol, Light custodians in natural composite Higgs models, Phys. Rev. D **75**, 055014 (2007).

[57] A. Falkowski and M. Perez-Victoria, Electroweak breaking on a soft wall, J. High Energy Phys. 12 (2008) 107.

[58] R. Contino, The Higgs as a composite Nambu-Goldstone boson, arXiv:1005.4269.

[59] R. Contino, D. Marzocca, D. Pappadopulo, and R. Rattazzi, On the effect of resonances in composite Higgs phenomenology, J. High Energy Phys. 10 (2011) 081.

[60] J. Erdmenger, N. Evans, W. Porod, and K. S. Rigatos, Gauge/gravity dynamics for composite Higgs models and the top mass, Phys. Rev. Lett. **126**, 071602 (2021).

[61] J. Erdmenger, N. Evans, W. Porod, and K. S. Rigatos, Gauge/gravity dual dynamics for the strongly coupled sector of composite Higgs models, J. High Energy Phys. 02 (2021) 058.

[62] D. Elander and M. Piai, Towards top-down holographic composite Higgs: Minimal coset from maximal supergravity, J. High Energy Phys. 03 (2022) 049.

[63] D. Elander, A. Fatemiabhari, and M. Piai, Toward minimal composite Higgs models from regular geometries in bottom-up holography, Phys. Rev. D **107**, 115021 (2023).

[64] J. Erdmenger, N. Evans, Y. Liu, and W. Porod, Holographic non-Abelian flavour symmetry breaking, Universe **9**, 289 (2023).

[65] D. Elander, A. Fatemiabhari, and M. Piai, On holographic vacuum misalignment, Phys. Rev. D **111**, 015040 (2025).

[66] D. B. Kaplan, Flavor at SSC energies: A new mechanism for dynamically generated fermion masses, Nucl. Phys. **B365**, 259 (1991).

[67] Y. Grossman and M. Neubert, Neutrino masses and mixings in nonfactorizable geometry, Phys. Lett. B **474**, 361 (2000).

[68] T. Gherghetta and A. Pomarol, Bulk fields and supersymmetry in a slice of AdS, Nucl. Phys. **B586**, 141 (2000).

[69] Z. Chacko and R. K. Mishra, Effective theory of a light dilaton, Phys. Rev. D **87**, 115006 (2013).

[70] M. J. Strassler and K. M. Zurek, Echoes of a hidden valley at hadron colliders, Phys. Lett. B **651**, 374 (2007).

[71] K. Cheung and T.-C. Yuan, Hidden fermion as milli-charged dark matter in Stueckelberg $Z\prime$ model, J. High Energy Phys. 03 (2007) 120.

[72] T. Hambye, Hidden vector dark matter, J. High Energy Phys. 01 (2009) 028.

[73] J. L. Feng, M. Kaplinghat, H. Tu, and H.-B. Yu, Hidden charged dark matter, J. Cosmol. Astropart. Phys. 07 (2009) 004.

[74] T. Cohen, D. J. Phalen, A. Pierce, and K. M. Zurek, Asymmetric dark matter from a GeV hidden sector, Phys. Rev. D **82**, 056001 (2010).

[75] R. Foot and S. Vagnozzi, Dissipative hidden sector dark matter, Phys. Rev. D **91**, 023512 (2015).

[76] G. Bertone and D. Hooper, History of dark matter, Rev. Mod. Phys. **90**, 045002 (2018).

[77] E. Del Nobile, C. Kouvaris, and F. Sannino, Interfering composite asymmetric dark matter for DAMA and CoGeNT, Phys. Rev. D **84**, 027301 (2011).

[78] A. Hietanen, R. Lewis, C. Pica, and F. Sannino, Composite Goldstone dark matter: Experimental predictions from the lattice, J. High Energy Phys. 12 (2014) 130.

[79] J. M. Cline, W. Huang, and G. D. Moore, Challenges for models with composite states, Phys. Rev. D **94**, 055029 (2016).

[80] N. A. Dondi, F. Sannino, and J. Smirnov, Thermal history of composite dark matter, Phys. Rev. D **101**, 103010 (2020).

[81] S. Ge, K. Lawson, and A. Zhitnitsky, Axion quark nugget dark matter model: Size distribution and survival pattern, Phys. Rev. D **99**, 116017 (2019).

[82] V. Beylin, M. Y. Khlopov, V. Kuksa, and N. Volchanskiy, Hadronic and hadron-like physics of dark matter, Symmetry **11**, 587 (2019).

[83] N. Yamanaka, H. Iida, A. Nakamura, and M. Wakayama, Dark matter scattering cross section and dynamics in dark Yang-Mills theory, Phys. Lett. B **813**, 136056 (2021).

[84] N. Yamanaka, H. Iida, A. Nakamura, and M. Wakayama, Glueball scattering cross section in lattice $SU(2)$ Yang-Mills theory, Phys. Rev. D **102**, 054507 (2020).

[85] H. Cai and G. Cacciapaglia, Singlet dark matter in the SU(6)/SO(6) composite Higgs model, Phys. Rev. D **103**, 055002 (2021).

[86] J. Pomper and S. Kulkarni, Low energy effective theories of composite dark matter with real representations, arXiv:2402.04176.

[87] T. Appelquist, J. Ingoldby, and M. Piai, Dilaton forbidden dark matter, Phys. Rev. D **110**, 035013 (2024).

[88] Y. Hochberg, E. Kuflik, T. Volansky, and J. G. Wacker, Mechanism for thermal relic dark matter of strongly interacting massive particles, Phys. Rev. Lett. **113**, 171301 (2014).

[89] Y. Hochberg, E. Kuflik, H. Murayama, T. Volansky, and J. G. Wacker, Model for thermal relic dark matter of strongly interacting massive particles, Phys. Rev. Lett. **115**, 021301 (2015).

[90] Y. Hochberg, E. Kuflik, and H. Murayama, SIMP spectroscopy, J. High Energy Phys. 05 (2016) 090.

[91] N. Bernal, X. Chu, and J. Pradler, Simply split strongly interacting massive particles, Phys. Rev. D **95**, 115023 (2017).

[92] A. Berlin, N. Blinov, S. Gori, P. Schuster, and N. Toro, Cosmology and accelerator tests of strongly interacting dark matter, Phys. Rev. D **97**, 055033 (2018).

[93] N. Bernal, X. Chu, S. Kulkarni, and J. Pradler, Self-interacting dark matter without prejudice, Phys. Rev. D **101**, 055044 (2020).

[94] Y.-D. Tsai, R. McGehee, and H. Murayama, Resonant self-interacting dark matter from dark QCD, Phys. Rev. Lett. **128**, 172001 (2022).

[95] D. Kondo, R. McGehee, T. Melia, and H. Murayama, Linear sigma dark matter, J. High Energy Phys. 09 (2022) 041.

[96] N. Bernal and X. Chu, $\mathbb{Z}_2$ SIMP dark matter, J. Cosmol. Astropart. Phys. 01 (2016) 006.

[97] X. Chu, M. Nikolic, and J. Pradler, Even SIMP miracles are possible, Phys. Rev. Lett. **133**, 021003 (2024).

[98] M. Cirelli, A. Strumia, and J. Zupan, Dark matter, arXiv:2406.01705.

[99] N. Arkani-Hamed, H.-C. Cheng, P. Creminelli, and L. Randall, Pseudonatural inflation, J. Cosmol. Astropart. Phys. 07 (2003) 003.

[100] G. Cacciapaglia, D. Y. Cheong, A. Deandrea, W. Isnard, and S. C. Park, Composite hybrid inflation: Dilaton and waterfall pions, J. Cosmol. Astropart. Phys. 10 (2023) 063.

[101] J. Liu, H.-X. Zhang, S. Matsuzaki, and H. Ishida, Walking-dilaton hybrid inflation with $B-L$ Higgs embedded in dynamical scalegenesis, J. High Energy Phys. 10 (2024) 069.

[102] E. Witten, Cosmic separation of phases, Phys. Rev. D **30**, 272 (1984).

[103] M. Kamionkowski, A. Kosowsky, and M. S. Turner, Gravitational radiation from first order phase transitions, Phys. Rev. D **49**, 2837 (1994).

[104] B. Allen, The Stochastic gravity wave background: Sources and detection, in Les Houches School of Physics: Astrophysical Sources of Gravitational Radiation (1996), pp. 373–417, arXiv:gr-qc/9604033.

[105] P. Schwaller, Gravitational waves from a dark phase transition, Phys. Rev. Lett. **115**, 181101 (2015).

[106] D. Croon, V. Sanz, and G. White, Model discrimination in gravitational wave spectra from dark phase transitions, J. High Energy Phys. 08 (2018) 203.

[107] N. Christensen, Stochastic gravitational wave backgrounds, Rep. Prog. Phys. **82**, 016903 (2019).

[108] N. Seto, S. Kawamura, and T. Nakamura, Possibility of direct measurement of the acceleration of the universe using 0.1-Hz band laser interferometer gravitational wave antenna in space, Phys. Rev. Lett. **87**, 221103 (2001).

[109] S. Kawamura *et al.*, The Japanese space gravitational wave antenna DECIGO, Classical Quantum Gravity **23**, S125 (2006).

[110] J. Crowder and N. J. Cornish, Beyond LISA: Exploring future gravitational wave missions, Phys. Rev. D **72**, 083005 (2005).

[111] V. Corbin and N. J. Cornish, Detecting the cosmic gravitational wave background with the big bang observer, Classical Quantum Gravity **23**, 2435 (2006).

[112] G. M. Harry, P. Fritschel, D. A. Shaddock, W. Folkner, and E. S. Phinney, Laser interferometry for the big bang observer, Classical Quantum Gravity **23**, 4887 (2006).

[113] S. Hild *et al.*, Sensitivity studies for third-generation gravitational wave observatories, Classical Quantum Gravity **28**, 094013 (2011).

[114] K. Yagi and N. Seto, Detector configuration of DECIGO/BBO and identification of cosmological neutron-star binaries, Phys. Rev. D **83**, 044011 (2011).

[115] B. Sathyaprakash *et al.*, Scientific objectives of Einstein telescope, Classical Quantum Gravity **29**, 124013 (2012).

[116] E. Thrane and J. D. Romano, Sensitivity curves for searches for gravitational-wave backgrounds, Phys. Rev. D **88**, 124032 (2013).

[117] C. Caprini *et al.*, Science with the space-based interferometer eLISA. II: Gravitational waves from cosmological phase transitions, J. Cosmol. Astropart. Phys. 04 (2016) 001.

[118] LISA Collaboration, Laser interferometer space antenna, arXiv:1702.00786.

[119] LIGO Scientific Collaboration, Exploring the sensitivity of next generation gravitational wave detectors, Classical Quantum Gravity **34**, 044001 (2017).

[120] S. Isoyama, H. Nakano, and T. Nakamura, Multiband gravitational-wave astronomy: Observing binary inspirals with a decihertz detector, B-DECIGO, Prog. Theor. Exp. Phys. **2018**, 073E01 (2018).

[121] J. Baker *et al.*, The laser interferometer space antenna: Unveiling the millihertz gravitational wave sky, arXiv:1907.06482.

[122] V. Brdar, A. J. Helmboldt, and J. Kubo, Gravitational waves from first-order phase transitions: LIGO as a window to unexplored seesaw scales, J. Cosmol. Astropart. Phys. 02 (2019) 021.

[123] D. Reitze *et al.*, Cosmic explorer: The U.S. contribution to gravitational-wave astronomy beyond LIGO, Bull. Am. Astron. Soc. **51**, 035 (2019).

[124] C. Caprini *et al.*, Detecting gravitational waves from cosmological phase transitions with LISA: An update, J. Cosmol. Astropart. Phys. 03 (2020) 024.

[125] M. Maggiore *et al.*, Science case for the Einstein telescope, J. Cosmol. Astropart. Phys. 03 (2020) 050.

[126] W.-C. Huang, M. Reichert, F. Sannino, and Z.-W. Wang, Testing the dark SU(N) Yang-Mills theory confined landscape: From the lattice to gravitational waves, Phys. Rev. D **104**, 035005 (2021).

[127] J. Halverson, C. Long, A. Maiti, B. Nelson, and G. Salinas, Gravitational waves from dark Yang-Mills sectors, J. High Energy Phys. 05 (2021) 154.

[128] Z. Kang, J. Zhu, and S. Matsuzaki, Dark confinement-deconfinement phase transition: A roadmap from Polyakov loop models to gravitational waves, J. High Energy Phys. 09 (2021) 060.

[129] M. Reichert, F. Sannino, Z.-W. Wang, and C. Zhang, Dark confinement and chiral phase transitions: Gravitational waves vs matter representations, J. High Energy Phys. 01 (2022) 003.

[130] M. Reichert and Z.-W. Wang, Gravitational waves from dark composite dynamics, EPJ Web Conf. **274**, 08003 (2022).

[131] R. Pasechnik, M. Reichert, F. Sannino, and Z.-W. Wang, Gravitational waves from composite dark sectors, J. High Energy Phys. 02 (2024) 159.

[132] A. Banerjee, M. Merchand, and I. Nałęcz, Phase transition and gravitational waves in maximally symmetric composite Higgs model, J. High Energy Phys. 10 (2024) 106.

[133] M. Bruno, N. Forzano, M. Panero, and A. Smecca, Thermal evolution of dark matter in the early universe from a symplectic glueball model, arXiv:2410.17122.

[134] D. Mason, B. Lucini, M. Piai, E. Rinaldi, and D. Vadacchino, The density of states method in Yang-Mills theories and first order phase transitions, EPJ Web Conf. **274**, 08007 (2022).

[135] D. Mason, B. Lucini, M. Piai, E. Rinaldi, and D. Vadacchino, The density of state method for first-order phase transitions in Yang-Mills theories, Proc. Sci. LATTICE2022 (**2023**) 216 [arXiv:2212.01074].

[136] F. Springer and D. Schaich, Density of states for gravitational waves, Proc. Sci. LATTICE2021 (**2022**) 043 [arXiv:2112.11868].

[137] F. Springer and D. Schaich, Progress applying density of states for gravitational waves, EPJ Web Conf. **274**, 08008 (2022).

[138] Lattice Strong Dynamics (LSD) Collaboration, Advances in using density of states for large-N Yang–Mills, Proc. Sci. LATTICE2022 (**2023**) 223 [arXiv:2303.01149].

[139] B. Lucini, D. Mason, M. Piai, E. Rinaldi, and D. Vadacchino, First-order phase transitions in Yang-Mills theories and the density of state method, Phys. Rev. D **108**, 074517 (2023).

[140] D. Mason, B. Lucini, M. Piai, E. Rinaldi, and D. Vadacchino, The deconfinement phase transition in $Sp(2N)$ gauge theories and the density of states method, Proc. Sci. LATTICE2023 (**2024**) 085 [arXiv:2310.02145].

[141] Lattice Strong Dynamics (LSD) Collaboration, First-order bulk transitions in large-N lattice Yang–Mills theories using the density of states, arXiv:2311.10243.

[142] Bennett, B. Lucini, D. Mason, M. Piai, E. Rinaldi, and D. Vadacchino, The density of states method for symplectic gauge theories at finite temperature, arXiv:2409.19426.

[143] E. Bennett, D. K. Hong, J.-W. Lee, C. J. D. Lin, B. Lucini, M. Piai, and D. Vadacchino, Sp(4) gauge theory on the lattice: Towards SU(4)/Sp(4) composite Higgs (and beyond), J. High Energy Phys. 03 (2018) 185.

[144] E. Bennett, D. K. Hong, J.-W. Lee, C. J. D. Lin, B. Lucini, M. Piai, and D. Vadacchino, Sp(4) gauge theories on the lattice: $N_f = 2$ dynamical fundamental fermions, J. High Energy Phys. 12 (2019) 053.

[145] E. Bennett, D. K. Hong, J.-W. Lee, C.-J. D. Lin, B. Lucini, M. Mesiti, M. Piai, J. Rantaharju, and D. Vadacchino, $Sp(4)$ gauge theories on the lattice: Quenched fundamental and antisymmetric fermions, Phys. Rev. D **101**, 074516 (2020).

[146] E. Bennett, J. Holligan, D. K. Hong, J.-W. Lee, C. J. D. Lin, B. Lucini *et al.*, Color dependence of tensor and scalar glueball masses in Yang-Mills theories, Phys. Rev. D **102**, 011501 (2020).

[147] E. Bennett, J. Holligan, D. K. Hong, J.-W. Lee, C. J. D. Lin, B. Lucini *et al.*, Glueballs and strings in $Sp(2N)$ Yang-Mills theories, Phys. Rev. D **103**, 054509 (2021).

[148] E. Bennett, D. K. Hong, H. Hsiao, J.-W. Lee, C. J. D. Lin, B. Lucini *et al.*, Lattice studies of the Sp(4) gauge theory with two fundamental and three antisymmetric Dirac fermions, Phys. Rev. D **106**, 014501 (2022).

[149] E. Bennett, D. K. Hong, J.-W. Lee, C. J. D. Lin, B. Lucini, M. Piai, and D. Vadacchino, Color dependence of the topological susceptibility in Yang-Mills theories, Phys. Lett. B **835**, 137504 (2022).

[150] E. Bennett, D. K. Hong, J.-W. Lee, C. J. D. Lin, B. Lucini, M. Piai *et al.*, Sp($2N$) Yang-Mills theories on the lattice: Scale setting and topology, Phys. Rev. D **106**, 094503 (2022).

[151] E. Bennett, J. Holligan, D. K. Hong, H. Hsiao, J.-W. Lee, C. J. D. Lin, B. Lucini, M. Mesiti, M. Piai, and D. Vadacchino *et al.*, Sp($2N$) lattice gauge theories and extensions of the standard model of particle physics, Universe **9**, 236 (2023).

[152] E. Bennett *et al.*, Symplectic lattice gauge theories in the grid framework: Approaching the conformal window, Phys. Rev. D **108**, 094508 (2023).

[153] E. Bennett, D. K. Hong, H. Hsiao, J.-W. Lee, C. J. D. Lin, B. Lucini *et al.*, Lattice investigations of the chimera baryon spectrum in the $Sp(4)$ gauge theory, Phys. Rev. D **109**, 094512 (2024).

[154] E. Bennett, J. Holligan, D. K. Hong, J.-W. Lee, C. J. D. Lin, B. Lucini *et al.*, Spectrum of mesons in quenched $Sp(2N)$ gauge theories, Phys. Rev. D **109**, 094517 (2024).

[155] E. Bennett *et al.*, Meson spectroscopy from spectral densities in lattice gauge theories, Phys. Rev. D **110**, 074509 (2024).

[156] E. Bennett, N. Forzano, D. K. Hong, H. Hsiao, J.-W. Lee, C. J. D. Lin, B. Lucini, M. Piai, D. Vadacchino, and F. Zierler, Mixing between flavor singlets in lattice gauge theories coupled to matter fields in multiple representations, Phys. Rev. D **110**, 074504 (2024).

[157] J.-W. Lee, E. Bennett, D. K. Hong, C. J. D. Lin, B. Lucini, M. Piai *et al.*, Progress in the lattice simulations of $Sp(2N)$ gauge theories, Proc. Sci. LATTICE2018 (**2018**) 192 [arXiv:1811.00276].

[158] B. Lucini, E. Bennett, J. Holligan, D. K. Hong, H. Hsiao, J.-W. Lee *et al.*, Sp(4) gauge theories and beyond the standard model physics, EPJ Web Conf. **258**, 08003 (2022).

[159] E. Bennett, J. Holligan, D. K. Hong, H. Hsiao, J.-W. Lee, C. J. D. Lin *et al.*, Progress in $Sp(2N)$ lattice gauge theories, Proc. Sci. LATTICE2021 (**2022**) 308 [arXiv:2111.14544].

[160] J.-W. Lee, E. Bennett, D. K. Hong, H. Hsiao, C. J. D. Lin, B. Lucini *et al.*, Spectroscopy of $Sp(4)$ lattice gauge theory with $n_f = 3$ antisymmetric fermions, Proc. Sci. LATTICE2022 (**2023**) 214 [arXiv:2210.08154].

[161] H. Hsiao, E. Bennett, D. K. Hong, J.-W. Lee, C. J. D. Lin, B. Lucini *et al.*, Spectroscopy of chimera baryons in a $Sp(4)$ lattice gauge theory, Proc. Sci. LATTICE2022 (**2022**) 211 [arXiv:2211.03955].

[162] E. Bennett *et al.*, Progress on the spectroscopy of lattice gauge theories using spectral densities, Proc. Sci. LATTICE2024 (**2025**) 137 [arXiv:2410.11386].

[163] F. Zierler, E. Bennett, N. Forzano, D. K. Hong, H. Hsiao, J.-W. Lee *et al.*, Progress on pseudoscalar flavour-singlets in Sp(4) with mixed fermion representations, Proc. Sci. LATTICE2024 (**2025**) 138 [arXiv:2410.11412].

[164] H. Hsiao, E. Bennett, N. Forzano, D. K. Hong, J.-W. Lee, C. J. D. Lin *et al.*, Progress on the spectroscopy of an Sp(4) gauge theory coupled to matter in multiple representations, Proc. Sci. LATTICE2024 (**2025**) 139 [arXiv:2411.18379].

[165] A. Maas and F. Zierler, Strong isospin breaking in $\boldsymbol{Sp}(4)$ gauge theory, Proc. Sci. LATTICE2021 (**2022**) 130 [arXiv:2109.14377].

[166] F. Zierler and A. Maas, $Sp(4)$ SIMP dark matter on the lattice, Proc. Sci. LHCP2021 (**2021**) 162.

[167] S. Kulkarni, A. Maas, S. Mee, M. Nikolic, J. Pradler, and F. Zierler, Low-energy effective description of dark $Sp(4)$ theories, SciPost Phys. **14**, 044 (2023).

[168] F. Zierler, J.-W. Lee, A. Maas, and F. Pressler, Singlet mesons in dark $Sp(4)$ theories, Proc. Sci. LATTICE2022 (**2023**) 225 [arXiv:2210.11187].

[169] F. Zierler, S. Kulkarni, A. Maas, S. Mee, M. Nikolic, and J. Pradler, Strongly interacting dark matter from Sp(4) gauge theory, EPJ Web Conf. **274**, 08014 (2022).

[170] E. Bennett, H. Hsiao, J.-W. Lee, B. Lucini, A. Maas, M. Piai, and F. Zierler, Singlets in gauge theories with fundamental matter, Phys. Rev. D **109**, 034504 (2024).

[171] Y. Dengler, A. Maas, and F. Zierler, Scattering of dark pions in an Sp(4)-gauge theory, Proc. Sci. LATTICE2023 (**2024**) 103 [arXiv:2311.18549].

[172] Y. Dengler, A. Maas, and F. Zierler, Scattering of dark pions in Sp(4) gauge theory, Phys. Rev. D **110**, 054513 (2024).

[173] K. Holland, M. Pepe, and U. J. Wiese, The deconfinement phase transition of Sp(2) and Sp(3) Yang-Mills theories in $(2+1)$-dimensions and $(3+1)$-dimensions, Nucl. Phys. **B694**, 35 (2004).

[174] M. Bochicchio, An asymptotic solution of large-N QCD, for the glueball and meson spectrum and the collinear S-matrix, AIP Conf. Proc. **1735**, 030004 (2016).

[175] M. Bochicchio, Glueball and meson spectrum in large-N massless QCD, arXiv:1308.2925.

[176] D. K. Hong, J.-W. Lee, B. Lucini, M. Piai, and D. Vadacchino, Casimir scaling and Yang–Mills glueballs, Phys. Lett. B **775**, 89 (2017).

[177] D. Elander, M. Frigerio, M. Knecht, and J.-L. Kneur, Holographic models of composite Higgs in the Veneziano limit. Part I. Bosonic sector, J. High Energy Phys. 03 (2021) 182.

[178] D. Elander, M. Frigerio, M. Knecht, and J.-L. Kneur, Holographic models of composite Higgs in the Veneziano limit. Part II. Fermionic sector, J. High Energy Phys. 05 (2022) 066.

[179] J. Erdmenger, N. Evans, Y. Liu, and W. Porod, Holography for Sp($2N_c$) gauge dynamics: From composite Higgs to technicolour, J. High Energy Phys. 07 (2024) 169.

[180] T. Imoto, T. Sakai, and S. Sugimoto, $O(N_c)$ and USp(N_c) QCD from string theory, Prog. Theor. Phys. **122**, 1433 (2010).

[181] M. E. Peskin, The alignment of the vacuum in theories of technicolor, Nucl. Phys. **B175**, 197 (1980).

[182] J. Barnard, T. Gherghetta, and T. S. Ray, UV descriptions of composite Higgs models without elementary scalars, J. High Energy Phys. 02 (2014) 002.

[183] A. Hietanen, R. Lewis, C. Pica, and F. Sannino, Fundamental composite Higgs dynamics on the lattice: $SU(2)$ with two flavors, J. High Energy Phys. 07 (2014) 116.

[184] W. Detmold, M. McCullough, and A. Pochinsky, Dark nuclei. II. Nuclear spectroscopy in two-color QCD, Phys. Rev. D **90**, 114506 (2014).

[185] R. Arthur, V. Drach, M. Hansen, A. Hietanen, C. Pica, and F. Sannino, $SU(2)$ gauge theory with two fundamental flavors: A minimal template for model building, Phys. Rev. D **94**, 094507 (2016).

[186] R. Arthur, V. Drach, A. Hietanen, C. Pica, and F. Sannino, $SU(2)$ gauge theory with two fundamental flavours: Scalar and pseudoscalar spectrum, arXiv:1607.06654.

[187] C. Pica, V. Drach, M. Hansen, and F. Sannino, Composite Higgs dynamics on the lattice, EPJ Web Conf. **137**, 10005 (2017).

[188] J.-W. Lee, B. Lucini, and M. Piai, Symmetry restoration at high-temperature in two-color and two-flavor lattice gauge theories, J. High Energy Phys. 04 (2017) 036.

[189] V. Drach, T. Janowski, and C. Pica, Update on $SU(2)$ gauge theory with $N_F = 2$ fundamental flavours, EPJ Web Conf. **175**, 08020 (2018).

[190] V. Drach, T. Janowski, C. Pica, and S. Prelovsek, Scattering of Goldstone Bosons and resonance production in a Composite Higgs model on the lattice, J. High Energy Phys. 04 (2021) 117.

[191] V. Drach, P. Fritzsch, A. Rago, and F. Romero-López, Singlet channel scattering in a composite Higgs model on the lattice, Eur. Phys. J. C **82**, 47 (2022).

[192] L. S. Bowes, V. Drach, P. Fritzsch, A. Rago, and F. Romero-Lopez, 2-flavour $SU(2)$ gauge theory with exponential clover Wilson fermions, Proc. Sci. LATTICE2023 (**2024**) 094 [arXiv:2401.00589].

[193] V. Ayyar, T. DeGrand, M. Golterman, D. C. Hackett, W. I. Jay, E. T. Neil, Y. Shamir, and B. Svetitsky, Spectroscopy of SU(4) composite Higgs theory with two distinct fermion representations, Phys. Rev. D **97**, 074505 (2018).

[194] V. Ayyar, T. Degrand, D. C. Hackett, W. I. Jay, E. T. Neil, Y. Shamir, and B. Svetitsky, Baryon spectrum of $SU(4)$ composite Higgs theory with two distinct fermion representations, Phys. Rev. D **97**, 114505 (2018).

[195] V. Ayyar, T. DeGrand, D. C. Hackett, W. I. Jay, E. T. Neil, Y. Shamir, and B. Svetitsky, Finite-temperature phase structure of $SU(4)$ gauge theory with multiple fermion representations, Phys. Rev. D **97**, 114502 (2018).

[196] V. Ayyar, T. DeGrand, D. C. Hackett, W. I. Jay, E. T. Neil, Y. Shamir *et al.*, Partial compositeness and baryon matrix elements on the lattice, Phys. Rev. D **99**, 094502 (2019).

[197] G. Cossu, L. Del Debbio, M. Panero, and D. Preti, Strong dynamics with matter in multiple representations: $SU(4)$ gauge theory with fundamental and sextet fermions, Eur. Phys. J. C **79**, 638 (2019).

[198] A. Lupo, M. Panero, N. Tantalo, and L. Del Debbio, Spectral reconstruction in $SU(4)$ gauge theory with fermions in multiple representations, Proc. Sci. LATTICE2021 (**2022**) 092 [arXiv:2112.01158].

[199] A. Hasenfratz, E. T. Neil, Y. Shamir, B. Svetitsky, and O. Witzel, Infrared fixed point and anomalous dimensions in a composite Higgs model, Phys. Rev. D **107**, 114504 (2023).

[200] G. Bergner and S. Piemonte, Lattice simulations of a gauge theory with mixed adjoint-fundamental matter, Phys. Rev. D **103**, 014503 (2021).

[201] G. Bergner and S. Piemonte, Mixed adjoint-fundamental matter and applications towards SQCD and beyond, Proc. Sci. LATTICE2021 (**2022**) 242 [arXiv:2111.15335].

[202] T. Appelquist, K. D. Lane, and U. Mahanta, On the ladder approximation for spontaneous chiral symmetry breaking, Phys. Rev. Lett. **61**, 1553 (1988).

[203] A. G. Cohen and H. Georgi, Walking beyond the rainbow, Nucl. Phys. **B314**, 7 (1989).

[204] F. Sannino and K. Tuominen, Orientifold theory dynamics and symmetry breaking, Phys. Rev. D **71**, 051901 (2005).

[205] D. D. Dietrich and F. Sannino, Conformal window of $SU(N)$ gauge theories with fermions in higher dimensional representations, Phys. Rev. D **75**, 085018 (2007).

[206] T. A. Ryttov and F. Sannino, Supersymmetry inspired QCD beta function, Phys. Rev. D **78**, 065001 (2008).

[207] C. Pica and F. Sannino, Beta function and anomalous dimensions, Phys. Rev. D **83**, 116001 (2011).

[208] C. Pica and F. Sannino, UV and IR zeros of gauge theories at the four loop order and beyond, Phys. Rev. D **83**, 035013 (2011).

[209] B. S. Kim, D. K. Hong, and J.-W. Lee, Into the conformal window: Multirepresentation gauge theories, Phys. Rev. D **101**, 056008 (2020).

[210] J.-W. Lee, Conformal window from conformal expansion, Phys. Rev. D **103**, 076006 (2021).

[211] T. A. Ryttov and R. Shrock, Infrared zero of β and value of γ_m for an $SU(3)$ gauge theory at the five-loop level, Phys. Rev. D **94**, 105015 (2016).

[212] T. A. Ryttov, Consistent perturbative fixed point calculations in QCD and supersymmetric QCD, Phys. Rev. Lett. **117**, 071601 (2016).

[213] T. A. Ryttov and R. Shrock, Scheme-independent calculation of $\gamma_{\bar{\psi}\psi,IR}$ for an $SU(3)$ gauge theory, Phys. Rev. D **94**, 105014 (2016).

[214] T. A. Ryttov and R. Shrock, Scheme-independent series expansions at an infrared zero of the beta function in asymptotically free gauge theories, Phys. Rev. D **94**, 125005 (2016).

[215] T. A. Ryttov and R. Shrock, Higher-order scheme-independent calculations of physical quantities in the conformal phase of a gauge theory, Phys. Rev. D **95**, 085012 (2017).

[216] T. A. Ryttov and R. Shrock, Higher-order scheme-independent series expansions of $\gamma_{\bar{\psi}\psi,IR}$ and β'_{IR} in conformal field theories, Phys. Rev. D **95**, 105004 (2017).

[217] T. A. Ryttov and R. Shrock, Infrared fixed point physics in $\mathrm{SO}(N_c)$ and $\mathrm{Sp}(N_c)$ gauge theories, Phys. Rev. D **96**, 105015 (2017).

[218] J. A. Gracey, T. A. Ryttov, and R. Shrock, Scheme-independent calculations of anomalous dimensions of baryon operators in conformal field theories, Phys. Rev. D **97**, 116018 (2018).

[219] T. A. Ryttov and R. Shrock, Scheme-independent calculations of properties at a conformal infrared fixed point in gauge theories with multiple fermion representations, Phys. Rev. D **98**, 096003 (2018).

[220] T. A. Ryttov and R. Shrock, Scheme-independent series for anomalous dimensions of higher-spin operators at an infrared fixed point in a gauge theory, Phys. Rev. D **101**, 076018 (2020).

[221] T. A. Ryttov and R. Shrock, Anomalous dimensions at an infrared fixed point in an SU(N_c) gauge theory with fermions in the fundamental and antisymmetric tensor representations, Phys. Rev. D **108**, 056007 (2023).

[222] W. E. Caswell, Asymptotic behavior of nonAbelian gauge theories to two loop order, Phys. Rev. Lett. **33**, 244 (1974).

[223] T. Banks and A. Zaks, On the phase structure of vector-like gauge theories with massless fermions, Nucl. Phys. **B196**, 189 (1982).

[224] K. G. Chetyrkin, Quark mass anomalous dimension to $O(\alpha_s{}^4)$, Phys. Lett. B **404**, 161 (1997).

[225] J. A. M. Vermaseren, S. A. Larin, and T. van Ritbergen, The four loop quark mass anomalous dimension and the invariant quark mass, Phys. Lett. B **405**, 327 (1997).

[226] P. A. Baikov, K. G. Chetyrkin, and J. H. Kühn, Five-loop running of the QCD coupling constant, Phys. Rev. Lett. **118**, 082002 (2017).

[227] F. Herzog, B. Ruijl, T. Ueda, J. A. M. Vermaseren, and A. Vogt, The five-loop beta function of Yang-Mills theory with fermions, J. High Energy Phys. 02 (2017) 090.

[228] B. Holdom, Techniodor, Phys. Lett. **150B**, 301 (1985).

[229] K. Yamawaki, M. Bando, and K.-i. Matumoto, Scale invariant technicolor model and a technidilaton, Phys. Rev. Lett. **56**, 1335 (1986).

[230] T. W. Appelquist, D. Karabali, and L. C. R. Wijewardhana, Chiral hierarchies and the flavor changing neutral current problem in technicolor, Phys. Rev. Lett. **57**, 957 (1986).

[231] D. B. Kaplan, J.-W. Lee, D. T. Son, and M. A. Stephanov, Conformality lost, Phys. Rev. D **80**, 125005 (2009).

[232] S. Catterall and F. Sannino, Minimal walking on the lattice, Phys. Rev. D **76**, 034504 (2007).

[233] L. Del Debbio, A. Patella, and C. Pica, Higher representations on the lattice: Numerical simulations. $SU(2)$ with adjoint fermions, Phys. Rev. D **81**, 094503 (2010).

[234] A. J. Hietanen, J. Rantaharju, K. Rummukainen, and K. Tuominen, Spectrum of $SU(2)$ lattice gauge theory with two adjoint Dirac flavours, J. High Energy Phys. 05 (2009) 025.

[235] T. Appelquist, G. T. Fleming, and E. T. Neil, Lattice study of conformal behavior in $SU(3)$ Yang-Mills theories, Phys. Rev. D **79**, 076010 (2009).

[236] A. J. Hietanen, K. Rummukainen, and K. Tuominen, Evolution of the coupling constant in $SU(2)$ lattice gauge theory with two adjoint fermions, Phys. Rev. D **80**, 094504 (2009).

[237] L. Del Debbio, B. Lucini, A. Patella, C. Pica, and A. Rago, Conformal versus confining scenario in $SU(2)$ with adjoint fermions, Phys. Rev. D **80**, 074507 (2009).

[238] LSD collaboration, Toward TeV conformality, Phys. Rev. Lett. **104**, 071601 (2010).

[239] F. Bursa, L. Del Debbio, L. Keegan, C. Pica, and T. Pickup, Mass anomalous dimension in $SU(2)$ with two adjoint fermions, Phys. Rev. D **81**, 014505 (2010).

[240] Z. Fodor, K. Holland, J. Kuti, D. Nogradi, and C. Schroeder, Chiral symmetry breaking in nearly conformal gauge theories, Proc. Sci. LAT2009 (**2009**) 055 [arXiv:0911.2463].

[241] L. Del Debbio, B. Lucini, A. Patella, C. Pica, and A. Rago, The infrared dynamics of minimal walking technicolor, Phys. Rev. D **82**, 014510 (2010).

[242] T. DeGrand, Y. Shamir, and B. Svetitsky, Running coupling and mass anomalous dimension of $SU(3)$ gauge theory with two flavors of symmetric-representation fermions, Phys. Rev. D **82**, 054503 (2010).

[243] A. Patella, L. Del Debbio, B. Lucini, C. Pica, and A. Rago, Confining vs. conformal scenario for $SU(2)$ with adjoint fermions. Gluonic observables, Proc. Sci. LATTICE2010 (**2010**) 068 [arXiv:1011.0864].

[244] M. Hayakawa, K. I. Ishikawa, Y. Osaki, S. Takeda, S. Uno, and N. Yamada, Running coupling constant of ten-flavor QCD with the Schrödinger functional method, Phys. Rev. D **83**, 074509 (2011).

[245] Z. Fodor, K. Holland, J. Kuti, D. Nogradi, C. Schroeder, Twelve massless flavors and three colors below the conformal window, Phys. Lett. B **703**, 348 (2011).

[246] F. Bursa, L. Del Debbio, D. Henty, E. Kerrane, B. Lucini, A. Patella, C. Pica, T. Pickup, and A. Rago *et al.*, Improved lattice spectroscopy of minimal walking technicolor, Phys. Rev. D **84**, 034506 (2011).

[247] T. Appelquist, G. T. Fleming, M. F. Lin, E. T. Neil, and D. A. Schaich, Lattice simulations and infrared conformality, Phys. Rev. D **84**, 054501 (2011).

[248] T. DeGrand, Finite-size scaling tests for spectra in $SU(3)$ lattice gauge theory coupled to 12 fundamental flavor fermions, Phys. Rev. D **84**, 116901 (2011).

[249] T. Karavirta, J. Rantaharju, K. Rummukainen, and K. Tuominen, Determining the conformal window: $SU(2)$ gauge theory with $N_f = 4$, 6 and 10 fermion flavours, J. High Energy Phys. 05 (2012) 003.

[250] T. DeGrand, Y. Shamir, and B. Svetitsky, SU(4) lattice gauge theory with decuplet fermions: Schrödinger functional analysis, Phys. Rev. D **85**, 074506 (2012).

[251] T. Appelquist *et al.*, Approaching conformality with ten flavors, arXiv:1204.6000.

[252] C. J. D. Lin, K. Ogawa, H. Ohki, and E. Shintani, Lattice study of infrared behaviour in $SU(3)$ gauge theory with twelve massless flavours, J. High Energy Phys. 08 (2012) 096.

[253] Y. Aoki, T. Aoyama, M. Kurachi, T. Maskawa, K.-i. Nagai, H. Ohki *et al.*, Lattice study of conformality in twelve-flavor QCD, Phys. Rev. D **86**, 054506 (2012).

[254] A. Cheng, A. Hasenfratz, G. Petropoulos, and D. Schaich, Scale-dependent mass anomalous dimension from Dirac eigenmodes, J. High Energy Phys. 07 (2013) 061.

[255] T. DeGrand, Y. Shamir, and B. Svetitsky, Near the sill of the conformal window: Gauge theories with fermions in two-index representations, Phys. Rev. D **88**, 054505 (2013).

[256] A. Hasenfratz, A. Cheng, G. Petropoulos, and D. Schaich, Finite size scaling and the effect of the gauge coupling in 12 flavor systems, Proc. Sci. LATTICE2013 (**2014**) 075 [arXiv:1310.1124].

[257] LSD collaboration, Lattice simulations with eight flavors of domain wall fermions in $SU(3)$ gauge theory, Phys. Rev. D **90**, 114502 (2014).

[258] M. P. Lombardo, K. Miura, T. J. Nunes da Silva, and E. Pallante, On the particle spectrum and the conformal window, J. High Energy Phys. 12 (2014) 183.

[259] A. Hasenfratz, D. Schaich, and A. Veernala, Nonperturbative β function of eight-flavor $SU(3)$ gauge theory, J. High Energy Phys. 06 (2015) 143.

[260] A. Athenodorou, E. Bennett, G. Bergner, and B. Lucini, Infrared regime of $SU(2)$ with one adjoint Dirac flavor, Phys. Rev. D **91**, 114508 (2015).

[261] Z. Fodor, K. Holland, J. Kuti, S. Mondal, D. Nogradi, and C. H. Wong, The running coupling of 8 flavors and 3 colors, J. High Energy Phys. 06 (2015) 019.

[262] Z. Fodor, K. Holland, J. Kuti, S. Mondal, D. Nogradi, and C. H. Wong, The running coupling of the minimal sextet composite Higgs model, J. High Energy Phys. 09 (2015) 039.

[263] J. Rantaharju, T. Rantalaiho, K. Rummukainen, and K. Tuominen, Running coupling in $SU(2)$ gauge theory with two adjoint fermions, Phys. Rev. D **93**, 094509 (2016).

[264] J. Rantaharju, Gradient flow coupling in the $SU(2)$ gauge theory with two adjoint fermions, Phys. Rev. D **93**, 094516 (2016).

[265] Z. Fodor, K. Holland, J. Kuti, S. Mondal, D. Nogradi, and C. H. Wong, Fate of the conformal fixed point with twelve massless fermions and $SU(3)$ gauge group, Phys. Rev. D **94**, 091501 (2016).

[266] A. Athenodorou, E. Bennett, G. Bergner, D. Elander, C. J. D. Lin, B. Lucini, and M. Piai, Large mass hierarchies from strongly-coupled dynamics, J. High Energy Phys. 06 (2016) 114.

[267] A. Hasenfratz and D. Schaich, Nonperturbative β function of twelve-flavor $SU(3)$ gauge theory, J. High Energy Phys. 02 (2018) 132.

[268] V. Leino, J. Rantaharju, T. Rantalaiho, K. Rummukainen, J. M. Suorsa, and K. Tuominen, The gradient flow running coupling in $SU(2)$ gauge theory with $N_f = 8$ fundamental flavors, Phys. Rev. D **95**, 114516 (2017).

[269] V. Leino, K. Rummukainen, J. M. Suorsa, K. Tuominen, and S. Tähtinen, Infrared fixed point of $SU(2)$ gauge theory with six flavors, Phys. Rev. D **97**, 114501 (2018).

[270] A. Amato, V. Leino, K. Rummukainen, K. Tuominen, and S. Tähtinen, From chiral symmetry breaking to conformality in $SU(2)$ gauge theory, arXiv:1806.07154.

[271] Z. Fodor, K. Holland, J. Kuti, D. Nogradi, and C. H. Wong, Fate of a recent conformal fixed point and β-function in the $SU(3)$ BSM gauge theory with ten massless flavors, Proc. Sci. LATTICE2018 (**2018**) 199 [arXiv:1812.03972].

[272] A. Hasenfratz, C. Rebbi, and O. Witzel, Gradient flow step-scaling function for $SU(3)$ with twelve flavors, Phys. Rev. D **100**, 114508 (2019).

[273] A. Hasenfratz, C. Rebbi, and O. Witzel, Gradient flow step-scaling function for $SU(3)$ with ten fundamental flavors, Phys. Rev. D **101**, 114508 (2020).

[274] Lattice Strong Dynamics Collaboration, Near-conformal dynamics in a chirally broken system, Phys. Rev. D **103**, 014504 (2021).

[275] C. Lopez, G. Bergner, I. Montvay, and S. Piemonte, Measurement of the mass anomalous dimension of near-conformal adjoint QCD with the gradient flow, arXiv:2011.02815.

[276] A. Athenodorou, E. Bennett, G. Bergner, and B. Lucini, Investigating the conformal behavior of $SU(2)$ with one adjoint Dirac flavor, Phys. Rev. D **104**, 074519 (2021).

[277] E. Bennett, A. Athenodorou, G. Bergner, and B. Lucini, New lattice results for $SU(2)$ gauge theory with one adjoint Dirac flavor, Proc. Sci. LATTICE2021 (**2022**) 204 [arXiv:2110.12979].

[278] G. Bergner, J. C. Lopez, S. Piemonte, and I. S. Calero, Lattice simulations of adjoint QCD with one Dirac overlap fermion, Phys. Rev. D **106**, 094507 (2022).

[279] E. Bennett, A. Athenodorou, G. Bergner, P. Butti, and B. Lucini, Update on $SU(2)$ with one adjoint Dirac flavor, Proc. Sci. LATTICE2022 (**2023**) 204 [arXiv:2212.09173].

[280] G. Bergner, S. Piemonte, I. Soler Calero, and J. C. Lopez, One flavour adjoint QCD with overlap fermions, Proc. Sci. LATTICE2022 (**2023**) 206 [arXiv:2212.10210].

[281] A. Hasenfratz, E. T. Neil, Y. Shamir, B. Svetitsky, and O. Witzel, Infrared fixed point of the $SU(3)$ gauge theory with $N_f = 10$ flavors, Phys. Rev. D **108**, L071503 (2023).

[282] A. Athenodorou, E. Bennett, G. Bergner, P. Butti, J. Lenz, and B. Lucini, $SU(2)$ gauge theory with one and two adjoint fermions towards the continuum limit, arXiv:2408.00171.

[283] K. Rummukainen and K. Tuominen, Lattice computations for beyond standard model physics, Universe **8**, 188 (2022).

[284] S. Duane, A. D. Kennedy, B. J. Pendleton, and D. Roweth, Hybrid Monte Carlo, Phys. Lett. B **195**, 216 (1987).

[285] M. A. Clark and A. D. Kennedy, Accelerating dynamical fermion computations using the rational hybrid Monte Carlo (RHMC) algorithm with multiple pseudofermion fields, Phys. Rev. Lett. **98**, 051601 (2007).

[286] M. Lüscher, Properties and uses of the Wilson flow in lattice QCD, J. High Energy Phys. 08 (2010) 071.

[287] M. Luscher and P. Weisz, Perturbative analysis of the gradient flow in non-Abelian gauge theories, J. High Energy Phys. 02 (2011) 051.

[288] M. Lüscher, Future applications of the Yang-Mills gradient flow in lattice QCD, Proc. Sci. LATTICE2013 (**2014**) 016 [arXiv:1308.5598].

[289] P. A. Boyle, A. Juttner, C. Kelly, and R. D. Kenway, Use of stochastic sources for the lattice determination of light quark physics, J. High Energy Phys. 08 (2008) 086.

[290] S. Gusken, A study of smearing techniques for hadron correlation functions, Nucl. Phys. B, Proc. Suppl. **17**, 361 (1990).

[291] D. S. Roberts, W. Kamleh, D. B. Leinweber, M. S. Mahbub, and B. J. Menadue, Accessing high momentum states in lattice QCD, Phys. Rev. D **86**, 074504 (2012).

[292] C. Alexandrou, F. Jegerlehner, S. Gusken, K. Schilling, and R. Sommer, B-meson properties from lattice QCD, Phys. Lett. B **256**, 60 (1991).

[293] APE Collaboration, Glueball masses and string tension in lattice QCD, Phys. Lett. B **192**, 163 (1987).

[294] M. Falcioni, M. L. Paciello, G. Parisi, and B. Taglienti, Again on $SU(3)$ glueball mass, Nucl. Phys. **B251**, 624 (1985).

[295] G. Martinelli and Y.-C. Zhang, The connection between local operators on the lattice and in the continuum and its relation to meson decay constants, Phys. Lett. **123B**, 433 (1983).

[296] G. P. Lepage and P. B. Mackenzie, On the viability of lattice perturbation theory, Phys. Rev. D **48**, 2250 (1993).

[297] B. Sheikholeslami and R. Wohlert, Improved continuum limit lattice action for QCD with Wilson fermions, Nucl. Phys. **B259**, 572 (1985).

[298] G. Rupak and N. Shoresh, Chiral perturbation theory for the Wilson lattice action, Phys. Rev. D **66**, 054503 (2002).

[299] S. Sharpe and R. Singleton, Jr., Spontaneous flavor and parity breaking with Wilson fermions, Phys. Rev. D **58**, 074501 (1998).

[300] K. Symanzik, Continuum limit and improved action in lattice theories: (I). Principles and φ^4 theory, Nucl. Phys. **B226**, 187 (1983).

[301] M. Luscher, S. Sint, R. Sommer, and P. Weisz, Chiral symmetry and O(a) improvement in lattice QCD, Nucl. Phys. **B478**, 365 (1996).

[302] E. Bennett, D. K. Hong, H. Hsiao, J.-W. Lee, C.-J. D. Lin, B. Lucini *et al.*, Meson spectroscopy in the $Sp(4)$ gauge theory with three antisymmetric fermions—data release, 10.5281/zenodo.13819562 (2024).

[303] E. Bennett, D. K. Hong, H. Hsiao, J.-W. Lee, C.-J. D. Lin, B. Lucini *et al.*, Meson spectroscopy in the $Sp(4)$ gauge theory with three antisymmetric fermions—analysis workflow, 10.5281/zenodo.15116604 (2024).

[304] S. Matsuzaki and K. Yamawaki, Dilaton chiral perturbation theory: Determining the mass and decay constant of the technidilaton on the lattice, Phys. Rev. Lett. **113**, 082002 (2014).

[305] M. Golterman and Y. Shamir, Low-energy effective action for pions and a dilatonic meson, Phys. Rev. D **94**, 054502 (2016).

[306] A. Kasai, K.-i. Okumura, and H. Suzuki, A dilaton-pion mass relation, arXiv:1609.02264.

[307] M. Hansen, K. Langæble, and F. Sannino, Extending chiral perturbation theory with an isosinglet scalar, Phys. Rev. D **95**, 036005 (2017).

[308] M. Golterman and Y. Shamir, Effective pion mass term and the trace anomaly, Phys. Rev. D **95**, 016003 (2017).

[309] T. Appelquist, J. Ingoldby, and M. Piai, Dilaton EFT framework for lattice data, J. High Energy Phys. 07 (2017) 035.

[310] T. Appelquist, J. Ingoldby, and M. Piai, Analysis of a dilaton EFT for lattice data, J. High Energy Phys. 03 (2018) 039.

[311] M. Golterman and Y. Shamir, Large-mass regime of the dilaton-pion low-energy effective theory, Phys. Rev. D **98**, 056025 (2018).

[312] O. Catà and C. Müller, Chiral effective theories with a light scalar at one loop, Nucl. Phys. **B952**, 114938 (2020).

[313] O. Catà, R. J. Crewther, and L. C. Tunstall, Crawling technicolor, Phys. Rev. D **100**, 095007 (2019).

[314] T. Appelquist, J. Ingoldby, and M. Piai, Dilaton potential and lattice data, Phys. Rev. D **101**, 075025 (2020).

[315] M. Golterman, E. T. Neil, and Y. Shamir, Application of dilaton chiral perturbation theory to $N_f = 8$, $SU(3)$ spectral data, Phys. Rev. D **102**, 034515 (2020).

[316] M. Golterman and Y. Shamir, Explorations beyond dilaton chiral perturbation theory in the eight-flavor $SU(3)$ gauge theory, Phys. Rev. D **102**, 114507 (2020).

[317] T. Appelquist, J. Ingoldby, and M. Piai, Nearly conformal composite Higgs model, Phys. Rev. Lett. **126**, 191804 (2021).

[318] T. Appelquist, J. Ingoldby, and M. Piai, Composite two-Higgs doublet model from dilaton effective field theory, Nucl. Phys. **B983**, 115930 (2022).

[319] T. Appelquist, J. Ingoldby, and M. Piai, Dilaton effective field theory, Universe **9**, 10 (2023).

[320] C. N. Leung, S. T. Love, and W. A. Bardeen, Spontaneous symmetry breaking in scale invariant quantum electrodynamics, Nucl. Phys. **B273**, 649 (1986).

[321] W. A. Bardeen, C. N. Leung, and S. T. Love, The dilaton and chiral symmetry breaking, Phys. Rev. Lett. **56**, 1230 (1986).

[322] A. A. Migdal and M. A. Shifman, Dilaton effective Lagrangian in gluodynamics, Phys. Lett. **114B**, 445 (1982).

[323] S. Coleman, *Aspects of Symmetry: Selected Erice Lectures* (Cambridge University Press, Cambridge, England, 1985), 10.1017/CBO9780511565045.

[324] W. D. Goldberger, B. Grinstein, and W. Skiba, Distinguishing the Higgs boson from the dilaton at the large hadron collider, Phys. Rev. Lett. **100**, 111802 (2008).

[325] D. K. Hong, S. D. H. Hsu, and F. Sannino, Composite Higgs from higher representations, Phys. Lett. B **597**, 89 (2004).

[326] D. D. Dietrich, F. Sannino, and K. Tuominen, Light composite Higgs from higher representations versus electroweak precision measurements: Predictions for CERN LHC, Phys. Rev. D **72**, 055001 (2005).

[327] M. Hashimoto and K. Yamawaki, Techni-dilaton at conformal edge, Phys. Rev. D **83**, 015008 (2011).

[328] T. Appelquist and Y. Bai, A light dilaton in walking gauge theories, Phys. Rev. D **82**, 071701 (2010).

[329] L. Vecchi, Phenomenology of a light scalar: The dilaton, Phys. Rev. D **82**, 076009 (2010).

[330] B. Bellazzini, C. Csaki, J. Hubisz, J. Serra, and J. Terning, A Higgslike dilaton, Eur. Phys. J. C **73**, 2333 (2013).

[331] B. Bellazzini, C. Csaki, J. Hubisz, J. Serra, and J. Terning, A naturally light dilaton and a small cosmological constant, Eur. Phys. J. C **74**, 2790 (2014).

[332] T. Abe, R. Kitano, Y. Konishi, K.-y. Oda, J. Sato, and S. Sugiyama, Minimal dilaton model, Phys. Rev. D **86**, 115016 (2012).

[333] E. Eichten, K. Lane, and A. Martin, A Higgs impostor in low-scale technicolor, arXiv:1210.5462.

[334] P. Hernandez-Leon and L. Merlo, Distinguishing a Higgs-like dilaton scenario with a complete bosonic effective field theory basis, Phys. Rev. D **96**, 075008 (2017).

[335] J. Cruz Rojas, D. K. Hong, S. H. Im, and M. Järvinen, Holographic light dilaton at the conformal edge, J. High Energy Phys. 05 (2023) 204.

[336] L. Vecchi, A dangerous irrelevant UV-completion of the composite Higgs, J. High Energy Phys. 02 (2017) 094.

[337] T. Ma and G. Cacciapaglia, Fundamental composite 2HDM: SU(N) with 4 flavours, J. High Energy Phys. 03 (2016) 211.

[338] D. Buarque Franzosi, G. Cacciapaglia, and A. Deandrea, Sigma-assisted low scale composite Goldstone–Higgs, Eur. Phys. J. C **80**, 28 (2020).

[339] LatKMI Collaboration, Light composite scalar in eight-flavor QCD on the lattice, Phys. Rev. D **89**, 111502 (2014).

[340] T. Appelquist *et al.*, Strongly interacting dynamics and the search for new physics at the LHC, Phys. Rev. D **93**, 114514 (2016).

[341] LatKMI Collaboration, Light flavor-singlet scalars and walking signals in $N_f = 8$ QCD on the lattice, Phys. Rev. D **96**, 014508 (2017).

[342] A. D. Gasbarro and G. T. Fleming, Examining the low energy dynamics of walking gauge theory, Proc. Sci. LATTICE2016 (**2017**) 242 [arXiv:1702.00480].

[343] Lattice Strong Dynamics Collaboration, Nonperturbative investigations of $SU(3)$ gauge theory with eight dynamical flavors, Phys. Rev. D **99**, 014509 (2019).

[344] Lattice Strong Dynamics (LSD) Collaboration, Goldstone boson scattering with a light composite scalar, Phys. Rev. D **105**, 034505 (2022).

[345] A. Hasenfratz, Emergent strongly coupled ultraviolet fixed point in four dimensions with eight Kähler-Dirac fermions, Phys. Rev. D **106**, 014513 (2022).

[346] LSD Collaboration, Hidden conformal symmetry from the lattice, Phys. Rev. D **108**, L091505 (2023).

[347] Lattice Strong Dynamics Collaboration, Light scalar meson and decay constant in $SU(3)$ gauge theory with eight dynamical flavors, Phys. Rev. D **110**, 054501 (2024).

[348] Z. Fodor, K. Holland, J. Kuti, D. Nogradi, C. Schroeder, and C. H. Wong, Can the nearly conformal sextet gauge model hide the Higgs impostor?, Phys. Lett. B **718**, 657 (2012).

[349] Z. Fodor, K. Holland, J. Kuti, S. Mondal, D. Nogradi, and C. H. Wong, Toward the minimal realization of a light composite Higgs, Proc. Sci. LATTICE2014 (**2015**) 244 [arXiv:1502.00028].

[350] Z. Fodor, K. Holland, J. Kuti, S. Mondal, D. Nogradi, and C. H. Wong, Status of a minimal composite Higgs theory, Proc. Sci. LATTICE2015 (**2016**) 219 [arXiv:1605.08750].

[351] Z. Fodor, K. Holland, J. Kuti, D. Nogradi, and C. H. Wong, The twelve-flavor β-function and dilaton tests of the sextet scalar, EPJ Web Conf. **175**, 08015 (2018).

[352] Z. Fodor, K. Holland, J. Kuti, and C. H. Wong, Tantalizing dilaton tests from a near-conformal EFT, Proc. Sci. LATTICE2018 (**2019**) 196 [arXiv:1901.06324].

[353] Z. Fodor, K. Holland, J. Kuti, and C. H. Wong, Dilaton EFT from p-regime to RMT in the ϵ-regime, Proc. Sci. LATTICE2019 (**2020**) 246 [arXiv:2002.05163].

[354] M. A. Clark and A. D. Kennedy, The RHMC algorithm for two flavors of dynamical staggered fermions, Nucl. Phys. B, Proc. Suppl. **129**, 850 (2004).

[355] GitHub—sa2c/HiRep: HiRep repository—github.com, https://github.com/sa2c/HiRep/tree/d3ab8d8c4a3c3f678cebd7428a01ca086e6f3109.

[356] GitHub—sa2c/HiRep: HiRep repository—github.com, https://github.com/sa2c/HiRep/tree/9e66e56558e8b728796ca65e7a374aa62cc31ae9.

[357] T. Takaishi and P. de Forcrand, Testing and tuning new symplectic integrators for hybrid Monte Carlo algorithm in lattice QCD, Phys. Rev. E **73**, 036706 (2006).

[358] L. Del Debbio, B. Lucini, A. Patella, C. Pica, and A. Rago, Large volumes and spectroscopy of walking theories, Phys. Rev. D **93**, 054505 (2016).

[359] J. Bijnens and J. Lu, Technicolor and other QCD-like theories at next-to-next-to-leading order, J. High Energy Phys. 11 (2009) 116.

[360] Z. Fodor, K. Holland, J. Kuti, D. Nogradi, and C. H. Wong, The Yang-Mills gradient flow in finite volume, J. High Energy Phys. 11 (2012) 007.

[361] A. Hasenfratz and O. Witzel, Continuous renormalization group β function from lattice simulations, Phys. Rev. D **101**, 034514 (2020).

[362] BMW Collaboration, High-precision scale setting in lattice QCD, J. High Energy Phys. 09 (2012) 010.

[363] M. Hasenbusch and K. Jansen, Speeding up lattice QCD simulations with clover improved Wilson fermions, Nucl. Phys. **B659**, 299 (2003).

[364] L. Del Debbio, H. Panagopoulos, and E. Vicari, θ dependence of SU(N) gauge theories, J. High Energy Phys. 08 (2002) 044.

[365] S. Aoki, H. Fukaya, S. Hashimoto, and T. Onogi, Finite volume QCD at fixed topological charge, Phys. Rev. D **76**, 054508 (2007).

[366] GitHub—sa2c/HiRep: HiRep repository—github.com, https://github.com/sa2c/HiRep/tree/1b204b666a23c4f18047cc233941dbdf8c8a3fcd.

[367] K. Kawarabayashi and M. Suzuki, Partially conserved axial vector current and the decays of vector mesons, Phys. Rev. Lett. **16**, 255 (1966).

[368] Riazuddin and Fayyazuddin, Algebra of current components and decay widths of ρ and $K*$ mesons, Phys. Rev. **147**, 1071 (1966).

[369] L. Del Debbio and R. Zwicky, Hyperscaling relations in mass-deformed conformal gauge theories, Phys. Rev. D **82**, 014502 (2010).

[370] N. Butt, S. Catterall, and A. Hasenfratz, Symmetric mass generation with four $SU(2)$ doublet fermions, Phys. Rev. Lett. **134**, 031602 (2025).

[371] A. V. Manohar, Large N QCD, in Les Houches Summer School in Theoretical Physics, Session 68: Probing the Standard Model of Particle Interactions (1998), pp. 1091–1169, arXiv:hep-ph/9802419.

[372] D. Nogradi, D. Nogradi, L. Szikszai, and L. Szikszai, The flavor dependence of m_ϱ/f_π, J. High Energy Phys. 05 (2019) 197.

[373] D. Nogradi and L. Szikszai, The model dependence of m_ϱ/f_π, Proc. Sci. LATTICE2019 (**2019**) 237 [arXiv:1912.04114].

[374] A. Y. Kotov, D. Nogradi, K. K. Szabo, and L. Szikszai, More on the flavor dependence of $\mathrm{m}_\varrho/\mathrm{f}_\pi$, J. High Energy Phys. 07 (2021) 202.

[375] Particle Data Group Collaboration, Review of particle physics, Phys. Rev. D **110**, 030001 (2024).

[376] A. Afzal, G. Agazie, A. Anumarlapudi, A. M. Archibald, Z. Arzoumanian, P. T. Baker *et al.*, The nanograv 15 yr data set: Search for signals from new physics, Astrophys. J. Lett. **951**, L11 (2023).

[377] R. D. Pisarski, Quark gluon plasma as a condensate of $SU(3)$ Wilson lines, Phys. Rev. D **62**, 111501 (2000).

[378] R. D. Pisarski, Tests of the Polyakov loops model, Nucl. Phys. **A702**, 151 (2002).

[379] R. D. Pisarski, Notes on the deconfining phase transition, in *Cargese Summer School on QCD Perspectives on Hot and Dense Matter* (2002), pp. 353–384, arXiv:hep-ph/0203271.

[380] F. Sannino, Polyakov loops versus hadronic states, Phys. Rev. D **66**, 034013 (2002).

[381] C. Ratti, M. A. Thaler, and W. Weise, Phases of QCD: Lattice thermodynamics and a field theoretical model, Phys. Rev. D **73**, 014019 (2006).

[382] K. Fukushima and C. Sasaki, The phase diagram of nuclear and quark matter at high baryon density, Prog. Part. Nucl. Phys. **72**, 99 (2013).

[383] K. Fukushima and V. Skokov, Polyakov loop modeling for hot QCD, Prog. Part. Nucl. Phys. **96**, 154 (2017).

[384] P. M. Lo, B. Friman, O. Kaczmarek, K. Redlich, and C. Sasaki, Polyakov loop fluctuations in $SU(3)$ lattice gauge theory and an effective gluon potential, Phys. Rev. D **88**, 074502 (2013).

[385] H. Hansen, R. Stiele, and P. Costa, Quark and Polyakov-loop correlations in effective models at zero and nonvanishing density, Phys. Rev. D **101**, 094001 (2020).

[386] P. N. Meisinger, T. R. Miller, and M. C. Ogilvie, Phenomenological equations of state for the quark gluon plasma, Phys. Rev. D **65**, 034009 (2002).

[387] A. Dumitru, Y. Guo, Y. Hidaka, C. P. K. Altes, and R. D. Pisarski, How wide is the transition to deconfinement?, Phys. Rev. D **83**, 034022 (2011).

[388] A. Dumitru, Y. Guo, Y. Hidaka, C. P. K. Altes, and R. D. Pisarski, Effective matrix model for deconfinement in pure gauge theories, Phys. Rev. D **86**, 105017 (2012).

[389] K.-I. Kondo, Confinement–deconfinement phase transition and gauge-invariant gluonic mass in Yang-Mills theory, arXiv:1508.02656.

[390] R. D. Pisarski and V. V. Skokov, Chiral matrix model of the semi-QGP in QCD, Phys. Rev. D **94**, 034015 (2016).

[391] H. Nishimura, R. D. Pisarski, and V. V. Skokov, Finite-temperature phase transitions of third and higher order in gauge theories at large N, Phys. Rev. D **97**, 036014 (2018).

[392] Y. Guo and Q. Du, Two-loop perturbative corrections to the constrained effective potential in thermal QCD, J. High Energy Phys. 05 (2019) 042.

[393] C. P. Korthals Altes, H. Nishimura, R. D. Pisarski, and V. V. Skokov, Free energy of a holonomous plasma, Phys. Rev. D **101**, 094025 (2020).

[394] Y. Hidaka and R. D. Pisarski, Effective models of a semi-quark-gluon plasma, Phys. Rev. D **104**, 074036 (2021).

[395] K. Langfeld, B. Lucini, and A. Rago, The density of states in gauge theories, Phys. Rev. Lett. **109**, 111601 (2012).

[396] K. Langfeld and J. M. Pawlowski, Two-color QCD with heavy quarks at finite densities, Phys. Rev. D **88**, 071502 (2013).

[397] K. Langfeld, B. Lucini, R. Pellegrini, and A. Rago, An efficient algorithm for numerical computations of continuous densities of states, Eur. Phys. J. C **76**, 306 (2016).

[398] G. Cossu, D. Lancaster, B. Lucini, R. Pellegrini, and A. Rago, Ergodic sampling of the topological charge using the density of states, Eur. Phys. J. C **81**, 375 (2021).

[399] C. N. Leung, S. T. Love, and W. A. Bardeen, Aspects of dynamical symmetry breaking in gauge field theories, Nucl. Phys. **B323**, 493 (1989).

[400] R. Zwicky, QCD with an infrared fixed point and a dilaton, Phys. Rev. D **110**, 014048 (2024).